The alkaline lamprophyres of the Dolomitic Area (Southern Alps, Italy): markers of the Late Triassic change from orogenic-like to anorogenic magmatism

Running title: A Late Triassic alkaline-carbonatitic pulse in the Dolomitic Area

Federico Casetta*

Department of Physics and Earth Sciences, University of Ferrara

Via Saragat 1, 44121 Ferrara, Italy

Ryan B. Ickert

Scottish Universities Environmental Research Centre, Scottish Enterprise Technology Park, Rankine Avenue, East Kilbride, G75 0QF, UK

Darren F. Mark

Scottish Universities Environmental Research Centre, Scottish Enterprise Technology Park, Rankine Avenue, East Kilbride, G75 0QF, UK

Department of Earth & Environmental Science, University of St Andrews, St Andrews, KY16 9AJ, UK

Costanza Bonadiman**

Department of Physics and Earth Sciences, University of Ferrara

Via Saragat 1, 44121 Ferrara, Italy

Pier Paolo Giacomoni

Department of Physics and Earth Sciences, University of Ferrara

Via Saragat 1, 44121 Ferrara, Italy

Theodoros Ntaflos

Department of Lithospheric Research, Universität Wien

Althanstraße 14 (UZA II), 1090 Wien, Austria

Massimo Coltorti

Department of Physics and Earth Sciences, University of Ferrara

Via Saragat 1, 44121 Ferrara, Italy

* Corresponding author. Phone +39 0532 974721. E-mail: cstfrc@unife.it

** Corresponding author. Phone +39 0532 974720. E-mail: bdc@unife.it

The alkaline lamprophyres of the Dolomitic Area (Southern Alps, Italy): markers of the Late Triassic change from orogenic-like to anorogenic magmatism

ABSTRACT

In this paper, the first complete petrological, geochemical and geochronological characterization of the oldest lamprophyric rocks in Italy cropping out around Predazzo (Dolomitic Area) is presented, with the aim of deciphering their relationship with the Triassic magmatic events of the whole Southern Alps. Their Mg# between 37 and 70, together with their trace element content, suggest that fractional crystallization was the main process responsible of their differentiation, together with small scale mixing, as evidenced by some complex amphibole textures. Moreover, the occurrence of primary carbonate ocelli suggests an intimate association between alkaline lamprophyric magmas and a carbonatitic melt. $^{40}Ar/^{39}Ar$ data show that lamprophyres were emplaced at 219.22 ± 0.73 Ma (2σ; full systematic uncertainties), around 20 Ma after the high K calc-alkaline to shoshonitic short-lived Ladinian (237-238 Ma) magmatic event of the Dolomitic Area. Their trace element and Sr-Nd isotopic signature ($^{87}Sr/^{86}Sr_i$ = 0.7033-0.7040; $^{143}Nd/^{144}Nd_i$ = 0.51260-0.51265) is likely related to a garnet-amphibole-bearing lithosphere interacting with an asthenospheric component, significantly more depleted than the mantle source of the high K calc-alkaline to shoshonitic magmas. These features suggest that Predazzo lamprophyres belong to the same alkaline-carbonatitic magmatic event that intruded the mantle beneath the Southern Alps (i.e. Finero peridotite) between 190 and 225 Ma. In this scenario, Predazzo lamprophyres cannot be considered as a late-stage pulse of the orogenic-like Ladinian magmatism of the Dolomitic Area, but most likely represent the petrological bridge to the opening of the Alpine Tethys.

KEYWORDS

Carbonatitic alkaline lamprophyre; Amphibole texture; Camptonite; Dolomitic Area; Predazzo; Southern Alps; Triassic magmatism.

INTRODUCTION

The late-stage emplacement of lamprophyric dykes typifies a large number of plutonic complexes, providing important information of the local geodynamic evolution. According to Rock *et al.* (1987), Le Maitre *et al.* (1989), Rock (1991), Woolley *et al.* (1996) and Le Maitre *et al.* (2002), lamprophyres are defined as H_2O-, CO_2-, and alkali-rich rocks with a porphyritic texture, characterized by the compulsory presence of amphibole and/or phlogopite-biotite phenocrysts and the common occurrence of halides, carbonates, sulphides and zeolites. Feldspars and/or feldspathoids are often present in the groundmass. Mineral chemistry is by far a key factor for the identification/classification of these rocks: high-Ti, -Ba and -F amphiboles and micas, high-Al clinopyroxenes, high-Zn spinels and Fe^{3+}-rich micas are in fact diagnostic phases of lamprophyres. The genesis of lamprophyres is commonly attributed to partial melting of a metasomatised mantle (Rock, 1991; Stoppa *et al.*, 2014; Pandey *et al.*, 2017*a*; 2017*b*; Soder & Romer, 2018), while their emplacement is usually associated with the onset of lithospheric extensional-transtensional tectonic regimes. Lamprophyres are often associated with strike-slip movements, and may mark a change in the geodynamic regime (Scarrow *et al.*, 2011). Following Le Maitre *et al.* (2002), lamprophyric rocks are grouped, on the basis of their mineralogy, into three associations: i) minette-kersantite; ii) vogesite-spessartite; and iii) sannaite-camptonite-monchiquite. This discrimination partially reflects what was originally proposed by Le Maitre *et al.* (1989) and Rock (1991), according to whom the first two associations belong to the "calc-alkaline (shoshonitic) lamprophyres", whereas the third to the "alkaline lamprophyres". While the calc-alkaline variety is commonly associated with convergent settings, alkaline lamprophyres are typical of divergent margins and continental intra-plate settings (Rock, 1991; Batki *et al.*, 2014; Stoppa *et al.*, 2014; Ubide *et al.*, 2014; Lu

et al., 2015; Pandey *et al.*, 2017*a*; 2017*b*), their composition resembling volatile-enriched alkali basalts, basanites and nephelinites.

Several authors have investigated the main geochemical features of the Cretaceous (110 Ma) to Oligocenic (29 Ma) alkaline lamprophyres across Italy, suggesting their formation by partial melting of a mantle metasomatized by alkaline carbonatitic components (Galassi *et al.*, 1994; Vichi *et al.*, 2005; Stoppa, 2008; Stoppa *et al.*, 2014). Lesser known are the alkaline lamprophyres of the Dolomitic Area (Southern Alps, NE Italy), intruded in and around the Middle Triassic Predazzo Intrusive Complex, to which they seemed geochemically and temporally related (Lucchini *et al.*, 1969). This complex is one of the few plutonic expressions of the high-K calc-alkaline to shoshonitic magmatism that shaped the Dolomitic Area between 237 and 238 Ma (Gasparotto & Simboli, 1991; Bonadiman *et al.*, 1994; Mundil *et al.*, 1996; Abbas *et al.*, 2018; Casetta *et al.*, 2018*a*; 2018*b*; Storck *et al.*, 2018; Wotzlaw *et al.*, 2018). Recent petrologic and Sr-Nd isotopic studies on the Predazzo pluton, complemented by field observations, revealed: i) the existence of three different SiO_2-oversaturated to -undersaturated magma batches and their precise emplacement sequence at shallow crustal depth (1.4-5.6 km); ii) the gradual transition between the intrusion and the overlying hypabyssal and volcanic (basaltic/latitic) deposits; iii) the EM I-like Sr-Nd isotopic signature of the intrusive rocks and the low degree of crustal assimilation experienced by Ladinian magmas during ascent; and iv) the slight isotopic depletion of the mantle source moving towards higher $^{143}Nd/^{144}Nd$ ratios from the older SiO_2-saturated to the younger SiO_2-undersaturated batches (Casetta *et al.*, 2018*a*; 2018*b*).

The connection between the alkaline lamprophyres and the host volcano-plutonic complex has never been investigated, despite being a key factor in deciphering the evolution of the magmatism of the Dolomitic Area. For this reason, whole-rock major, trace element and Sr-Nd isotopic determinations, together with mineral phases major and trace element chemistry, were used to characterize the Predazzo alkaline lamprophyres mantle source, and identify how the

melts differentiated at shallow depths. Finally, $^{40}Ar/^{39}Ar$ dating constrained their emplacement within the temporal evolution of the Dolomitic Area and the whole Southern Alps magmatism.

GEOLOGICAL AND GEODYNAMIC OVERVIEW

The geodynamic framework of the Austroalpine and Southalpine domains during Middle-Late Triassic is complicated by the short timescales, variety of magma types, and overprinting by Alpine orogenesis. Magmas with calc-alkaline to shoshonitic affinity intruded in several localities of the Southern Alps, Dynarides and Hellenides between ~242 and 227±6 Ma (Barbieri et al., 1982; Pamić, 1984; Gianolla, 1992; Mundil *et al.*, 1996; Pe-Piper, 1998; Armienti *et al.*, 2003; Beccaluva *et al.*, 2005; Cassinis *et al.*, 2008; Bellieni *et al.*, 2010; Beltràn-Trivino *et al.*, 2016; Bianchini *et al.*, 2018; Storck *et al.*, 2018; Wotzlaw *et al.*, 2018). Simultaneously, scattered intrusions of alkaline magmas emplaced between 231±1 and 227±7 Ma along the Periadriatic lineament (Karawanken) and in the Carpathians (Ditrau) area (Lippolt & Pidgeon, 1974; Dallmeyer *et al.*, 1997; Morogan *et al.*, 2000; Visonà & Zanferrari, 2000; Batki *et al.*, 2014; Pál-Molnár *et al.*, 2015).

The close relationship between the orogenic magmatism and the onset of extensional-transtensional tectonics (Doglioni, 1984, 1987, 2007; Stampfli & Borel, 2002; 2004) led some to hypothesize various possible geodynamic scenarios for the Southern Alps. They include: i) aborted rifting in a passive margin (Bernoulli & Lemoine, 1980); ii) active mantle upwelling (Stähle *et al.*, 2001); iii) arc system at the Paleo-Tethys NW limb (Castellarin *et al.*, 1988); iv) back-arc development connected to the subduction of the Paleo-Tethys (Ziegler & Stampfli, 2001; Stampfli & Borel, 2002; 2004; Stampfli *et al.*, 2002; Armienti *et al.*, 2003; Stampfli, 2005; Cassinis *et al.*, 2008; Schmid *et al.*, 2008; Zanetti *et al.*, 2013); v) anorogenic rifting with subduction signature inherited from the Hercynian orogeny (Sloman, 1989; Bonadiman *et al.*, 1994; Pe-Piper, 1998; Beltràn-Trivino *et al.*, 2016). Other authors, trying to encompass the Austroalpine and Carnian-Dinaric domains in the geodynamic reconstruction, hypothesized: vi)

the presence, beneath the Southern Alps-Austroalpine and Carnian-Dinaric plates, of different mantle sources affected by Palaeozoic subduction-related and plume-related processes, respectively (Visonà & Zanferrari, 2000); and vii) the existence of a Palaeozoic oceanic basin between Austroalpine and Southern Alps, closed by a subduction dipping beneath the latter (Bianchini *et al.*, 2018).

MATERIALS AND METHODS

Whole-rock major and trace element analyses were carried out at the Department of Physics and Earth Sciences of the University of Ferrara using an ARL Advant-XP automated X-ray fluorescence spectrometer. Full matrix correction procedure and intensities were completed following Traill & Lachance (1966). Accuracy and precision are better than 2-5% for major elements and 5-10% for trace elements. Detection limits are 0.01 wt% and 1-3 ppm for most of the major and trace element concentrations, respectively.

Rb, Sr, Y, Zr, Nb, Hf, Ta, Th, U, and rare-earth elements (REE) were analyzed at the Department of Physics and Earth Sciences of the University of Ferrara by inductively coupled plasma-mass spectrometry (ICP-MS) using a Thermo Series X spectrometer. Precision and accuracy were better than 10% for all elements, well above the detection limit.

Mineral phase major element compositions were analyzed at the Department of Lithospheric Research of the University of Wien, using a CAMECA SX100 electron microprobe equipped with four WD and one ED spectrometers. The operating conditions were as follows: 15 kV accelerating voltage, 20 nA beam current, and 20 s counting time on peak position. Natural and synthetic standards were used for calibration, and PAP corrections were applied to the intensity data (Pouchou & Pichoir, 1991).

Trace element concentration of pyroxene and amphibole crystals was carried out at the CNR - Istituto di Georisorse of Pavia by laser ablation microprobe-inductively coupled plasma-mass spectrometry (LAM-ICP-MS). The basic set and protocol were described by Tiepolo *et al.*

(2003). NIST 610 and NIST 612 standard glasses were used to calibrate relative element sensitivity. Precision and accuracy for trace element analyses were assessed by standard sample BCR-2 (reference values from USGS Geochemical Reference Materials Database). Each analysis was corrected with internal standards using CaO for both clinopyroxene and amphibole. The detection limit was function of the ablation volume and counting time and was therefore calculated for each analysis; indeed, ablation volume greatly depends on instrument configuration. As a consequence, the detection limit reduces if spot size, beam power and cell gas flow are decreased. A 40-100 μm beam diameter and 20 μm s1 scanning rate were used. The theoretical detection limit ranges from 10 to 20 ppb for REE, Ba, Th, U, Zr and are about 2 ppm for Ti.

Whole-rock $^{87}Sr/^{86}Sr$ and $^{143}Nd/^{144}Nd$ analyses were made at the Scottish Universities Environmental Research Centre (SUERC) by thermal ionization mass spectrometry (TIMS) following procedures described by Casetta *et al.* (2018*a*). Eight measurements of SRM-987 and 12 of JNdi-1 made during the course of this analytical programme yielded mean values of 0.710244±0.000016, and 0.512079±0.000018 (2 SD), consistent with the consensus values of ~0.71025 and ~0.51210.

$^{40}Ar/^{39}Ar$ analyses on amphibole and plagioclase separates were made at SUERC. Samples for $^{40}Ar/^{39}Ar$ dating were prepared using the methods described in Mark *et al.* (2011*a*). All samples were subsequently cleaned in de-ionised water. They were parcelled in high purity Al discs for irradiation. International standards Fish Canyon sanidine (FCs) (28.294 ± 0.036 Ma, Renne *et al.*, 2011; Morgan *et al.*, 2014) and GA1550 biotite (99.738 ± 0.104 Ma, Renne *et al.*, 2011) were loaded adjacent to the samples to permit accurate characterisation of the neutron flux (J parameter). Samples were irradiated for 50 hours in the Cd-lined facility of the CLICIT Facility at the OSU TRIGA reactor. Standards were analyzed on a MAP 215-50 system (described below briefly and in more detail by Ellis *et al.*, 2012) - FCs was analyzed by CO_2 laser total fusion as single crystals (n = 20). GA1550 (n = 20) was also analyzed by CO_2 laser total fusion

and step-heated using a CO_2 scanning laser (n = 5) (Barfod *et al.*, 2014). Using GA1550 the J-parameter was determined to a precision approaching 0.1% uncertainty.

Wafers were loaded into an Ultra-High-Vacuum (UHV) laser cell with a SiO_2 window. In situ UVLAMP Ar extraction was conducted using a New Wave UP-213 nm UV laser system (described in Moore *et al.*, 2011). 50 × 50 × 5 μm^3 (amounts of ablated material approximately 1250 μm^3) raster pits were made in mineral surfaces to extract the Ar isotopes. All gas fractions were subjected to 180 seconds of purification by exposure to two SAES GP50 getters (one maintained at room temperature, the other held at ca. 450˚C). A cold finger was maintained at -95.5˚C using a mixture of dry ice ($CO_{2[S]}$) and acetone. Ion beam intensities (i.e., Ar isotope intensities and hence ratios) were measured using a MAP 215-50 mass spectrometer in peak jumping mode. Measurements were made using a Balzers SEV-217 electron multiplier. The system had a measured sensitivity of 1.12×10^{-13} moles/Volt. The extraction and cleanup, as well as mass spectrometer inlet and measurement protocols and data acquisition were automated. Blanks (full extraction line and mass spectrometer) were made following every two analyses of unknowns. The average blank ± standard deviation (n = 28) from the entire blank run sequence was used to correct raw isotope measurements from unknowns. Mass discrimination was monitored by analysis of air pipette aliquots after every five analyses of unknowns (n = 13, 7.21 x 10^{-14} moles ^{40}Ar, $^{40}Ar/^{36}Ar = 289.67 \pm 0.63$).

The samples were step-heated using a CO_2 laser (approximately 500-1500˚C, optical pyrometer measurements). Extracted gases were subjected to 300 seconds of purification by exposure to two SAES GP50 getters (one maintained at room temperature, the other held at ca. 450˚C). A cold finger was maintained at -95.5˚C using a mixture of dry ice ($CO_{2[S]}$) and acetone. Ion beam intensities were measured using a MAP 215-50 mass spectrometer in peak jumping mode. Measurements were made using a Balzers SEV-217 electron multiplier. The system had a measured sensitivity of 1.12×10^{-13} moles/Volt. The extraction and cleanup, as well as mass spectrometer inlet and measurement protocols and data acquisition were automated. Blanks

(full extraction line and mass spectrometer) were made following every analysis of an unknown. The average blank ± standard deviation for each experiment (n = 14) from the entire blank run sequence was used to correct raw isotope measurements from unknowns. Mass discrimination was monitored by analysis of air pipette aliquots after every three analyses.

All Ar isotope data were corrected for backgrounds, mass discrimination, and reactor-produced nuclides and processed using standard data reduction protocols and reported according to the criteria of Renne *et al.* (2009). The atmospheric argon isotope ratios of Lee *et al.* (2006), which have been independently verified by Mark *et al.* (2011*b*), were employed. The $^{40}Ar/^{39}Ar$ ages for were determined relative to the statistical optimization model of Renne *et al.* (2010; 2011) and are reported including analytical and full systematic uncertainties at the 2 sigma level. All raw Ar/Ar data with associated parameters are presented in Electronic Appendix 1.

PETROGRAPHY AND WHOLE-ROCK GEOCHEMISTRY

Petrography

The lamprophyres are part of a swarm of dykes that intrudes the Predazzo Intrusive Complex, the overlying volcanites and the Permo-Triassic sedimentary host rocks (Fig. 1). The dykes are mainly porphyritic basalts to trachytes, the great majority of them having the same high-K calc-alkaline to shoshonitic affinity of the intrusive rocks (Casetta *et al.*, 2018*a*; 2018*b*). Lamprophyres are 20-200 cm in thickness, NNW-SSW to N-S oriented and can be easily distinguished by their greenish colour, strongly contrasting with the pink granitic/syenogranitic body that they preferentially intrude (Fig. 1; see also Lucchini *et al.*, 1969). Contacts are generally sharp, and no significant thermometamorphic structures are present, although intense alteration often obscures hand-sample scale textures.

A distinctive feature is the common presence of carbonate-bearing ocelli, feldspar and amphibole megacrysts (up to 5 cm), and xenoliths (Fig. 1; Vardabasso, 1929; Lucchini *et al.*, 1969; 1982). The latters are mainly cumulate clinopyroxenites (Morten, 1980) or fragments of

the Triassic intrusive rocks and the Permian basement, but also a few spinel lherzolites can be found (Carraro & Visonà, 2003). The petrology and geochemistry of lamprophyres led Lucchini *et al.* (1969) to classify them as camptonites, an alkaline variety of lamprophyres characterized by abundant plagioclase (modally more abundant than K-feldspar), and the absence of leucite and Na-foids (Rock, 1991).

The dykes are panidiomorphic, with, in order of decreasing abundance, amphibole, plagioclase, clinopyroxene and olivine phenocrysts, embedded in a microcrystalline assemblage of amphibole, plagioclase, clinopyroxene, K-feldspar and Fe-Ti oxides (Fig. 2). Accessory phases include carbonate, ilmenite, titanite, apatite and analcime. The modal abundances are: amphibole 35-55 vol.%, plagioclase 30-40 vol.%, clinopyroxene 0-10 vol.%, olivine 0-10 vol.%, K-feldspar 2-6 vol.%, Fe-Ti oxides 3-6 vol.%. Clinopyroxene and olivine are only absent in MA1 sample (Fig. 2b), where the presence of plagioclase, K-feldspar and Fe-Ti oxides strongly increases. Carbonate is present as pseudomorphic phase replacing olivine, in secondary veins/fractures, or as a major constituent of small (200-250 μm in diameter) spherical ocelli, variably distributed and surrounded by the orthogonal growth of multiple small plagioclase, amphibole and/or clinopyroxene crystals (see the following section for a more detailed descripton). These features confirm the definition of camptonites proposed by the previous authors for all Predazzo lamprophyres.

Amphibole, pale brown to reddish in colour, occurs as euhedral, elongate crystals as both phenocrysts and in the groundmass. In sample MA1, amphibole is often acicular and has a pale brown to yellowish colour (Fig. 2b). It ranges in size from 20-30 μm (groundmass) to 2.5 mm (phenocryst), excluding megacrysts, whose colour ranges from dark brown to black.

Plagioclase crystals are generally euhedral and vary in size between 10-20 and 400-450 μm. Larger plagioclase xenocrysts, fragments and xenoliths (0.5-1 mm) of crustal origin can be easily distinguished from the phenocrysts by their rounded shape and by the presence of well developed reaction rims made of Fe-Ti oxides, secondary feldspar and rare clinopyroxene.

Clinopyroxene, pale brown in colour, is less abundant and smaller than amphibole, rarely exceeding 150-200 μm in size among the phenocrysts. Relicts of bigger euhedral crystals (1-2 mm) are almost totally replaced by plagioclase, amphibole and Fe-Ti oxides, resulting in an "atoll-like" shape, where only the outermost rim of clinopyroxene is preserved. The formation of secondary epidote and chlorite often occurs at the expense of clinopyroxene.

Olivine phenocrysts (100-350 μm) are rare and usually pseudomorphosed by calcite and serpentine. This kind of alteration, typical in lamprophyres, is indicated by the general term pilite (Velde, 1968; Rock, 1991). K-feldspar and Fe-Ti oxides are present only in the groundmass, rarely exceeding 40-50 μm in size.

Whole-rock major and trace element chemistry

Predazzo camptonites generally have a SiO_2 range of 44.1 to 47.9 wt%, 1.6-3.2 Na_2O wt% and 1.0-3.7 K_2O wt%; sample MA1 is an exception, and has higher silica (52.8 wt%) and alkali contents (2.9 Na_2O wt%; 5.0 K_2O wt%; Table 1). Mg# is variable, varying between 37 and 70, and mainly controlled by a wide range in MgO. Again, sample MA1 has the lowest FeO content, and is probably more differentiated than the rest of the samples. All lamprophyres have a K-affinity (Fig. 3), and their CaO contents are variable depending upon alteration and presence of carbonates. In the Al_2O_3-MgO-CaO and $SiO_2/10$-CaO-$TiO_2\times4$ ternary diagrams, all samples plot in the alkaline lamprophyres field (Rock, 1987; 1991), and are enriched in Al_2O_3 with respect to the Cretaceous to Oligocene Italian lamprophyres (Stoppa *et al.*, 2014, and references therein). CIPW norm calculations highlight the moderate to strong Si-undersaturation, with 1-13% normative nepheline for all samples and 3-5% normative leucite for two samples with high K/Si. MgO is negatively correlated with compatible elements, such as Ni (237-27 ppm) and Cr (585-14 ppm; Fig. 3).

Whole-rock chondrite-normalized incompatible element patterns (Fig. 4) have positive anomalies in Nb, Ta, Zr, Ti and LILE (especially Sr), and negative anomalies in Th and U.

These features are similar to the Central Iberia lamprophyres (Scarrow *et al.*, 2011). Predazzo lamprophyre patterns resemble those of alkaline rocks, but, when compared to the average composition of oceanic island basalts, they are depleted in all elements except Rb, Ba and Sr. This feature is even more evident when compared to the worldwide camptonites (Fig. 4; Rock, 1991). Chondrite-normalized REE patterns are characterised by LREE enrichment and flat M-HREE profiles, with absence of Eu negative anomaly, consistent with the lack of significant plagioclase fractionation (Fig. 4). The less differentiated camptonite (Mg# 70) is slightly LREE-depleted with respect to the other samples. The Gd_N/Yb_N ratios of Predazzo camptonites range between 1.7 and 2.7, contrasting with the typical steep-sloping shape of OIB rocks in general, and of camptonites in particular (Fig. 4; Sun & McDonough, 1989; Rock, 1991). Compared to the other Italian lamprophyres (Galassi *et al.*, 1994; Vichi *et al.*, 2005; Stoppa, 2008; Stoppa *et al.*, 2014), Predazzo camptonites are generally depleted in all incompatible elements, except for Rb and K. A common feature is the absence of a Ta-Nb-Ti negative anomaly (Fig. 4). The HFSE distribution in the less differentiated Predazzo camptonites fall in the OIB field on a Th_N vs. Nb_N tectonic discrimination diagram (Fig. 5a; Saccani, 2015), suggesting a within-plate setting. The alkaline nature of Predazzo lamprophyres is clearly evidenced by the Ti/Y vs. Nb/Y and Zr/Y vs. Zr diagrams (Fig. 5b-c; Pearce & Norry, 1979; Pearce, 1982), as well as by the Th-Hf-Ta and Zr-Nb-Y ternary diagrams (Fig. 5e-f; Wood, 1980; Meschede, 1986).

MINERAL CHEMISTRY AND TEXTURAL RELATIONSHIPS

Major element composition of amphibole, clinopyroxene, feldspars, oxides and trace element analyses of amphibole and clinopyroxene were determined on representative lamprophyre samples. The intense state of alteration of olivine in pilite prevented its chemical analysis: according to Carraro & Visonà (2003), olivine phenocrysts in the less evolved Predazzo camptonites range in composition from $Fo_{72.5}$ to $Fo_{87.5}$, suggesting a primitive, mantle-derived nature of these rocks.

Amphibole

We adopted the Locock (2014) a.p.f.u. amphibole classification, consistent with the recommendations of the IMA-CNMNC subcommittee on amphiboles (Table 2; Hawthorne *et al.*, 2012; Oberti *et al.*, 2012). This cation site distribution assigns the proper nomenclature while minimizing the OH and Fe^{3+} effects. Amphibole in Predazzo camptonites belongs to both the ^{W}(OH, F, Cl)- and the ^{W}(O)-dominant (oxo-amphibole) groups, and to the Ca subgroup. Its composition, extremely variable between the less and the more differentiated samples, varies from pargasite to ferri-kaersutite, Ti-rich magnesio-hastingsite and Ti-rich ferro-ferri-sadanagaite (Mg# from 28 to 75; Table 2). The sadanagaitic composition is quite rare and represents the most Si-poor variety of amphibole reported from lamprophyres (Rock, 1991). In terms of CaO/Na_2O and Al_2O_3/TiO_2 ratios, most of the analyzed amphiboles are similar to those reported by Rock (1991) from alkaline lamprophyres (Fig. 6). Some crystals have a quite high Al_2O_3/TiO_2 ratio, similar to that of calc-alkaline hastingsites, but maintaining a CaO/Na_2O ratio comparable to alkaline kaersutites (Fig. 6).

Amphibole textural features and major element composition

Optical and electron microscope observations, coupled with major element chemical data, enabled us to identify the occurrence of five distinct textural types of amphibole, following a scheme analogous to that proposed for plagioclase and clinopyroxene crystals at Mt. Etna by Giacomoni *et al.* (2014; 2016).

Type 1 amphiboles (Fig. 7a) are the most common and occur both phenocrysts and in the groundmass. They have euhedral contour with homogeneous pale brown to orange rounded dissolved cores; the more differentiated is the host rock, the more elongated is the crystal shape, becoming acicular in sample MA1. *Type 1* crystals are pargasitic to Ti-rich magnesio-hastingsitic (Mg# = 71-74), usually surrounded by a reddish ferri-kaersutitic rim (Mg# =59-66)

with euhedral shape, in optical continuity with the cores. In *Type 1* crystals an intermediate magnesio-hastingsitic (Mg# = 72-74) overgrowth is often visible by means of electron microscope. Groundmass amphiboles reflect the composition of the outermost rims of the phenocrysts (ferri-kaersutite to Ti-rich magnesio-hastingsite). *Type 2* crystals (Fig. 7b), Ti-rich magnesio-hastingsitic in composition, have brown rounded cores (Mg# = 62-64), characterized by the presence of dispersed Fe-Ti oxides and melt pockets, and ferri-kaersutitic rims (Mg# = 60-68). The cores are often surrounded by magnesio-hastingsitic intermediate overgrowths analogous to those documented in *Type 1* amphiboles. Both the intermediate overgrowth and the external rim are in optical continuity with the core. *Type 3* crystals (Fig. 7c) have blackish dusty cores with euhedral edges. As in case of *Type 1* crystals, they are surrounded by Ti-rich magnesio-hastingsitic to ferri-kaersutitic rims (Mg# 53-70). *Type 4* amphiboles (Fig. 7d) are those previously defined xenocrysts. They usually are cm in size, black coloured and markedly altered, sometimes being resorbed in entire portions. Their Ti-rich magnesio-hastingsitic core (Mg# 51-62) is often pervaded by the incipient formation of fibrous minerals and micrometric veins bearing Fe-Ti oxides. The outer portions of the core present strongly dusty resorbed zones comparable to those recognized in *Type 3* crystals cores. *Type 4* xenocrysts are surrounded by a pale brown to reddish magnesio-hastingsitic to ferri-kaersutitic rim (Mg# ~68). *Type 5* amphiboles (Fig. 7e), documented only in sample MA1, occur both as phenocrysts and centimeter-scale megacrysts. They have dark brown Ti-rich ferri-sadanagaitic to Ti-rich ferro-ferri-sadanagaitic cores (Mg# = 29-39) and pale brown Ti-rich magnesio-hastingsitic rims (Mg# 68-72), grown in optical continuity. With respect to *Type 4* xenocrysts, megacrysts are identified by their euhedral habitus and the absence of resorption/alteration features. It should be noticed that, although important indicators of the physico-chemical conditions of the magmatic system, *Type 2* to *Type 5* are much rarer than *Type 1* amphiboles, rarely exceeding 1-5 vol.% of the specimens.

Amphibole trace element composition

Due to the small size and general alteration of most of the amphiboles, in situ trace element analyses were performed only on *Type 1* (both core/rim of the larger phenocrysts and smaller groundmass specimens), *Type 2* (rim) crystals and *Type 4* (core/rim) xenocrysts (Table 3). Chondrite-normalized incompatible element patterns have Ba, Sr positive spikes and Th, U and Zr negative anomalies; REE patterns are convex-upward (Fig. 8). *Type 4* amphibole core and *Type 1* groundmass crystals have the most Nb-, Zr-, Hf-, and REE-enriched composition, whereas *Type 1* phenocrysts have the less enriched patterns, relatively Zr-Hf-Nb-depleted at the core and REE-depleted at the rim. In all amphiboles, rims are generally REE-depleted with respect to the related cores (Fig. 8).

Clinopyroxene

Clinopyroxene is generally aluminian- to ferrian-titanian-diopside (Fig. 6; Table 4). Large clinopyroxene phenocrysts are typically zoned in Mg#, ranging from ~82 in the centres to 68-72 in the rims. Smaller phenocrysts have Mg# down to 64, being similar in composition to the outermost rim of the larger "atoll-like" clinopyroxene crystals. TiO_2 content reaches high values (5.2 wt%), as already highlighted by Carraro & Visonà (2003).

Clinopyroxene trace element analyses were performed on euhedral phenocrysts as well as on the outermost rims of the larger crystal with evident compositional zoning (Table 3; Fig.8) No significant trace element compositional variations are present between the smaller phenocrysts and the rims of the larger crystals.

Feldspar

From textural relationships, plagioclase and K-feldspar crystallization occurs later than olivine, clinopyroxene and amphibole. Plagioclase compositions vary from An_{74} to An_{23} (Fig. 6; Table

5). K-Feldspar, usually present as groundmass phase, becames modally and dimensionally significant in sample MA1, where it ranges in composition from Or_{54} to Or_{57} (Fig. 6; Table 5).

Fe-Ti oxides

Fe-Ti oxides are widespread in the groundmass assemblage of all camptonites and generally have TiO_2 and Al_2O_3 contents ranging from 12.1 to 19.0 wt% and from 2.3 to 7.8 wt%, respectively (Fig. 6; Table 6). Micrometer-sized Ti-magnetite crystals can be also found included in *Type 2* amphibole cores or within the reaction assemblages pervading some clinopyroxene crystals and *Type 4* amphibole xenocrysts.

CARBONATE OCELLI

Rounded ocellar structures with carbonatic composition were identified in all Predazzo camptonites. Unfortunately, the remarkable alteration of the dykes prevented any accurate evaluation of their distribution at the macro-scale. Sample MA1 is the only ocelli-free, consistently with its more differentiated character (Rock, 1991). The ocelli-hosted carbonate can be subdivided in two groups (Fig. 9; Table 7): i) dolomite-ankerite type (FeO = 5.0-14.4 wt%; MgO = 12.7-18.7 wt%); and ii) magnesite-siderite type (FeO = 27.5-39.0 wt%; MgO = 14.3-24.0 wt%). These compositions are similar to those identified by Rock (1991) for the worldwide carbonate-bearing lamprophyres (Fig. 9). SrO content is low in all carbonate types, reaching the maximum values of 0.16-0.30 wt% in some dolomite-ankerite grains; BaO was often below the EMPA detection limit. MnO content varies from 0.24 to 0.62 wt%. Some of the ocelli are texturally composite, including both smaller dolomite-ankerite crystals and larger well-developed magnesite-siderite ones, the latters mainly occurring in the inner portions; some others are instead constituted of sole dolomite-ankerite crystals (Fig. 9).

An intriguing topic in the study of carbonates in magmatic rocks is the determination of their primary (carbonatitic) or secondary (hydrothermal) origin. If the carbonate ocelli are derived

from a melt, the relationship between lamprophyric and carbonatitic melts would be strengthened by Predazzo camptonites, and liquid immiscibility processes probably drove the generation of the carbonate ocelli globular structures (Rock, 1991; Le Roex & Lanyon, 1998; Leat *et al.*, 2000; Vichi *et al.*, 2005). If not, their nature would be linked to the occurrence of late-stage hydrothermal processes. From a textural point of view, carbonate ocelli in Predazzo camptonites are characterized by: i) spherical shape, easily distinguishable from secondary-filled amygdalae, elongated in shape; ii) flow-aligned tangential growth of high-temperature-forming silicates (plagioclase, amphibole and/or clinopyroxene); and iii) lack of more typically hydrothermal minerals, such as zeolites (Fig. 9). According to Vichi *et al.* (2005) and Gozzi *et al.* (2014), all these features support the primary magmatic nature of the ocelli, and, therefore, the existence of carbonatitic-like droplets within the silicate melt.

To discriminate between primary and secondary carbonates, some authors have suggested that low SrO (<0.6 wt%) is consistent with a late-stage origin (Hay & O'Neil, 1983; Hogarth, 1989; Leat *et al.*, 2000), whereas some others suggested that carbonates with SrO >0.3 wt% and MnO >0.2 wt% can be considered primary (Vichi *et al.*, 2005). Alternatively, the magnesite-siderite carbonates in carbonatitic complexes often have low SrO contents (Buckley & Woolley, 1990; Zaitsev *et al.*, 2004). When plotting our data in a CaO/MgO vs. SrO + MnO space, which discriminates between high temperature and late-stage secondary carbonates (Vichi *et al.*, 2005), a positive correlation is displayed by most of the magnesite-siderite crystals, whereas an almost constant CaO/MgO accompanies a large scattered (SrO + MnO) sum for the dolomite-ankerite grains (Fig. 9). Such a feature is consistent with a late-stage crystallization of the magnesite-siderite crystals, and a magmatic origin for the dolomite-ankerite grains. This hypothesis is also supported by the occurrence of magnesite-siderite-free ocelli in the analyzed camptonites. A similar combination has been also recognized by Leat *et al.* (2000) in carbonate ocelli inside the Middle Jurassic lamprophyres of the Ferrar region (Antarctica): according to these authors, an earlier formation of magmatic calcite-dolomite was followed by a late-stage

deposition of Fe-rich, Sr-poor carbonates towards the core of the ocelli. Such an interpretation, well fitting both the chemical and textural features of the carbonate ocelli of Predazzo lamprophyres, lead us to hypothesize that magnesite-siderite precipitation probably occurred during late-stage hydrothermal fluid circulation, whereas dolomite-ankerite crystallization was primary (magmatic), likely derived from a carbonatitic-like melt that coexisted with the lamprophyric one. It is not clear whether these carbonatites are primary melts generated by mantle partial melting or formed by exsolution of immiscible carbonate fractions from alkaline magmas (Wallace & Green, 1988). The almost perfectly rounded shape of the analyzed ocelli seems to favour immiscibility, however further studies are required to investigate the association between carbonatites and lamprophyres in the Southern Alps subcontinental lithospheric mantle.

AGE AND ISOTOPIC SIGNATURE OF PREDAZZO CAMPTONITES

$^{40}Ar/^{39}Ar$ geochronology

The $^{40}Ar/^{39}Ar$ incremental heating method was applied to amphibole and plagioclase separates from two different camptonite samples (FF2 and FF37). Results and age spectra are shown in Fig. 10. Sample FF2 (plagioclase): The data defined a plateau (>90% ^{39}Ar, n = 16, MSWD 0.9) with an age of 218.90 ± 0.59 Ma. The younger discordant steps in the age spectrum likely related to alteration of the plagioclase. Sample FF37 (amphibole): The data defined a plateau (>50% ^{39}Ar, n = 6, MSWD 1.98) with an age of 219.70 ± 0.73 Ma. Younger apparent ages in the early steps of amphibole age spectrum, concomitant with high K/Ca ratios, were probably due to secondary alteration. The plagioclase and amphibole age are in good agreement and define a crystallisation age for the Predazzo camptonites of 219.22 ± 0.46/0.73 Ma (2σ; analytical/full systematic uncertainties).

$^{87}Sr/^{86}Sr$ and $^{143}Nd/^{144}Nd$ isotopes

Whole-rock $^{87}Sr/^{86}Sr$ and $^{143}Nd/^{144}Nd$ isotopic ratios were measured on representative samples among the Predazzo lamprophyres (Table 1). Initial isotopic ratios, respectively named $^{87}Sr/^{86}Sr_i$ and $^{143}Nd/^{144}Nd_i$, were corrected to an age of 220 Ma, in accordance with the $^{40}Ar/^{39}Ar$ dating results. Lamprophyres have $^{87}Sr/^{86}Sr_i$ values ranging between 0.7033 and 0.7040, for a $^{143}Nd/^{144}Nd_i$ range of 0.51260-0.51265 (Fig. 11). The isotopic data, in accordance to what hypothesized by Marrocchino *et al.* (2002), highlight a discrepancy between the isotopic signature of the lamprophyres and their "hosting" Predazzo Intrusive Complex (Casetta *et al.*, 2018*a*). The lamprophyres isotopic signature lies in fact between the DMM and the EM I mantle end-members, in contrast to that of the Predazzo intrusive rocks, purely EM I-like (Fig. 11).

LAMPROPHYRE DIFFERENTIATION

The differentiation processes of worldwide alkaline lamprophyres are often characterized by the occurrence, both at local (ocelli, veins, globules) and regional scale (coeval dykes/plutons), of co-magmatic intermediate/felsic rocks, mainly foid-syenitic in composition (Rock, 1987; 1991). In these samples, the Ni, Cr decrease at decreasing MgO (Fig. 3), together with the mineral phase compositional variations, are consistent with fractional crystallization. The absence of a significant interaction with crustal components during ascent/emplacement is supported by the high whole-rock MgO, Cr and Ni contents, the presence of forsteritic olivine and the initial $^{87}Sr/^{86}Sr$ and $^{143}Nd/^{144}Nd$ values that approach the DMM isotopic component. These features point towards a mantle-derived origin for our samples, in accordance with most of the worldwide alkaline lamprophyres (Rock, 1991).

The extent of fractional crystallization was estimated assuming Rayleigh distillation (e.g. Shaw, 1970). Assuming Zr as perfectly incompatible element (e.g. a mineral-melt distribution coefficient of zero), the most differentiated camptonite MA1 was generated by ~40% fractional crystallization of a starting primitive camptonitic melt. This estimate is consistent with mass balance calculations from major elements. Major element vectors (Fig. 12) show that ~35%

fractional crystallization of an assemblage made of olivine (19.1%), clinopyroxene (53.4%), amphibole (19.1%) and Ti-magnetite (8.4%) from a starting primitive camptonitic magma can in fact reproduce the MA1 composition.

T-P-fO_2 CONDITIONS OF CRYSTALLIZATION AND WATER CONTENT OF LAMPROPHYRIC MELTS

The determination of T-P-fO_2 parameters and water content of lamprophyric systems is challenging. Following Rock (1987, 1991), we assume that the whole-rock samples approximate the composition of melt + suspended crystals + volatiles. On this basis, the physico-chemical crystallization conditions of Predazzo camptonites were estimated by means of several thermo-, oxy-barometric and hygrometric equations applied to chosen mineral (clinopyroxene, Ti-magnetite, amphibole)-melt pairs. Errors related to each applied method are reported in Table 8.

Equilibrium between clinopyroxene (Cpx) phenocrysts and camptonitic melt was evaluated by means of their Fe-Mg partitioning, assuming a $^{Cpx\text{-}Liq}Kd_{Fe\text{-}Mg}$ of 0.26±0.05 (Akinin *et al.*, 2005), which ideally reflect clinopyroxene equilibrium conditions in an alkali-dominated basic melt (i.e. camptonites; Ubide *et al.*, 2014). Since most of clinopyroxene-liquid thermobarometers require as input the H_2O content of the crystallizing melt, and this parameter is highly variable in the lamprophyre system, *T* and *P* of clinopyroxene crystallization were determined by means of the single-mineral H_2O-independent equations 32a and 32d of Putirka (2008), in turn derived by the *T*-dependent barometer and the *P*-independent thermometer of Putirka *et al.* (1996). This rational scheme enabled us to retrieve the *T-P* path of clinopyroxene crystallization without implying any circular reference. The equilibrium between amphibole (Amp) crystals and the camptonitic melts was evaluated by means of the *T*- and *P*-independent $^{Amp\text{-}Liq}Kd_{Fe\text{-}Mg}$ exchange coefficient, which should be 0.28±0.11 in conditions of equilibrium (Putirka, 2016). The H_2O content of the melt from which amphibole crystallized was calculated by the single-mineral

hygrometer of Ridolfi *et al.* (2010). Afterwards, the *T*-*P* conditions of amphibole crystallization were calculated by means of the amphibole-melt *P*-independent thermometer (Equation 5) and the *T*-independent, H_2O-dependent barometer (Equation 7b) of Putirka (2016). In this latter equation, the H_2O values obtained by the Ridolfi *et al.* (2010) hygrometer were used as input. The oxygen fugacity of the magmatic system was calculated by means of the oxy-barometer of Ishibashi (2013), based on the Fe^{2+}/Fe^{3+} partitioning between spinel and melt.

Clinopyroxene and Ti-magnetite crystallization conditions

Equilibrium check results indicated that most of the clinopyroxene phenocrysts were not in equilibrium with the high Mg# (59-65) camptonitic melts ($^{Cpx\text{-}Liq}Kd_{Fe\text{-}Mg}$ = 0.32-0.96), requiring instead a more evolved melt to attain equilibrium (Mg# 44-49). The disequilibrium is also supported by the compositional zoning between cores (Mg# 82) and rims (Mg# 68) of many crystals, as well as by the dusty reaction zones of the larger phenocrysts. The few crystals attaining equilibrium belong to slightly more evolved camptonitic samples ($^{Cpx\text{-}Liq}Kd_{Fe\text{-}Mg}$ = 0.17-0.40). Thermobarometric results indicate that clinopyroxene in equilibrium with their host rock composition crystallized at *P* of 490±180 MPa and *T* of 1087±27°C (Table 8). According to these ranges, *T*-*P* values of 1100-1050°C and 500 MPa were considered to apply the Ishibashi (2013) oxy-barometer to Ti-magnetite crystals. Results yielded a fO_2 interval of -8.3/-10.0 log fO_2 at 1100°C, and a -9.4/-11.0 log fO_2 range at 1050°C (between -1 and +1 FMQ; Table 8).

Amphibole crystallization conditions

Amphibole crystals in the less evolved camptonite resulted not in equilibrium with their host rock composition, having an $^{Amp\text{-}Liq}Kd_{Fe\text{-}Mg}$ of 0.42-0.89. On the other side, equilibrium was attained by some crystals in the more evolved MA1 sample ($^{Amp\text{-}Liq}Kd_{Fe\text{-}Mg}$ = 0.29-1.0). As expected, *Type 4* xenocrysts and *Type 5* amphiboles cores yielded extreme disequilibrium conditions, with $^{Amp\text{-}Liq}Kd_{Fe\text{-}Mg}$ values as high as 1.94.

The Ridolfi *et al.* (2010) hygrometer indicates that *Type 1*, *Type 2* and *Type 3* amphiboles crystallized at water contents of 7.3±0.3 wt% in the less evolved camptonitic melt, and 6.8±0.7 wt% in the more differentiated one (Table 8). Higher values were calculated for *Type 4* xenocrysts and *Type 5* amphibole cores, which yielded H_2O contents up to 9.8 wt%. By considering only the crystals in equilibrium with their host rock composition, a range of 6.4±0.3 H_2O wt% is obtained. Putirka (2016) thermobarometers yielded *T-P* intervals of 1074-927°C and 1230-470 MPa for all amphibole crystals (Table 8). The highest *P* were calculated for *Type 4* xenocrysts (1190±50 MPa) and *Type 5* amphiboles cores (1030±50 MPa), at corresponding crystallization *T* of 1037±21°C and 952±21°C, respectively (Table 8). It is worth noting that, due to the significant disequilibrium between *Type 4* and *Type 5* crystals and the melt, these values should be considered with caution. By taking into account only the crystals in equilibrium with the host rock, *T-P* ranges of 1027±12°C and 600±60 MPa are obtained. These values can likely represent the shallower amphibole crystallization conditions in the magmatic system. The deeper crystallization conditions can be instead roughly approached by some *Type 1*, *Type 2* and *Type 3* crystals close to the equilibrium with the host camptonite ($^{Amp\text{-}Liq}Kd_{Fe\text{-}Mg}$ = 0.42-0.46), which yield *P* and *T* up to 1160 MPa and 1067°C. In any case, the obtained *T-P* ranges are consistent with the experimental simulations proposed by Pilet *et al.* (2010), who demonstrated that kaersutite crystallization can start at 1130°C and 1.5 GPa in volatile-enriched (5-6 H_2O wt%) basanitic melts, thus in conditions similar to those of Predazzo camptonites. If combined to the thermobarometric results obtained by clinopyroxene, these *T-P* values suggest that crystallization in the lamprophyric system occurred continuously between 690 and 230 MPa, at *T* decreasing from 1124 to ~1000°C, with an H_2O content ≥ 6.4±0.3 wt%.

Interpretation of amphibole textures

A correlation between the obtained *T-P* and H_2O results and the previously identified textures enable us to infer amphibole crystallization processes. The homogeneous composition of *Type*

1 amphibole cores, close to the equilibrium with the less evolved melt ($^{Amp\text{-}Liq}Kd_{Fe\text{-}Mg}$ = 0.42-0.58) records a growth at high *T-P* (1057±12°C; 980±50 MPa), and 7.5±0.3 H_2O wt% in the melt. The crystallization of *Type 1* crystals continued during differentiation of the melt towards more evolved compositions (MA1 sample), where crystals attain equilibrium ($^{Amp\text{-}Liq}Kd_{Fe\text{-}Mg}$ = 0.32-0.36), at *T-P* down to 1013±34°C and 740±120 MPa, and water content of 7.3±0.9 wt%. *Type 2* crystal cores, in marked disequilibrium with the melt ($^{Amp\text{-}Liq}Kd_{Fe\text{-}Mg}$ = 0.73-0.80), record crystallization *T* and *P* of 1004±3°C and 900±10 MPa, at 7.0±0.1 H_2O wt%. The rounded shape of both *Type 1* and *Type 2* cores reflects an event of dissolution after reaction with a melt undersaturated in amphibole. Subsequently, the melt differentiated and re-saturated in amphibole, allowing the precipitation of the rims at lower *T-P* (1048±15°C, 750±110 MPa *Type 1*; 1029±24°C and 750±20 MPa *Type 2*) and H_2O content (6.9±0.3 wt%; Fig. 7). The magnesio-hastingsitic overgrowth in both *Type 1* and *Type 2* crystals, similar to the diopsidic bands identified by Petrone *et al.* (2018) in clinopyroxenes from Stromboli volcano (Aeolian Islands), probably formed in response of new pulse of primitive melts that introduced additional high *T* components (Mg and Ca) in the magmatic system. An abrupt *T* increase (from 1051 to 1071°C) is recorded in this intermediate overgrowth (Figg. 7a and 7b), which can provide the evidence of small-scale mixing dynamics between differentiated and primitive batches inside the magmatic system. Dusty zones of *Type 3* amphibole cores formed as result of pseudomorphic replacement by interface-coupled dissolution-precipitation processes, resulting in Ti-magnetite, plagioclase and clinopyroxene formation at the interface (Ruiz-Agudo *et al.*, 2014). The overgrowth of a newly formed rim in *Type 3* crystals is likely concomitant with the formation of *Type 1* and *Type 2* rims. *Type 3* rim, in fact, approaches the equilibrium towards the more evolved camptonitic melt ($^{Amp\text{-}Liq}Kd_{Fe\text{-}Mg}$ = 0.34-0.69). Its crystallization conditions are the following: *T* = 1017±40°C; *P* = 760±120 MPa; melt H_2O content = 7.2±0.4 wt%. *Type 4* xenocrysts probably represent relicts of larger crystals of deep crustal origin, brought to the surface by the ascent of lamprophyres. The incipient alteration and resorption features of their

cores suggest disequilibrium with the hosting melt, as also confirmed by the high $^{Amp\text{-}Liq}Kd_{Fe\text{-}Mg}$ (1.22). Their dusty portions probably formed as consequence of interface-coupled dissolution-precipitation. The outermost rim, compositionally analogous to most phenocryst rims and groundmass crystals (*Type 1, Type 2* and *Type 3*) represent a late overgrowth approaching the equilibrium with the melt ($^{Amp\text{-}Liq}Kd_{Fe\text{-}Mg}$ down to 0.61), as evidenced by the crystallization *T* (1051±9°C), *P* (1180±50 MPa) and H_2O (8.6±0.3 wt%). The sharp edges and optical continuity between *Type 5* amphiboles core and rim, as well as the absence of resorption zones, suggest that this texture is a consequence of a magnesio-hastingsitic overgrowth around preexisting sadanagaitic (Mg# = 29-39) crystals (Fig. 7e). The high $^{Amp\text{-}Liq}Kd_{Fe\text{-}Mg}$ of the cores (1.18 to 1.94) indicates significant disequilibrium with respect to the host rock composition, implying that they would attain equilibrium only in an extremely differentiated melt. The related thermobarometric results, which should be considered with caution, suggest high *P* (1030±50 MPa) and low *T* (952±21°C) of crystallization, at high water content (up to 9.8 wt%). The peculiar composition of *Type 5* cores, rare even in lamprophyres (Rock, 1991), makes it difficult to clearly define their origin, deserving further studies. *Type 5* rims represent a subsequent growth in equilibrium with the melt ($^{Amp\text{-}Liq}Kd_{Fe\text{-}Mg}$ = 0.29-0.55), at *T* of 1015±18°C, *P* of 570±60 MPa and H_2O content down to 5.8 wt%.

The observed simple dissolution and pseudomorphic replacement textures indicate a very dynamic regime of the lamprophyres magmatic system. Chemical zoning associated with dissolution-reprecipitation textures suggest that amphibole stability was affected by *T* changes due to small scale mixing between variably differentiated and/or volatile-rich melts. The repeated occurrence of such small-scale mixing processes resulted in fact in multiple and abrupt changes of amphibole liquidus conditions during lamprophyre differentiation.

LAMPROPHYRE MANTLE SOURCE AND MELTING MODEL

An intriguing topic is the nature of the mantle source from which Predazzo lamprophyres were generated, especially in the light of their HFSE/REE distribution and Sr-Nd isotopic signature. Indirect evidence of the minimum depth of segregation is provided by the lherzolite xenoliths, which record a re-equilibration process at about 45 km of depth, in the spinel stability field (Carraro & Visonà, 2003). The Zr/Y (6-11), Lu/Hf (0.07-0.12) and Dy_N/Yb_N (1.1-1.7) ratios of Predazzo lamprophyres suggest that garnet played a significant role during melting in their mantle source, as also suggested by Pinzuti *et al.* (2013) for Asal Rift magmas. However, the La_N/Yb_N and Gd_N/Yb_N ratios of the less evolved camptonites are not very high, suggesting that their source differs from those of the "typical" alkaline lamprophyres and OIB magmas (Sun & McDonough, 1989; Rock, 1991). According to the Sr-Nd isotopic data (Fig. 11), lamprophyres were generated by a depleted mantle, as also confirmed by the Nb/La vs. La/Yb diagram of Smith *et al.* (1999), which indicates that an asthenospheric contribution was required for their generation (Fig. 13a).

On the basis of these constraints, we modelled the nature of the mantle domain from which Predazzo lamprophyres were segregated by non-modal batch melting (Shaw, 1970). To account for the HFSE and REE budget of our samples, several mantle melting domains were used as starting point of our simulations. The modal composition and melting proportion of each of the considered mantle sources are reported in Table 9. A first discrimination between the role of spinel and garnet in the hypothetical source was put forward by using as starting mantle domains a spinel- and a garnet-bearing fertile lherzolites with Primordial Mantle (PM; Sun & McDonough, 1989) composition (curves II and III in Fig. 13). Consistently with the Sr-Nd isotopic data, a melting path was also proposed by using as starting source a depleted mantle composition (DMM; Workman & Hart, 2005; curve I in Fig. 13). The obtained melting curves suggest that none of the chosen starting components were able to reproduce the Sm/Yb ratio of Predazzo lamprophyres (Fig. 13). Their Gd/Yb ratio was better approximated by the melting curve of the garnet-bearing source, even if the match was not perfect (curve III in Fig. 13).

Consequently, amphibole and/or phlogopite were introduced as additional components of the starting mantle domains in our simulations. The calculated curves showed that garnet-amphibole- (curve V), garnet-phlogopite- (curve VI) and garnet-spinel-amphibole-bearing (curve IV) sources are able to account for the Sm/Yb and Gd/Yb ratios of our samples (Fig. 13), though the garnet-phlogopite-lherzolite assemblage was not able to reproduce the HREE systematics. Among the melting trends of garnet-amphibole- and the garnet-spinel-amphibole-bearing sources, the former better reproduced the features of the less evolved camptonites, both in the Sm/Yb, La/Yb and Gd/Yb ratios and in the REE pattern (Fig. 13d). Accordingly, we suggest that the Predazzo lamprophyres could have been generated by low melting percentages (1.0 to 2.5%) of a garnet-amphibole-bearing lherzolite, with a fertile PM starting composition (Sun & McDonough, 1989).

Such mantle source modal composition and melting degrees are similar to those proposed by Batki *et al.* (2014) for the generation of Ditrau lamprophyres (1-4% partial melting). However, the mantle source composition required by Predazzo lamprophyres is more depleted than the Ditrau one, being this latter a REE-enriched mantle with significant contribution of asthenospheric HIMU-OIB-like components (EAM, Seghedi *et al.*, 2004; Batki *et al.*, 2014). The presence of a LILE- and volatiles-enriched garnet-bearing mantle source with an asthenospheric signature was also proposed by Stoppa *et al.* (2014) to model the genesis of the Cretaceous to Oligocenic alkaline/ultramafic lamprophyres of Central-Southern Italy, whose REE patterns are strongly LREE-enriched and HREE-depleted with respect to the Predazzo ones. The involvement of amphibole and garnet during melting was required to simulate the relatively low LREE/HREE ratios of Predazzo lamprophyres, as well as to get rid of their H_2O-CO_2-alkali-rich nature. Considering that the spinel-garnet transition in a continental lithospheric setting occurs at 60-90 km (2-3 GPa; Takahashi & Kushiro, 1983; Falloon & Green, 1988; Kinzler & Grove, 1992; Robinson & Wood, 1998; Pinzuti *et al.*, 2013), we can constrain the melting region of Predazzo lamprophyres to >60 km depth. Amphibole stability in the mantle

is limited to ~3 GPa (Frost, 2006; Fumagalli *et al.*, 2009; Tumiati *et al.*, 2013; Mandler & Grove, 2016), suggesting that the mantle source depth is <90 km. Based on these constraints, we suggest that a depth of 70-80 km is most likely for the source region of these camptonites. Similar depths are also consistent with those proposed by Hammouda & Keshav (2015), according to whom carbonatite and silicate melts can coexist between 2 and 2.6 GPa (ca. 60-80 km) along the convecting mantle adiabat (asthenosphere).

GEODYNAMIC IMPLICATIONS

The magmatism of the Dolomitic Area

The late-stage occurrence of alkaline lamprophyric dykes in intrusive complexes often acquires a double significance, since they do not only act as younger chronological boundary of the magmatic episodes, but they also constitute the most primitive (and least contaminated by the crust) magma types (Rock, 1991). In the case of the Predazzo area, several authors suggested a close relationship between the alkaline lamprophyres and the host pluton (Lucchini *et al.*, 1969; 1982; Carraro & Visonà, 2003). The new $^{40}Ar/^{39}Ar$ age results (from 218.90 ± 0.59/0.66 to 219.70 ± 0.73/0.85 Ma; Fig. 10) lead us to point out that the lamprophyric rocks belong to a distinct magmatic pulse that occurred about 17-20 Ma later than the emplacement of the Predazzo Intrusive Complex (U-Pb zircon age of 238.075 ± 0.087 Ma, Storck *et al.*, 2018). Moreover, since the entire Ladinian volcano-plutonic event in the Dolomitic Area has a limited duration (from 239.04±0.04 to 237.77±0.05 Ma; Brack *et al.*, 1996; Mundil *et al.*, 1996; Mietto et al., 2012; Abbas *et al.*, 2018; Storck *et al.*, 2018; Wotzlaw *et al.*, 2018), it is evident that the lamprophyres represent a distinct magmatic event. This chronological gap is also reinforced by the geochemical discrepancies: despite showing a K-affinity comparable to that of the high-K calc-alkaline to shoshonitic volcano-plutonic rocks of the entire Dolomitic Area (Bonadiman *et al.*, 1994; Casetta *et al.*, 2018*a*; 2018*b*), camptonites have peculiar trace element profiles and Sr-Nd isotopic signature (Figg. 4 and 11). In fact, whereas the Ladinian high-K calc-alkaline to

shoshonitic rocks display the typical subduction-related incompatible element patterns, alkaline lamprophyres lack any Ta-Nb-Ti and U-Th negative anomaly, suggesting the involvement of an OIB-like component in their mantle source. The $^{87}Sr/^{86}Sr_i$ and $^{143}Nd/^{144}Nd_i$ signature of Predazzo camptonites points towards a genesis from a mantle source more depleted than the EM I-like source that produced the Ladinian high-K calc-alkaline to shoshonitic rocks. As shown in Fig. 11, in fact, they plot close to the DMM end-member (Workman & Hart, 2005), suggesting that a significant contribution of the asthenospheric mantle was involved in their genesis. This feature confirms a time-related progressive depletion of the mantle source beneath the Dolomitic Area during Middle-Late Triassic, as already hypothesized for the source of Predazzo Intrusive Complex by Casetta *et al.* (2018*a*). Our study indicates that the magmatic activity in the Dolomitic Area was not confined to the Ladinian, but re-activated at about 218.5-220.5 Ma, with the emplacement of a small alkaline pulse generated from a $^{143}Nd/^{144}Nd$-enriched mantle domain. At shallow depth, the ascent of such small melts was probably favoured by extensional-transtensional dynamics, to which lamprophyres are often associated (e.g. Scarrow *et al.*, 2011, and reference therein). The (if any) relationships between Predazzo lamprophyres and the Triassic NE-SW transtensive-transpressive regimes of the Dolomitic Area (Doglioni, 2007; Doglioni & Carminati, 2008; Abbas *et al.*, 2018), however, has never been investigated, and requires further studies, especially in the light of the new age data. The occurrence of extensional dynamics during lamprophyres ascent is also implied by the amphibole and clinopyroxene *T-P* path of crystallization. In contrast to the Ladinian magmatic event, when the crystallization of the high-K calc-alkaline to shoshonitic melts occurred preferentially in batches located at shallow crustal depths (1.4-5.6 km; Casetta *et al.*, 2018*a*), lamprophyres crystallization started at 24 km (considering a $\Delta P/\Delta z$ of 29 MPa/km) and continued towards the surface (at least until 8 km). Such a condition is consistent with the presence of a polybaric vertical plumbing system and suggests that the fractional crystallization and (small-scale) mixing processes recorded by amphibole crystals took place en route to the

surface, without implying the presence of a magma chamber. This hypothesis, fostered by the presence of mantle xenoliths in few Predazzo camptonites, further suggest that lamprophyres are unrelated to the host plutonic complex.

Late-stage magmas or alkaline precursors?

When considered at a geodynamic scale, the significance of Predazzo lamprophyres is intriguing, since several magmatic episodes with variable geochemical affinity shaped the Southalpine-Austroalpine and Carnic-Dinaric domains from Permian to Middle-Late Triassic. The most similar and chronologically closer magmatic occurrence was documented in the Ditrau Alkaline Massif (Carpathians), where late-stage alkaline lamprophyres (camptonites) intruded a Middle-Triassic (231-227 Ma) alkaline intrusion (Dallmeyer *et al.*, 1997; Morogan *et al.*, 2000; Pana *et al.*, 2000; Batki *et al.*, 2014; Pál-Molnár *et al.*, 2015). The major and trace elements and isotopic similarities between the Ditrau lamprophyres and the host pluton led to interpret them as the parental magmas of the intrusive suite (Batki *et al.*, 2014). Such a model cannot be applied to the Predazzo case, where the geochronological and geochemical discrepancies between the alkaline lamprophyres and the plutonic complex rule out any possible correlation between camptonites and the trachybasaltic/shoshonitic rocks. Notwithstanding a slight relative depletion in Th, U, Nb, Zr and LREE with respect to the Ditrau lamprophyres, Predazzo lamprophyres have comparable Sr-Nd isotopic signature (Figg. 4 and 11), suggesting that similar mantle sources were involved in their genesis. According to Batki *et al.* (2014), Ditrau lamprophyres were generated in an early extensional phase of the Middle Triassic to Jurassic rifting that separated the Getic microplate from the Bucovinian margin (Batki *et al.*, 2014), thus representing the Alpine Tethys rift portion located northward of the Meliata basin (Stampfli *et al.*, 2002; Stampfli, 2005). Precursors of the Tethyan opening were also documented in the Brescian Alps, not far from the Dolomitic Area, where intra-plate tholeiitic

lavas and dykes with depleted Sr-Nd isotopic signature emplaced almost simultaneously with the Predazzo lamprophyres, at about 217±3 Ma (Cassinis *et al.*, 2008).

Coeval magmatic occurrences were also recognized in the Western Alps, where alkaline dykes, generated by an upwelling mantle with significant asthenospheric contribution, emplaced in the Finero area between 190-212.5 and 225±13 Ma (Stähle *et al.*, 1990; 2001; Schaltegger *et al.*, 2015). Moreover, ages of 215±35 Ma and 220±4 Ma were determined by Morishita *et al.* (2008) and Malitch *et al.* (2017), respectively, for the formation of the metasomatic apatite-rich and chromitite layers in the Finero peridotite. This temporal overlap, bolstered by the similar Sr-Nd isotopic systematics between the alkaline dykes and the apatite-rich layers (Fig. 11), led several authors (Ferrario & Garuti, 1990; Morishita *et al.*, 2003; 2008; Zaccarini *et al.*, 2004) to associate all these occurrences to a unique alkaline-carbonatitic magmatic event. The generation of such H_2O-CO_2-rich fluids was attributed to mantle upwelling dynamics in a continental rifting setting (Zaccarini *et al.*, 2004). Further evidence of an intimate association between alkaline and carbonatitic magmas in the Western Alps has been recently provided by Galli *et al.* (2019), who documented the existence of alkaline-carbonatitic bodies with emplacement age of 185-195 Ma throughout the Ivrea zone.

The 219.22 ± 0.73 Ma occurrence of alkaline lamprophyres at Predazzo can be easily incorporated in such a context, taking into account that their Sr-Nd isotopic signature totally overlap those of the alkaline dykes and the apatite-rich layers at Finero (Fig. 11; Stähle *et al.*, 1990; 2001; Morishita *et al.*, 2008). The less differentiated alkaline dykes intruded at Finero (Stähle *et al.*, 2001) are also characterized by trace element patterns comparable to those of Predazzo lamprophyres, except for Nb, Ta and Zr, slightly enriched in the formers. A marked U-Th depletion characterizes both Predazzo lamprophyres and the alkaline dykes at Finero, and their REE patterns almost totally overlap. Furthermore, the Sr-Nb enrichment of Predazzo lamprophyres matches the main features of the apatite-bearing assemblages at Finero (Zanetti *et al.*, 1999), confirming the involvement of a carbonate-rich component in their genesis. This

parallelism is also supported by the presence, in Predazzo camptonites, of carbonate ocelli with a dolomite-ankerite composition comparable to that of the interstitial dolomite grains in the Finero peridotite (Zanetti *et al.*, 1999).

According to our findings, Predazzo lamprophyres can be considered as an expression of the 190-225 Ma alkaline-carbonatitic magmatism that intruded the subcontinental mantle portion beneath the Southern Alps (Ferrario & Garuti, 1990; Stähle *et al.*, 1990; 2001; Zanetti *et al.*, 1999; Morishita *et al.*, 2003; 2008; Zaccarini *et al.*, 2004; Matsumoto *et al.*, 2005; Raffone *et al.*, 2006; Schaltegger *et al.*, 2015; Malitch *et al.*, 2017). This magmatic pulse, characterized by a mantle-upwelling signature, is distinguished from the previous, subduction-related, K- and LILE-rich metasomatic episode that produced amphibole and phlogopite in the Finero peridotite (Fig. 11; Coltorti & Siena, 1984; Morishita *et al.*, 2003; 2008; Malitch *et al.*, 2017). According to the U-Pb zircon ages (190-180 Ma and 230-180 Ma) proposed by Zanetti *et al.* (2016) and Langone *et al.* (2018), the alkaline-carbonatitic metasomatism affected the subcontinental mantle immediately prior to its exhumation, which was precisely related to the extensional stages of the Alpine Tethys rift.

Rather than to a late-stage episode connected to the Middle Triassic high-K calc-alkaline to shoshonitic (orogenic) magmatism, the generation of Predazzo lamprophyres should be considered, together with the Ditrau lamprophyres, the Brescian Alps basalts and the Ivrea alkaline-carbonatitic magmas, as a Late Triassic precursor of the Alpine Tethys rifting event. This hypothesis is supported by their depleted Sr-Nd isotopic signature, consistent with a genesis from a mantle source influenced by an asthenospheric contribution (Fig. 11). Further evidence is given by the incompatible elements pattern of the alkaline lamprophyres that, when compared to the Ladinian shoshonitic rocks of the Dolomitic Area, appear depleted in U, Th, K and La, more than enriched in Nb and Ta (Fig. 4). Such a feature is consistent with the progressive shift of the magmatism from orogenic-like to anorogenic, and thus to a progressive

evolution of the subcontinental mantle source towards a more depleted, asthenospheric-related nature.

CONCLUSIVE REMARKS

The petrological, geochronological and isotopic study of the Predazzo alkaline lamprophyres enabled us to provide new insights on the geodynamic evolution of the Dolomitic Area and the Southern Alps during Middle-Late Triassic. The most relevant findings can be summarized as follows:

1. The compositional spectrum of Predazzo alkaline lamprophyres (camptonites) can be explained by assuming 35-40% fractional crystallization of olivine, clinopyroxene, amphibole and Ti-magnetite from an initial primitive camptonitic melt.
2. Amphibole textural and compositional features suggest that the lamprophyre magmatic system was subjected to small scale mixing between variably differentiated and/or volatile rich melts during differentiation. Moreover, the occurrence, composition and textural features of carbonate-bearing ocelli suggest that a carbonatitic melt was intimately associated to the alkaline lamprophyric one.
3. $^{40}Ar/^{39}Ar$ ages of Predazzo alkaline lamprophyres demonstrated that they were emplaced at 219.22 ± 0.73 Ma (Late Triassic; $^{40}Ar/^{39}Ar$; 2σ; full systematic uncertainties), suggesting an origin unrelated to the short-lived Ladinian high-K calc-alkaline to shoshonitic magmatism of the Predazzo-Mt. Monzoni intrusions in the Dolomitic Area.
4. The difference between alkaline lamprophyres and the host Ladinian rocks is illustrated by the absence of Ta-Nb-Ti negative anomalies, the presence of U-Th negative peaks, and their HFSE distribution, which point towards a genesis in an intra-plate geodynamic setting, from a garnet-bearing mantle source. This is also confirmed by their Sr-Nd isotopic systematics, which are consistent with a depleted mantle contribution in their source, in contrast to the

pure EM I-like signature of the Predazzo-Mt.Monzoni Ladinian intrusions, which was ascribed to a subduction-modified mantle.

5. Thermo-, oxy-barometric and hygrometric calculations based on clinopyroxene, amphibole and Ti-magnetite composition suggest that the crystallization in the lamprophyre magmatic system occurred at least between 690 and 230 MPa, a *T* decreasing from 1124 to ~1000°C. The oxygen fugacity of the magmatic system varied between -1 and +1 FMQ, whereas the H_2O content of the lamprophyric melts resulted ≥ 6.4±0.3 wt%, decreasing with decreasing temperature. These results strengthen the distinction between lamprophyres and the Ladinian high-K calc-alkaline to shoshonitic magmatism: whereas the latter was dominated by crystallization processes at shallow crustal levels (1.4-5.6 km; Casetta *et al.*, 2018), lamprophyres started crystallizing at about 24 km and continued towards the surface, probably in an extensional-transtensional tectonic regime.
6. Mantle melting models suggest that low melting percentages (1.0-2.5%) of a fertile garnet-amphibole-bearing lherzolite can account for the generation of Predazzo lamprophyres. The melting region was probably located between 70 and 80 km of depth.
7. Predazzo lamprophyres are temporally, spatially and geochemically correlable to several magmatic occurrences of the Southern Alps-Carpathians area: i) the Ditrau alkaline lamprophyres (Batki *et al.*, 2014); ii) the Brescian Alps intra-plate tholeiitic lavas and dykes (Cassinis *et al.*, 2008); and iii) the alkaline dykes, apatite-rich and chromitite layers in the Ivrea zone (Ferrario & Garuti, 1990; Stähle *et al.*, 1990; 2001; Morishita *et al.*, 2003; 2008; Zaccarini *et al.*, 2004; Schaltegger *et al.*, 2015; Malitch *et al.*, 2017; Galli *et al.*, 2019). A further geochemical and geochronological comparison with the alkaline magmas at Karawanken (Austroalpine domain, Visonà & Zanferrari, 2000) is instead required, since the only available age data for this complex (230±9 Ma, Lippolt & Pidgeon, 1974) overlaps with both the ~237 Ma high-K calc-alkaline to shoshonitic and the 218.5-220.5 Ma alkaline lamprophyres of the Dolomitic Area.

8. Rather than a late-stage episode related to the Ladinian high-K calc-alkaline to shoshonitic magmatism of the Dolomitic Area, Predazzo lamprophyres should be considered part of the alkaline-carbonatitic magmatic pulse that intruded the Southern Alps subcontinental mantle between 225 and 190 Ma. Such a magmatic event likely represents a precursor of the rifting stage connected to the Alpine Tethys opening, as also suggested by its asthenospheric-influenced Sr-Nd isotopic signature. The generation of such H_2O-CO_2-rich alkaline-carbonatitic melts is therefore ascribable to mantle upwelling dynamics in a continental rifting setting (Stähle *et al.*, 1990; 2001; Zaccarini *et al.*, 2004; Batki *et al.*, 2014; Schaltegger *et al.*, 2015; Galli *et al.*, 2019).
9. Predazzo alkaline lamprophyres can be considered as geochemical and geochronological markers of the shift from orogenic-like to anorogenic magmatism in the Southern Alps. Their Sr-Nd isotopic signature and incompatible elements pattern suggest that the mantle source that generated the Ladinian (~237 Ma) subduction-related magmas was progressively being depleted, during Late Triassic, by the asthenospheric influx related to the Alpine Tethys opening.

FUNDING

This work was supported by The University Institute for Higher Studies (IUSS) Mobility Research Programme of the University of Ferrara [grant numbers 570, 571] for Long Period, 2016/2017 to [FC], the Italian National Research Program [PRIN_2017 Project 20178LPCPW] to [MC] and the Italian National Research Program [PRIN_2015/prot. 20158A9] to [CB]

ACKNOWLEDGEMENTS

NERC are acknowledged for continued funding of the Argon Isotope Facility at SUERC. Alberto Zanetti is acknowledged for LAM-ICP-MS analyses. Anne Kelly, Vincent Gallagher, Ross Dymock and Jim Imlach are thanked for making the Sr and Nd isotopic analyses and the

$^{40}Ar/^{39}Ar$ measurements at SUERC. Francesco Stoppa, Matteo Masotta and Brian Upton are acknowledged for their constructive comments to an earlier version of the paper. Editor Valentin Troll is thanked for his careful editorial guidance.

REFERENCES

Abbas, H., Michail, M., Cifelli, F., Mattei, M., Gianolla, P., Lustrino, M. & Carminati, E. (2018). Emplacement modes of the Ladinian plutonic rocks of the Dolomites: Insights from anisotropy of magnetic susceptibility. *Journal of Structural Geology* **113**, 42-61.

Akinin, V. V., Sobolev, A. V., Ntaflos, T. & Richter, W. (2005). Clinopyroxene megacrysts from Enmelen melanephelinitic volcanoes (Chukchi Peninsula, Russia): application to composition and evolution of mantle melts. *Contributions to Mineralogy and Petrology* **150(1)**, 85-101.

Armienti, P., Corazzato, C., Groppelli, G., Natoli, E. & Pasquarè, G. (2003). Geological and petrographical study of Montecampione Triassic subvolcanic bodies (Southern Alps, Italy): preliminary geodynamic results. *Italian Journal of Geosciences* **2**, 67-78.

Barbieri, G., De Vecchi, G. P., De Zanche, V., Mietto, P. & Sedea, R. (1982). Stratigrafia e petrologia del magmatismo triassico nell'area di Recoaro. Guida alla geologia del Sudalpino centro-orientale. *Società Geologica Italiana - Guide Geologiche Regionali*, 179-187.

Barfod, D. N., Mark, D. F., Tait, A., Dymock, R. C. & Imlach, J. (2014). *Argon extraction from geological samples by CO2 scanning laser step-heating*. In: Jourdan, F., Mark, D.F., & Verati, C. (eds.) *Advances in $^{40}Ar/^{39}Ar$ dating: from archaeology to planetary sciences*. Geological Society of London Special Publication **378**, 79-90.

Barry, T. L., Saunders, A. D., Kempton, P. D., Windley, B. F., Pringle, M. S., Dorjnamjaa, D. & Saandar, S. (2003). Petrogenesis of Cenozoic basalts from Mongolia: evidence for the role of asthenospheric versus metasomatized lithospheric mantle sources. *Journal of Petrology* **44(1)**, 55-91.

Batki, A., Pál-Molnár, E., Dobosi, G. & Skelton, A. (2014). Petrogenetic significance of ocellar camptonite dykes in the Ditrău Alkaline Massif, Romania. *Lithos* **200**, 181-196.

Beccaluva, L., Coltorti, M., Saccani, E., Siena, F. & Zeda, O. (2005). *Triassic Magmatism and Jurassic Ophiolites at the Margins of the Adria Plate*. In: Finetti, I.R. (ed.) *Crop Project: Deep Seismic Exploration of the Central Mediterranean and Italy*. Elsevier **28**, 607-622.

Bellieni, G., Fioretti, A. M., Marzoli, A. & Visonà, D. (2010). Permo-Paleogene magmatism in the eastern Alps. *Rendiconti Lincei* **21**, S51-S71.

Beltrán-Triviño, A., Winkler, W., von Quadt, A. & Gallhofer, D. (2016). Triassic magmatism on the transition from Variscan to Alpine cycles: evidence from U–Pb, Hf, and geochemistry of detrital minerals. *Swiss Journal of Geosciences* **109(3)**, 309-328.

Bernoulli, D. & Lemoine, M. (1980). Birth and Early Evolution of the Tethys: the Overall Situation. *Mémoires du Bureau de recherches géologiques et minières* **115**, 168-179.

Bianchini, G., Natali, C., Shibata, T. & Yoshikawa, M. (2018). Basic dykes crosscutting the crystalline basement of Valsugana (Italy): new evidence of early Triassic volcanism in the Southern Alps. *Tectonics* **37(7)**, 2080-2093.

Bonadiman, C., Coltorti, M. & Siena, F. (1994). Petrogenesis and *T*-fO_2 estimates of Mt. Monzoni complex (Central Dolomites, Southern Alps): a Triassic shoshonitic intrusion in a trascurrent geodynamic setting. *European Journal of Mineralogy* **6**, 943-966.

Brack, P., Mundil, R., Oberli, F., Meier, M. & Rieber, H. (1996). Biostratigraphic and radiometric age data question the Milankovitch characteristics of the Latemar cycles (Southern Alps, Italy). *Geology* **24(4)**, 371-375.

Buckley, H. A. & Woolley, A. R. (1990). Carbonates of the magnesite-siderite series from four carbonatite complexes. *Mineralogical Magazine* **54(376)**, 413-418.

Carraro, A. & Visonà, D. (2003). Mantle xenoliths in Triassic camptonite dykes of the Predazzo Area (Dolomites, Northern Italy). *European Journal of Mineralogy* **15(1)**, 103-115.

Casetta, F., Coltorti, M., Ickert, R. B., Bonadiman, C., Giacomoni, P. P. & Ntaflos, T. (2018a). Intrusion of shoshonitic magmas at shallow crustal depth: *T–P* path, H_2O estimates, and AFC modeling of the Middle Triassic Predazzo Intrusive Complex (Southern Alps, Italy). *Contributions to Mineralogy and Petrology* **173(7)**, 57.

Casetta, F., Coltorti, M. & Marrocchino, E. (2018b). Petrological evolution of the Middle Triassic Predazzo Intrusive Complex, Italian Alps. *International Geology Review* **60(8)**, 977-997.

Cassinis, G., Cortesogno, L., Gaggero, L., Perotti, C. R. & Buzzi, L. (2008). Permian to Triassic geodynamic and magmatic evolution of the Brescian Prealps (eastern Lombardy, Italy): *Italian Journal of Geosciences* **127(3)**, 501-518.

Castellarin, A., Lucchini, F., Rossi, P. L., Selli, L. & Simboli, G. (1988). The Middle Triassic magmatic-tectonic arc development in the Southern Alps. *Tectonophysics* **146(1-4)**, 79-89.

Coltorti, M. & Siena, F. (1984). Mantle tectonite and fractionate peridotite at Finero (Italian Western Alps). *Neues Jahrbuch fur Mineralogie-Abhandlungen* **149(3)**, 225-244.

Dal Piaz, G., Bistacchi, A. & Massironi, M. (2003). Geological outline of the Alps. *Episodes* **26(3)**, 175-180.

Dallmeyer, D.R., Kräutner, H.G. & Neubauer, F. (1997). Middle-late Triassic $^{40}Ar/^{39}Ar$ hornblende ages for early intrusions within the Ditrau alkaline massif, Rumania: Implications for Alpine rifting in the Carpathian orogen. *Geologica Carpathica* **48(6)**, 347-352.

Doglioni, C. (1984). Triassic diapiric structure in the central Dolomites (Northen Italy). *Eclogae Geologicae Helvetiae* **77**, 2.

Doglioni, C. (1987). Tectonics of the Dolomites (Southern Alps, Northern Italy). *Journal of Structural Geology* **9**, 181-193.

Doglioni, C. (2007). Tectonics of the Dolomites. *Bulletin für angewandte Geologie* **12(2)**, 11-15.

Doglioni, C., & Carminati, E. (2008). Structural styles and Dolomites field trip. *Memorie Descrittive della Carta Geologica d'Italia* **82**, 301.

Ellis, B. S., Mark, D. F., Pritchard, C. J. & Wolff, J. A. (2012). Temporal dissection of the Huckleberry Ridge Tuff using the $^{40}Ar/^{39}Ar$ dating technique. *Quaternary Geochronology* **9**, 34-41.

Falloon, T. J. & Green, D. H. (1988). Anhydrous partial melting of peridotite from 8 to 35 kb and the petrogenesis of MORB. *Journal of Petrology* **1**, 379-414.

Ferrario, A. & Garuti, G. (1990). Platinum-group mineral inclusions in chromitites of the Finero mafic-ultramafic complex (Ivrea-Zone, Italy). *Mineralogy and Petrology* **41(2-4)**, 125-143.

Frost, D.J. (2006). The stability of hydrous mantle phases. *Reviews in Mineralogy and Geochemistry* **62(1)**, 243-271.

Fujimaki, H., Tatsumoto, M. & Aoki, K. I. (1984). Partition coefficients of Hf, Zr, and REE between phenocrysts and groundmasses. *Journal of Geophysical Research: Solid Earth* **89(S02)**, B662-B672.

Fumagalli, P., Zanchetta, S. & Poli, S. (2009). Alkali in phlogopite and amphibole and their effects on phase relations in metasomatized peridotites: a high-pressure study. *Contributions to Mineralogy and Petrology* **158(6)**, 723.

Galassi, B., Monese, A., Ogniben, G., Siena, F. & Vaccaro, C. (1994). Age and nature of lamprophyric dykes at Calceranica (Trento). *Mineralogica et Petrographica Acta* **37**, 163-171.

Galli, A., Grassi, D., Sartori, G., Gianola, O., Burg, J. P. & Schmidt, M. W. (2019). Jurassic carbonatite and alkaline magmatism in the Ivrea zone (European Alps) related to the breakup of Pangea. *Geology*.

Gasparotto, G. & Simboli, G. (1991). Mineralogia, petrografia e schemi evolutivi delle magmatiti triassiche del complesso di Cima Pape (Dolomiti Orientali). *Mineralogica et Petrografica Acta* **34**, 205-234.

Giacomoni, P. P., Coltorti, M., Bryce, J. G., Fahnestock, M. F. & Guitreau, M. (2016). Mt. Etna plumbing system revealed by combined textural, compositional, and thermobarometric studies in clinopyroxenes. *Contributions to Mineralogy and Petrology* **171(4)**, 34.

Giacomoni, P. P., Ferlito, C., Coltorti, M., Bonadiman, C. & Lanzafame, G. (2014). Plagioclase as archive of magma ascent dynamics on "open conduit" volcanoes: The 2001-2006 eruptive period at Mt. Etna. *Earth-Science Reviews* **138**, 371-393.

Gianolla, P. (1992). Evoluzione mediotriassica del vulcanismo di Rio Freddo (Api Giulie, Italia). *Memorie di Scienze Geologiche* **44**, 193-209.

Gozzi, F., Gaeta, M., Freda, C., Mollo, S., Di Rocco, T., Marra, F., ... & Pack, A. (2014). Primary magmatic calcite reveals origin from crustal carbonate. *Lithos* **190**, 191-203.

Hammouda, T., & Keshav, S. (2015). Melting in the mantle in the presence of carbon: Review of experiments and discussion on the origin of carbonatites. *Chemical Geology* **418**, 171-188.

Hawthorne, F. C., Oberti, R., Harlow, G. E., Maresch, W. V., Martin, R. F., Schumacher, J. C. & Welch, M.D. (2012). Nomenclature of the amphibole supergroup. *American Mineralogist* **97(11-12)**, 2031-2048.

Hay, R. L. & O'Neil, J. R. (1983). Carbonatite tuffs in the Laetolil Beds of Tanzania and the Kaiserstuhl in Germany. *Contributions to Mineralogy and Petrology* **82(4)**, 403-406.

Hogarth, D. D. (1989). *Pyrochlore, apatite and amphibole: distinctive minerals in carbonatite*. In: Bell, K. (ed.) *Carbonatites: Genesis and Evolution*. Unwin Hyman, London, 103-148.

Ickert, R. B. (2013). Algorithms for estimating uncertainties in initial radiogenic isotope ratios and model ages. *Chemical Geology* **340**, 131-138.

Ishibashi H. (2013). Spinel-melt oxygen barometry: a method and application to Cenozoic alkali basaltic magmas from the Higashi-Matsuura district, NW Kyushu. *Japan Geoscience Reports* **40**, 21-32.

Kinzler, R. J. & Grove, T. L. (1992). Primary magmas of mid-ocean ridge basalts 1. Experiments and methods. *Journal of Geophysical Research: Solid Earth* **97(B5)**, 6885-6906.

Kress, V. C. & Carmichael, I. S. (1991). The compressibility of silicate liquids containing Fe_2O_3 and the effect of composition, temperature, oxygen fugacity and pressure on their redox states. *Contributions to Mineralogy and Petrology* **108(1-2)**, 82-92.

Langone, A., Zanetti, A., Daczko, N. R., Piazolo, S., Tiepolo, M. & Mazzucchelli, M. (2018). Zircon U-Pb Dating of a Lower Crustal Shear Zone: A Case Study From the Northern Sector of the Ivrea-Verbano Zone (Val Cannobina, Italy). *Tectonics* **37(1)**, 322-342.

Leat, P. T., Riley, T. R., Storey, B. C., Kelley, S. P. & Millar, I. L. (2000). Middle Jurassic ultramafic lamprophyre dyke within the Ferrar magmatic province, Pensacola Mountains, Antarctica. *Mineralogical Magazine* **64(1)**, 95-111.

Lee, J-Y., Marti, K., Severinghaus, J. P., Kawamura, K., Yoo, H. S., Lee, J. B., & Kim, J. S. (2006). A redetermination of the isotopic abundances of atmospheric Ar. *Geochimica et Cosmochimica Acta* **70**, 4507-4512.

Le Maitre, R.W., Bateman, P., Dudek, A., Keller, J., Lameyre, L., Sabine, P. A., ... & Zanettin, B., 1989. *A classification of igneous rocks and glossary of terms: recommendations of the IUGS Commission on the Systematics of Igneous Rocks.*

Le Maitre, R. W., Streckeisen, A., Zanettin, B., Le Bas, M. J., Bonin, B., Bateman, P., … & Lameyre, J. (2002). *Igneous rocks. A classification and glossary of terms. Recommendations of the IUGS Subcomission on the Systematics of Igneous Rocks.* Cambridge University Press.

Le Roex, A. P. & Lanyon, R. (1998). Isotope and trace element geochemistry of Cretaceous Damaraland lamprophyres and carbonatites, northwestern Namibia: Evidence for plume-lithosphere interactions. *Journal of Petrology* **39(6)**, 1117-1146.

Lippolt, H. & Pidgeon, R. (1974). Isotopic mineral ages of a diorite from the Eisenkappel intrusion, Austria. *Zeitschrift für Naturforschung* **29a**.

Locock, A. J. (2014). An Excel spreadsheet to classify chemical analyses of amphiboles following the IMA 2012 recommendations. *Computers & Geosciences* **62**, 1-11.

Lu, Y. J., McCuaig, T. C., Li, Z. X., Jourdan, F., Hart, C. J., Hou, Z. Q. & Tang, S.H. (2015). Paleogene post-collisional lamprophyres in western Yunnan, western Yangtze Craton: mantle source and tectonic implications. *Lithos* **233**, 139-161.

Lucchini, F., Mezzetti, R. & Simboli, G. (1969). The lamprophyres of the area Predazzo-Monzoni: camptonites. *Mineralogica et Petrografica Acta* **15**, 109-145.

Lucchini, F., Rossi, P. L. & Simboli, G. (1982). *Il magmatismo triassico dell'area di Predazzo (Alpi Meridionali, Italia)*. In: Castellarin, A. & Vai, G. B. (eds.). *Guida alla Geologia del Sudalpino centro-orientale*. Guide Geologiche Regionali Società Geologica Italiana, 221-230.

Lugmair, G. W. & Marti, K. (1978). Lunar initial $^{143}Nd/^{144}Nd$: differential evolution of Lunar crust and mantle. *Earth and Planetary Science Letters* **39**, 349-357.

Malitch, K. N., Belousova, E. A., Griffin, W. L., Badanina, I. Y., Knauf, V. V., O'Reilly, S. Y. & Pearson, N.J. (2017). Laurite and zircon from the Finero chromitites (Italy): New insights into evolution of the subcontinental mantle. *Ore Geology Reviews* **90**, 210-225.

Mandler, B. E. & Grove, T. L. (2016). Controls on the stability and composition of amphibole in the Earth's mantle. *Contributions to Mineralogy and Petrology* **171(8-9)**, 68.

Mark, D. F., Rice, C. M., Lee, M. R., Fallick, A. E., Boyce, A., Trewin, N. H. & Lee, J. K. W. (2011a). $^{40}Ar/^{39}Ar$ dating of hydrothermal activity, biota and gold mineralization in the Rhynie hot-spring system, Aberdeenshire, Scotland. *Geochimica et Cosmochimica Acta* **75**, 555-569.

Mark, D. F., Stuart, F. M. & De Podesta, M. (2011b). New high-precision measurements of the isotopic composition of atmospheric argon. *Geochimica et Cosmochimica Acta* **75(23)**, 7494-7501.

Marrocchino, E., Coltorti, M., Visonà, D. & Thirwall, M. F. (2002). Petrology of Predazzo magmatic complex (Trento, Italy). *Geochimica et Cosmochimica Acta* **66(15a)**, A486-A486.

Matsumoto, T., Morishita, T., Matsuda, J. I., Fujioka, T., Takebe, M., Yamamoto, K. & Arai, S. (2005). Noble gases in the Finero phlogopite-peridotites, western Italian Alps. *Earth and Planetary Science Letters* **238(1-2)**, 130-145.

Mazzucchelli, M., Rivalenti, G., Brunelli, D., Zanetti, A. & Boari, E. (2009). Formation of highly refractory dunite by focused percolation of pyroxenite-derived melt in the Balmuccia peridotite massif (Italy). *Journal of Petrology* **50(7)**, 1205-1233.

McKenzie, D. A. N. & O'nions, R. K. (1991). Partial melt distributions from inversion of rare earth element concentrations. *Journal of Petrology* **32(5)**, 1021-1091.

Meschede, M. (1986). A method of discriminating between different types of mid-ocean ridge basalts and continental tholeiites with the Nb-Zr-Y diagram. *Chemical geology* **56(3-4)**, 207-218.

Mietto, P., Manfrin, S., Preto, N., Rigo, M., Roghi, G., Furin, S., Gianolla, P., Posenato, R., ... & Bowring, S.A. (2012). The Global Boundary Stratotype Section and Point (GSSP) of the Carnian Stage (Late Triassic) at Prati di Stuores/ Stuores Wiesen Section (Southern Alps, NE Italy). *Episodes* **35(3)**, 414-430.

Moore, J. M., Kuhn, B. K., Mark, D. F. & Tsikos, H. (2011). A sugilite-bearing assemblage from the Wolhaarkop breccia, Bruce iron-ore mine, South Africa: Evidence for alkali metasomatism and ^{40}Ar-^{39}Ar dating. *European Journal of Mineralogy* **23(4)**, 661-673.

Morgan, L. E., Mark, D. F., Imlach, J., Barfod, D. & Dymock, R. (2014). FCs-EK: a new sampling of the Fish Canyon Tuff ^{40}Ar/^{39}Ar neutron flux monitor. *Geological Society of London, Special Publications* **378(1)**, 63-67.

Morimoto, N. (1988). Nomenclature of pyroxenes. *Mineralogy and Petrology* **39(1)**, 55-76.

Morishita, T., Arai, S. & Tamura, A. (2003). Petrology of an apatite-rich layer in the Finero phlogopite–peridotite, Italian Western Alps; implications for evolution of a metasomatising agent. *Lithos* **69(1-2)**, 37-49.

Morishita, T., Hattori, K. H., Terada, K., Matsumoto, T., Yamamoto, K., Takebe, M., ... & Arai, S. (2008). Geochemistry of apatite-rich layers in the Finero phlogopite–peridotite massif (Italian Western Alps) and ion microprobe dating of apatite. *Chemical Geology* **251(1-4)**, 99-111.

Morogan, V., Upton, B. G. J., & Fitton, J. G. (2000). The petrology of the Ditrau alkaline complex, Eastern Carpathians. *Mineralogy and Petrology* **69(3-4)**, 227-265.

Morten, L. (1980). Mineral chemistry of ultramafic inclusions from the Predazzo volcanic rocks. Dolomite Region, north Italy. *Journal of Mineralogy and Geochemistry* **138**, 259-273.

Mukasa, S.B. & Shervais, J. W. (1999). Growth of subcontinental lithosphere: evidence from repeated dike injections in the Balmuccia lherzolite massif, Italian Alps. *Lithos* **48**, 287-316.

Mundil, R., Brack, P. & Laurenzi, M. A. (1996). High resolution U/Pb single zircon age determinations: new constraints on the timing of Middle Triassic magmatism in the Southern Alps. *Conference abstract, 78° Riunione estiva S.G.I.*

Oberti, R., Cannillo, E. & Toscani, G. (2012). How to name amphiboles after the IMA2012 report: rules of thumb and a new PC program for monoclinic amphiboles. *Periodico di Mineralogia* **81(2)**, 257-267.

Pál-Molnár, E., Batki, A., Almási, E., Kiss, B., Upton, B. G., Markl, G., ... & Harangi, S. (2015). Origin of mafic and ultramafic cumulates from the Ditrău Alkaline Massif, Romania. *Lithos* **239**, 1-18.

Pamić, J. J. (1984). Triassic magmatism of the Dinarides in Yugoslavia. *Tectonophysics* **109(3-4)**, 273-307.

Pană, D., Balintoni, I. & Heaman, L. (2000). Precise U-Pb zircon dating of the syenite phase from the Ditrau alkaline igneous complex. *Studia UBB Geologia* **45(1)**, 79-90.

Pandey, A., Rao, N. C., Chakrabarti, R., Pandit, D., Pankaj, P., Kumar, A. & Sahoo, S. (2017a). Petrogenesis of a Mesoproterozoic shoshonitic lamprophyre dyke from the Wajrakarur kimberlite field, eastern Dharwar craton, southern India: geochemical and Sr-Nd isotopic evidence for a modified sub-continental lithospheric mantle source. *Lithos* **292**, 218-233.

Pandey, A., Rao, N. C., Pandit, D., Pankaj, P., Pandey, R., Sahoo, S. & Kumar, A. (2017b). Subduction–tectonics in the evolution of the eastern Dharwar craton, southern India: Insights from the post-collisional calc-alkaline lamprophyres at the western margin of the Cuddapah basin. *Precambrian Research* **298**, 235-251.

Pearce, J. A. (1982). *Trace element characteristics of lavas from destructive plate boundaries.* In: Thorpe E. S. (ed.) *Andesites.* New York, John Wiley and Sons **8**, 525-548.

Pearce, J. A. & Norry, M. J. (1979). Petrogenetic implications of Ti, Zr, Y, and Nb variations in volcanic rocks. *Contributions to Mineralogy and Petrology* **69(1)**, 33-47.

Pe-Piper, G. (1998). The nature of Triassic extension-related magmatism in Greece: evidence from Nd and Pb isotope geochemistry. *Geological Magazine* **135(3)**, 331-348.

Petrone, C. M., Braschi, E., Francalanci, L., Casalini, M. & Tommasini, S. (2018). Rapid mixing and short storage timescale in the magma dynamics of a steady-state volcano. *Earth and Planetary Science Letters* **492**, 206-221.

Pilet, S., Ulmer, P. & Villiger, S. (2010). Liquid line of descent of a basanitic liquid at 1.5 GPa: constraints on the formation of metasomatic veins. *Contributions to Mineralogy and Petrology* **159(5)**, 621-643.

Pinzuti, P., Humler, E., Manighetti, I. & Gaudemer, Y. (2013). Petrological constraints on melt generation beneath the Asal Rift (Djibouti) using quaternary basalts. *Geochemistry, Geophysics, Geosystems* **14(8)**, 2932-2953.

Pouchou, J. L. & Pichoir, F. (1991). *Quantitative analysis of homogeneous or stratified microvolumes applying the model "PAP"*. In: *Electron probe quantitation*. Springer US, 31-75.

Putirka, K. D., Johnson, M., Kinzler, R., Longhi, J. & Walker, D. (1996). Thermobarometry of mafic igneous rocks based on clinopyroxene-liquid equilibria, 0–30 kbar. *Contributions to Mineralogy and Petrology* **123(1)**, 92-108.

Putirka, K. D. (2008). Thermometers and barometers for volcanic systems. *Reviews in Mineralogy and Geochemistry* **69(1)**, 61-120.

Putirka, K. D. (2016). Amphibole thermometers and barometers for igneous systems and some implications for eruption mechanisms of felsic magmas at arc volcanoes. *American Mineralogist* **101(4)**, 841-858.

Raffone, N., Le Fèvre, B., Ottolini, L., Vannucci, R. & Zanetti, A. (2006). Light-lithophile element metasomatism of Finero peridotite (W Alps): a secondary-ion mass spectrometry study. *Microchimica Acta* **155(1-2)**, 251-255.

Renne, P. R., Deino, A. L., Hames, W. E., Heizler, M. T., Hemming, S. R., Hodges, K. V., Koppers, A. A. P., Mark, D. F., … & Wijbrans, J.R. (2009). Data Reporting Norms for $^{40}Ar/^{39}Ar$ Geochronology. *Quaternary Geochronology* **4**, 346-352.

Renne, P. R., Mundil, R., Balco, G., Min, K. & Ludwig, K. R. (2010). Joint determination of ^{40}K decay constants and $^{40}Ar^*/^{40}K$ for the Fish Canyon sanidine standard, and improved accuracy for $^{40}Ar/^{39}Ar$ geochronology. *Geochimica et Cosmochimica Acta* **74**, 5349-5367.

Renne, P. R., Balco, G., Ludwig, K. R., Mundil, R. & Min, K. (2011). Response to comment by W.H. Schwarz *et al.* on 'Joint determination of ^{40}K decay constants and $^{40}Ar^*/^{40}K$ for the Fish Canyon sanidine standard, and improved accuracy for $^{40}Ar/^{39}Ar$ geochronology' by P.R. Renne *et al.*, 2010. *Geochimica et Cosmochimica Acta* **75**, 5097-5100.

Ridolfi, F., Renzulli, A. & Puerini, M. (2010). Stability and chemical equilibrium of amphibole in calc-alkaline magmas: an overview, new thermobarometric formulations and application to subduction-related volcanoes. *Contributions to Mineralogy and Petrology* **160(1)**, 45-66.

Robinson, J. A. C. & Wood, B. J. (1998). The depth of the spinel to garnet transition at the peridotite solidus. *Earth and Planetary Science Letters* **164(1-2)**, 277-284.

Rock, N. M. S. (1987). The nature and origin of lamprophyres: an overview. *Geological Society of London, Special Publications* **30(1)**, 191-226.

Rock, N. M. S. (1991). *Lamprophyres*. Springer.

Rotenberg, E., Davis, D. W., Amelin, Y., Ghosh, S. & Bergquist, B. A. (2012). Determination of the decay-constant of ^{87}Rb by laboratory accumulation of ^{87}Sr. *Geochimica et Cosmochimica Acta* **85**, 41-57.

Ruiz-Agudo, E., Putnis, C. V. & Putnis, A. (2014). Coupled dissolution and precipitation at mineral–fluid interfaces. *Chemical Geology* **383**, 132-146.

Saccani, E. (2015). A new method of discriminating different types of post-Archean ophiolitic basalts and their tectonic significance using Th-Nb and Ce-Dy-Yb systematics. *Geoscience Frontiers* **6(4)**, 481-501.

Scarrow, J. H., Molina, J. F., Bea, F., Montero, P. & Vaughan, A. P. (2011). Lamprophyre dikes as tectonic markers of late orogenic transtension timing and kinematics: A case study from the Central Iberian Zone. *Tectonics*, **30(4)**.

Schaltegger, U., Ulianov, A., Müntener, O., Ovtcharova, M., Peytcheva, I., Vonlanthen, P., Vennemann, T., Antognini, A. & Girlanda, F. (2015). Megacrystic zircon with planar fractures in miaskite-type nepheline pegmatites formed at high pressures in the lower crust (Ivrea Zone, southern Alps, Switzerland). *American Mineralogist* **100(1)**, 83-94.

Schmid, M. S., Bernoulli, D., Fügenschuh, B., Georgiev, N., Kounov, A., Matenco, L., Oberhansli, R., Pleuger, J., Schefer, S., Ustaszewski, K. & Van Hinsbergen, D. (2016).

Tectonic units of the Alpine collision zone between Eastern Alps and Western Turkey: *Unpublished map*.

Schmid, S. M., Bernoulli, D., Fügenschuh, B., Matenco, L., Schefer, S., Schuster, R., Tischler, M. & Ustaszewski, K. (2008). The Alpine-Carpathian-Dinaridic orogenic system: correlation and evolution of tectonic units. *Swiss Journal of Geosciences* **101(1)**, 139-183.

Schmidt, K. H., Bottazzi, P., Vannucci, R. & Mengel, K. (1999). Trace element partitioning between phlogopite, clinopyroxene and leucite lamproite melt. *Earth and Planetary Science Letters* **168(3)**, 287-299.

Seghedi, I., Downes, H., Vaselli, O., Szakács, A., Balogh, K. & Pécskay, Z. (2004). Post-collisional Tertiary-Quaternary mafic alkalicmagmatism in the Carpathian–Pannonian region: a review. *Tectonophysics* **393**, 43–62.

Shaw, D. M. (1970). Trace element fractionation during anatexis. *Geochimica et Cosmochimica Acta* **34(2)**, 237-243.

Sloman, L. E. (1989). Triassic shoshonites from the dolomites, northern Italy: Alkaline arc rocks in a strike-slip setting. *Journal of Geophysical Research: Solid Earth* **94(B4)**, 4655-4666.

Smith, E. I., Sanchez, A., Walker, J. D. & Wang, K. (1999). Geochemistry of mafic magmas in the Hurricane Volcanic field, Utah: implications for small-and large-scale chemical variability of the lithospheric mantle. *The Journal of Geology* **107(4)**, 433-448.

Soder, C. & Romer, R. L. (2018). Post-collisional potassic–ultrapotassic magmatism of the Variscan Orogen: implications for mantle metasomatism during continental subduction. *Journal of Petrology* **59(6)**, 1007-1034.

Stahle, V., Frenzel, G., Hess, J. C., Saupé, F., Schmidt, S. T. & Schneider, W. (2001). Permian metabasalt and Triassic alkaline dykes in the northern Ivrea zone: clues to the post-Variscan geodynamic evolution of the Southern Alps. *Schweizerische Mineralogische und Petrographische Mitteilungen* **81(1)**, 1-21.

Stähle, V., Frenzel, G., Kober, B., Michard, A., Puchelt, H. & Schneider, W. (1990). Zircon syenite pegmatites in the Finero peridotite (Ivrea zone): evidence for a syenite from a mantle source. *Earth and Planetary Science Letters* **101(2-4)**, 196-205.

Stampfli, G.M. (2005). *Plate Tectonics of the Apulia-Adria Microcontinents*. In: Finetti, I. R. (ed.) *Crop Project: Deep Seismic Exploration of the Central Mediterranean and Italy*. Elsevier **28**, 747-766.

Stampfli, G. M. & Borel, G. D. (2002). A plate tectonic model for the Paleozoic and Mesozoic constrained by dynamic plate boundaries and restored synthetic oceanic isochrones. *Earth and Planetary Science Letters* **196(1)**, 17-33.

Stampfli, G. M. & Borel, G. D. (2004). *The TRANSMED transects in space and time: constraints on the paleotectonic evolution of the Mediterranean domain*. In: The TRANSMED Atlas: The Mediterranean region from crust to mantle, 53-80.

Stampfli, G. M., Borel, G. D., Marchant, R. & Mosar, J. (2002). Western Alps geological constraints on western Tethyan reconstructions. *Journal of the Virtual Explorer* **8**, 77.

Stoppa, F. (2008). *Alkaline and ultramafic lamprophyres in Italy: Distribution, mineral phases, and bulk rock data. Deep-Seated Magmatism, Its Sources and Plumes*. Publishing House of the Institute of Geography, SB RAS, 209-238.

Stoppa, F., Rukhlov, A.S., Bell, K., Schiazza, M. & Vichi, G. (2014). Lamprophyres of Italy: early cretaceous alkaline lamprophyres of southern Tuscany, Italy. *Lithos* **188**, 97-112.

Storck, J-C., Brack, P., Wotzlaw, J-F & Ulmer, P. (2018). Timing and evolution of Middle Triassic magmatism in the Southern Alps (Northern Italy). *Journal of the Geological Society* **123**.

Sun, S. & McDonough, W. F. (1989). *Chemical and isotopic systematics of oceanic basalts: implication for mantle and processes*. In: Saunders A. D. & Norry M. J. (eds.) *Magmatism in the Ocean Basins*. Geological Society, Special Publications, **42**, 313-345.

Takahashi, E. & Kushiro, I. (1983). Melting of a dry peridotite at high pressures and basalt magma genesis. *American Mineralogist* **68(9-10)**, 859-879.

Tiepolo, M., Bottazzi, P., Palenzona, M. & Vannucci, R. (2003). A laser probe coupled with ICP–double-focusing sector-field mass spectrometer for in situ analysis of geological samples and U-Pb dating of zircon. *The Canadian Mineralogist* **41(2)**, 259-272.

Traill, R. J. & Lachance, G. R. (1966). A practical solution to the matrix problem in X-ray analysis. II. Application to a multicomponent alloy system. Canadian Spectroscopy **11(3)**, 63-71.

Tumiati, S., Fumagalli, P., Tiraboschi, C. & Poli, S. (2013). An experimental study on COH-bearing peridotite up to 3.2 GPa and implications for crust–mantle recycling. *Journal of Petrology* **54(3)**, 453-479.

Ubide, T., Galé, C., Arranz, E., Lago, M. & Larrea, P. (2014). Clinopyroxene and amphibole crystal populations in a lamprophyre sill from the Catalonian Coastal Ranges (NE Spain): a record of magma history and a window to mineral-melt partitioning. *Lithos* **184**, 225-242.

Vardabasso, S. (1929). Rapporti tra attività magmatica e vicende tettoniche nella provincia petrografica di Predazzo. *Studi Trentini di Scienze Naturali* **11**.

Velde, D. (1968). Les transformations de l'olivine dans les lamprophyres et lamproites; une etude de la pilite. *Bulletin de la Société Géologique de France* **7(5)**, 601-612.

Vichi, G., Stoppa, F. & Wall, F. (2005). The carbonate fraction in carbonatitic Italian lamprophyres. *Lithos* **85(1-4)**, 154-170.

Visonà, D. & Zanferrari, A (2000). Some constraints on geochemical features in the Triassic mantle of the easternmost Austroalpine-Southalpine domain: evidence from the Karawanken pluton (Carinthia, Austria). *International Journal of Earth Sciences* **89(1)**, 40-51.

Voshage, H., Hunziker, J. C., Hofmann, A. W. & Zingg, A. (1987). A Nd and Sr isotopic study of the Ivrea zone, Southern Alps, N-Italy. *Contributions to Mineralogy and Petrology* **97**, 31-42.

Wallace, M.E. & Green, D.H. (1988). An experimental determination of primary carbonatite magma composition. *Nature* **335**, 343-346.

Whitney, D. L. & Evans, B. W. (2010). Abbreviations for names of rock-forming minerals. *American Mineralogist* **95**, 185-187.

Wood, D.A. (1980). The application of a Th-Hf-Ta diagram to problems of tectonomagmatic classification and to establishing the nature of crustal contamination of basaltic lavas of the British Tertiary Volcanic Province. *Earth and Planetary Science Letters* **50(1)**, 11-30.

Woolley, A. R., Bergman, S. C., Edgar, A. D., Le Bas, M. J., Mitchell, R. H., Rock, N. M. S. & Scott Smith, B. H. (1996). Classification of lamprophyres, lamproites, kimberlites, and the kalsilitic, melilitic, and leucitic rocks. *The Canadian Mineralogist* **34(2)**, 175-186.

Workman, R. K. & Hart, S. R. (2005). Major and trace element composition of the depleted MORB mantle (DMM). *Earth and Planetary Science Letters* **231(1)**, 53-72.

Wotzlaw, J. F., Brack, P. & Storck, J. C. (2018). High-resolution stratigraphy and zircon U–Pb geochronology of the Middle Triassic Buchenstein Formation (Dolomites, northern Italy): precession-forcing of hemipelagic carbonate sedimentation and calibration of the Anisian-Ladinian boundary interval. *Journal of the Geological Society* **175(1)**, 71-85.

Zaccarini, F., Stumpfl, E. F. & Garuti, G. (2004). Zirconolite and Zr–Th–U minerals in chromitites of the Finero complex, Western Alps, Italy: evidence for carbonatite-type metasomatism in a subcontinental mantle plume. *The Canadian Mineralogist* **42(6)**, 1825-1845.

Zack, T. & Brumm, R. (1998). *Ilmenite/liquid partition coefficients of 26 trace elements determined through ilmenite/clinopyroxene partitioning in garnet pyroxene*. In: Gurney, J. J., Gurney, J. L., Pascoe, M. D. & Richardson, S. H. (eds.) *7th International Kimberlite Conference*. Red Roof Design, Cape Town, 986-988.

Zaitsev, A. N., Sitnikova, M. A., Subbotin, V. V., Fernández-Suárez, J., Jeffries, T. E. & Wall, F. (2004). Sallanlatvi complex: a rare example of magnesite and siderite carbonatites.

Phoscorites and carbonatites from mantle to mine: the key example of the Kola Alkaline Province. *Mineralogical Society of London*, 201-245.

Zanetti, A., Giovanardi, T., Langone, A., Tiepolo, M., Wu, F. Y., Dallai, L. & Mazzucchelli, M. (2016). Origin and age of zircon-bearing chromitite layers from the Finero phlogopite peridotite (Ivrea-Verbano Zone, Western Alps) and geodynamic consequences. *Lithos* **262**, 58-74.

Zanetti, A., Mazzucchelli, M., Rivalenti, G. & Vannucci, R. (1999). The Finero phlogopite-peridotite massif: an example of subduction-related metasomatism. *Contributions to Mineralogy and Petrology* **134(2-3)**, 107-122.

Zanetti, A., Mazzucchelli, M., Sinigoi, S., Giovanardi, T., Peressini, G. & Fanning, M. (2013). SHRIMP U–Pb Zircon Triassic intrusion age of the Finero mafic complex (Ivrea–Verbano zone, Western Alps) and its geodynamic implications. *Journal of Petrology* **54(11)**, 2235-2265.

Ziegler, P. A. & Stampfli, G. M. (2001). Late Palaeozoic-Early Mesozoic plate boundary reorganization: collapse of the Variscan orogen and opening of Neotethys. *Natura Bresciana* **25**, 17-34.

Zindler, A. & Hart, S. R. (1986). Chemical geodynamics. *Annual Review of Earth and Planetary Sciences* **14**, 493-571.

FIGURE CAPTIONS

Fig. 1. (colour online)

(**a**) Map of the tectonic units of the eastern portion of the Alps (partly modified from Castellarin *et al.*, 1988; Dal Piaz *et al.*, 2003; Schmid *et al.*, 2016). LO: Ligurian Ophiolites; AM: deformed Adriatic margin; AD: Adriatic Microplate; SA: Southern Alps; DI: Dinarides; SM: Southern margin of Meliata; HB: Eoalpine High-Pressure Belt; TW: Tauern tectonic Window; EW: Engadine tectonic Window; OTW: Ossola-Tessin tectonic Window; EA: Eastern Austroalpine;

H: Helvetic domain; M: Molasse foredeep. The Middle Triassic magmatic occurrences in the Southern Alps domain are evidenced in black. They are, from west to east: Brescian Alps, Alto Vicentino, Valsugana, Dolomitic Area (identified by the circle), Carnia and Karawanken. (**b**) Simplified geological map of the Predazzo Intrusive Complex (PIC), showing the occurrence of lamprophyric dykes (modified from Casetta *et al.*, 2018*a*). SS: Shoshonitic Silica Saturated unit; SU: Shoshonitic Silica Undersaturated unit; GU: Granitic Unit. (**c**) Lamprophyric dyke intruded in the syenogranites (Sygr) at Predazzo. (**d**) Amphibole megacryst (indicated by the arrow) and (**e**) clinopyroxenitic xenolith included in the lamprophyric rocks.

Fig. 2. (colour online)

Photomicrographs in transmitted plane-polarized light of (**a**) a less evolved and (**b**) a more evolved (sample MA1) camptonite. Amp: amphibole; Cpx: clinopyroxene; Ol: olivine; Pl: plagioclase; Ti-Mag: Ti-magnetite. Mineral abbreviations following Whitney & Evans (2010).

Fig. 3. (colour online)

(**a**) K_2O vs. Na_2O diagram, (**b**) Cr vs. MgO and (**c**) Ni vs. MgO variations diagrams for Predazzo camptonites. (**d**) Al_2O_3-MgO-CaO and (**e**) $SiO_2/10$-CaO-$TiO_2\times4$ ternary diagrams showing the composition of Predazzo camptonites compared to those of worldwide alkaline lamprophyres (AL), ultramafic lamprophyres (UML) and calc-alkaline lamprophyres (CAL; data from Rock, 1991). The compositional field of Cretaceous to Oligocenic Italian lamprophyres (grey field) is also reported for comparison (data from Stoppa *et al.*, 2014).

Fig. 4. (colour online)

Chondrite-normalized (Sun & McDonough, 1989) trace element (**a**) and REE patterns (**b**) of Predazzo camptonites. The OIB pattern (Sun & McDonough, 1989), the average composition of the worldwide camptonites (Rock, 1991), Italian lamprophyres (Galassi *et al.*, 1994; Vichi

et al., 2005; Stoppa *et al.*, 2008; 2014), Ditrau lamprophyres (Batki *et al.*, 2014) and Predazzo Intrusive Complex Shoshonitic Silica Saturated (SS) and Undersaturated (SU) rocks (Casetta *et al.*, 2018a; 2018*b*) are reported for comparison.

Fig. 5. (colour online)

Trace element discrimination diagrams for Predazzo camptonites: (**a**) Th_N vs. Nb_N diagram (Saccani, 2015); (**b**) Ti/Y vs. Nb/Y diagram (Pearce, 1982); (**c**) Zr/Y vs. Zr diagram (Pearce and Norry, 1979); (**d**) Th-Hf-Ta ternary diagram (Wood, 1980); (**e**) Zr-Nb-Y ternary diagram (Meschede, 1986). Fractional Crystallization (FC) and Assimilation and Fractional Crystallization (AFC) vectors reported in (**a**) are in accordance with Saccani (2015).

Fig. 6. (colour online)

Mineral phase classification diagrams showing the composition of the main crystals of Predazzo camptonites. (**a**) Orthoclase (Or)-Albite (Ab)-Anorthite (An) ternary diagram for plagioclase and K-Feldspar; (**b**) Rutile (Rt)-Wustite (Wus)-Hematite (Hem) ternary diagram for Fe-Ti oxide; (**c**) Wollastonite (Wo)-Enstatite (En)-Ferrosilite (Fs) diagram for clinopyroxene (after Morimoto, 1988). (**d**) CaO/Na_2O vs. Al_2O_3/TiO_2 diagram for amphibole (after Rock, 1991). Compositional field of kaersutite in ultramafic (UML) and alkaline lamprophyres (AL), hastingsite in calc-alkaline lamprophyres (CAL), and K-richterite, arfvedsonite and eckermannite in lamproites (LL) are also reported in (**d**) for comparison (data from Rock, 1991).

Fig. 7. (colour online)

Photomicrographs in transmitted plane-polarized light, back scattered SEM images and core-to-rim compositional (Mg# and TiO_2) profiles of (**a**) *Type 1*, (**b**) *Type 2*, (**c**) *Type 3*, (**d**) *Type 4* and (**e**) *Type 5* amphiboles recognized in Predazzo camptonites. For each amphibole type, the determination of the water content (H_2O wt%) dissolved in the melt obtained by the equation

of Ridolfi *et al.* (2010) and the crystallization temperature (*T*°C) calculated by means of Putirka (2016) thermometer are also reported.

Fig. 8. (colour online)

Chondrite-normalized (Sun & McDonough, 1989) trace element (**a, c**) and REE (**b, d**) patterns of amphibole (Amp) and clinopyroxene (Cpx) crystals analysed in Predazzo camptonites. Solid lines: core composition; dotted lines: rim composition.

Fig. 9. (colour online)

Compositional and textural features of the carbonate ocelli inside Predazzo camptonites. (**a**) Calcite-magnesite-siderite ternary diagram and (**b**) SrO + MnO vs. CaO/MgO diagram (after Vichi *et al.*, 2005) showing the composition of carbonates from the inner and outer portions of the ocelli. Grey fields in (**a**) are referred to the composition of carbonates documented in worldwide lamprophyres (data from Rock, 1991). Dotted arrow in (**b**) represent the positive correlation between SrO + MnO and CaO/MgO, typical of low-temperature (low-*T*) carbonates (Vichi *et al.*, 2005). (**c, d, e**) Back scattered SEM images of carbonate ocelli composed of (**c, d**) both dolomite-ankerite/magnesite-siderite or (**e**) dolomite-ankerite crystals only. The flow-aligned tangential growth of amphibole, plagioclase and clinopyroxene is particularly evident in (**d**) and (**e**).

Fig. 10. (colour online)

$^{40}Ar/^{39}Ar$ age spectra for mineral separates from Predazzo camptonites, with apparent ages and K/Ca ratios spectra plotted against the cumulative percentage of ^{39}Ar released. (**a**) Age spectrum yielded by amphibole crystals from sample FF37; (**b**) age spectrum yielded by plagioclase crystals from sample FF2. Plateau ages are indicated in bold.

Fig. 11. (colour online)

$^{87}Sr/^{86}Sr$ vs. $^{143}Nd/^{144}Nd$ diagram showing the isotopic signature of Predazzo camptonites corrected to 220 Ma. Fields indicate the Sr-Nd isotopic signature of the: Finero (Voshage *et al.*, 1987), Balmuccia and Baldissero peridotites (Mukasa & Shervais 1999; Mazzucchelli *et al.*, 2009); alkaline dykes intruded in the Finero peridotite (220 Ma; Stahle *et al.*, 2001); apatite-rich layers of the Finero peridotite (215 Ma; Morishita *et al.*, 2008); Ditrau lamprophyres (220 Ma; Batki *et al.*, 2014); Predazzo Intrusive Complex (PIC) Shoshonitic Silica Saturated (SS) and Undersaturated (SU) rocks (234 Ma; Casetta *et al.*, 2018*a*). DMM (Workman & Hart, 2005) and EM I (Zindler & Hart, 1986) mantle end-members (corrected to 220 Ma) are also reported for comparison.

Fig. 12. (colour online)

(**a**) FeO vs. MgO and (**b**) Al_2O_3/TiO_2 vs. MgO diagrams showing the fractional crystallization (FC) vectors used to simulate the compositional trend of Predazzo camptonites. The dotted vectors represent the contribution of the single mineral phases during fractional crystallization; the black solid arrows represent the sum vector at 35% fractional crystallization. The relative percentages of fractionation of the single phases are also reported. Ol: olivine; Cpx: clinopyroxene; Amp: amphibole; Ti-Mag: Ti-magnetite; Pl: plagioclase.

Fig. 13. (colour online)

(**a**) Nb/La vs. La/Yb diagram (Smith *et al.*, 1999) used to discriminate between the contribution of lithosphere and asthenosphere in the mantle source of Predazzo camptonites. (**b**) Gd/Yb vs. La/Yb and (**c**) Sm/Yb vs. La/Sm diagrams for the less differentiated Predazzo camptonites. Melting curves in (**b**) and (**c**) are modelled using the non-modal batch melting equations of Shaw (1970). Starting mantle sources: I = Spl-lherzolite with DMM composition (Workman & Hart, 2005); II = Spl-lherzolite; III = Grt-lherzolite; IV = Spl-Grt-Amp-lherzolite; V = Grt-

Amp-lherzolite; VI = Grt-Phl-lherzolite. Starting REE composition of II, III, IV, V and VI sources is fertile PM of Sun & McDonough (1989). Source modal composition, melting proportions and partition coefficients for olivine, orthopyroxene, clinopyroxene, spinel, garnet, amphibole and phlogopite are reported in Table 9. (**d**) Chondrite-normalized (Sun & McDonough, 1989) REE patterns of Predazzo less differentiated camptonites compared to those simulated by partial melting of a garnet-amphibole-lherzolite (curve V) at partial melting degrees of 0.5 to 10%.

The alkaline lamprophyres of the Dolomitic Area (Southern Alps, Italy): markers of the Late Triassic change from orogenic-like to anorogenic magmatism

Running title: A Late Triassic alkaline-carbonatitic pulse in the Dolomitic Area

Federico Casetta*

Department of Physics and Earth Sciences, University of Ferrara

Via Saragat 1, 44121 Ferrara, Italy

Ryan B. Ickert

Scottish Universities Environmental Research Centre, Scottish Enterprise Technology Park, Rankine Avenue, East Kilbride, G75 0QF, UK

Darren F. Mark

Scottish Universities Environmental Research Centre, Scottish Enterprise Technology Park, Rankine Avenue, East Kilbride, G75 0QF, UK

Department of Earth & Environmental Science, University of St Andrews, St Andrews, KY16 9AJ, UK

Costanza Bonadiman**

Department of Physics and Earth Sciences, University of Ferrara

Via Saragat 1, 44121 Ferrara, Italy

Pier Paolo Giacomoni

Department of Physics and Earth Sciences, University of Ferrara

Via Saragat 1, 44121 Ferrara, Italy

Theodoros Ntaflos

Department of Lithospheric Research, Universität Wien

Althanstraße 14 (UZA II), 1090 Wien, Austria

Massimo Coltorti

Department of Physics and Earth Sciences, University of Ferrara

Via Saragat 1, 44121 Ferrara, Italy

* Corresponding author. Phone +39 0532 974721. E-mail: cstfrc@unife.it

** Corresponding author. Phone +39 0532 974720. E-mail: bdc@unife.it

The alkaline lamprophyres of the Dolomitic Area (Southern Alps, Italy): markers of the Late Triassic change from orogenic-like to anorogenic magmatism

ABSTRACT

In this paper, the first complete petrological, geochemical and geochronological characterization of the oldest lamprophyric rocks in Italy cropping out around Predazzo (Dolomitic Area) is presented, with the aim of deciphering their relationship with the Triassic magmatic events of the whole Southern Alps. Their Mg# between 37 and 70, together with their trace element content, suggest that fractional crystallization was the main process responsible of their differentiation, together with small scale mixing, as evidenced by some complex amphibole textures. Moreover, the occurrence of primary carbonate ocelli suggests an intimate association between alkaline lamprophyric magmas and a carbonatitic melt. $^{40}Ar/^{39}Ar$ data show that lamprophyres were emplaced at 219.22 ± 0.73 Ma (2σ; full systematic uncertainties), around 20 Ma after the high K calc-alkaline to shoshonitic short-lived Ladinian (237-238 Ma) magmatic event of the Dolomitic Area. Their trace element and Sr-Nd isotopic signature ($^{87}Sr/^{86}Sr_i$ = 0.7033-0.7040; $^{143}Nd/^{144}Nd_i$ = 0.51260-0.51265) is likely related to a garnet-amphibole-bearing lithosphere interacting with an asthenospheric component, significantly more depleted than the mantle source of the high K calc-alkaline to shoshonitic magmas. These features suggest that Predazzo lamprophyres belong to the same alkaline-carbonatitic magmatic event that intruded the mantle beneath the Southern Alps (i.e. Finero peridotite) between 190 and 225 Ma. In this scenario, Predazzo lamprophyres cannot be considered as a late-stage pulse of the orogenic-like Ladinian magmatism of the Dolomitic Area, but most likely represent the petrological bridge to the opening of the Alpine Tethys.

KEYWORDS

Carbonatitic alkaline lamprophyre; Amphibole texture; Camptonite; Dolomitic Area; Predazzo; Southern Alps; Triassic magmatism.

INTRODUCTION

The late-stage emplacement of lamprophyric dykes typifies a large number of plutonic complexes, providing important information of the local geodynamic evolution. According to Rock *et al.* (1987), Le Maitre *et al.* (1989), Rock (1991), Woolley *et al.* (1996) and Le Maitre *et al.* (2002), lamprophyres are defined as H_2O-, CO_2-, and alkali-rich rocks with a porphyritic texture, characterized by the compulsory presence of amphibole and/or phlogopite-biotite phenocrysts and the common occurrence of halides, carbonates, sulphides and zeolites. Feldspars and/or feldspathoids are often present in the groundmass. Mineral chemistry is by far a key factor for the identification/classification of these rocks: high-Ti, -Ba and -F amphiboles and micas, high-Al clinopyroxenes, high-Zn spinels and Fe^{3+}-rich micas are in fact diagnostic phases of lamprophyres. The genesis of lamprophyres is commonly attributed to partial melting of a metasomatised mantle (Rock, 1991; Stoppa *et al.*, 2014; Pandey *et al.*, 2017*a*; 2017*b*; Soder & Romer, 2018), while their emplacement is usually associated with the onset of lithospheric extensional-transtensional tectonic regimes. Lamprophyres are often associated with strike-slip movements, and may mark a change in the geodynamic regime (Scarrow *et al.*, 2011). Following Le Maitre *et al.* (2002), lamprophyric rocks are grouped, on the basis of their mineralogy, into three associations: i) minette-kersantite; ii) vogesite-spessartite; and iii) sannaite-camptonite-monchiquite. This discrimination partially reflects what was originally proposed by Le Maitre *et al.* (1989) and Rock (1991), according to whom the first two associations belong to the "calc-alkaline (shoshonitic) lamprophyres", whereas the third to the "alkaline lamprophyres". While the calc-alkaline variety is commonly associated with convergent settings, alkaline lamprophyres are typical of divergent margins and continental intra-plate settings (Rock, 1991; Batki *et al.*, 2014; Stoppa *et al.*, 2014; Ubide *et al.*, 2014; Lu

et al., 2015; Pandey *et al.*, 2017*a*; 2017*b*), their composition resembling volatile-enriched alkali basalts, basanites and nephelinites.

Several authors have investigated the main geochemical features of the Cretaceous (110 Ma) to Oligocenic (29 Ma) alkaline lamprophyres across Italy, suggesting their formation by partial melting of a mantle metasomatized by alkaline carbonatitic components (Galassi *et al.*, 1994; Vichi *et al.*, 2005; Stoppa, 2008; Stoppa *et al.*, 2014). Lesser known are the alkaline lamprophyres of the Dolomitic Area (Southern Alps, NE Italy), intruded in and around the Middle Triassic Predazzo Intrusive Complex, to which they seemed geochemically and temporally related (Lucchini *et al.*, 1969). This complex is one of the few plutonic expressions of the high-K calc-alkaline to shoshonitic magmatism that shaped the Dolomitic Area between 237 and 238 Ma (Gasparotto & Simboli, 1991; Bonadiman *et al.*, 1994; Mundil *et al.*, 1996; Abbas *et al.*, 2018; Casetta *et al.*, 2018*a*; 2018*b*; Storck *et al.*, 2018; Wotzlaw *et al.*, 2018). Recent petrologic and Sr-Nd isotopic studies on the Predazzo pluton, complemented by field observations, revealed: i) the existence of three different SiO_2-oversaturated to -undersaturated magma batches and their precise emplacement sequence at shallow crustal depth (1.4-5.6 km); ii) the gradual transition between the intrusion and the overlying hypabyssal and volcanic (basaltic/latitic) deposits; iii) the EM I-like Sr-Nd isotopic signature of the intrusive rocks and the low degree of crustal assimilation experienced by Ladinian magmas during ascent; and iv) the slight isotopic depletion of the mantle source moving towards higher $^{143}Nd/^{144}Nd$ ratios from the older SiO_2-saturated to the younger SiO_2-undersaturated batches (Casetta *et al.*, 2018*a*; 2018*b*).

The connection between the alkaline lamprophyres and the host volcano-plutonic complex has never been investigated, despite being a key factor in deciphering the evolution of the magmatism of the Dolomitic Area. For this reason, whole-rock major, trace element and Sr-Nd isotopic determinations, together with mineral phases major and trace element chemistry, were used to characterize the Predazzo alkaline lamprophyres mantle source, and identify how the

melts differentiated at shallow depths. Finally, $^{40}Ar/^{39}Ar$ dating constrained their emplacement within the temporal evolution of the Dolomitic Area and the whole Southern Alps magmatism.

GEOLOGICAL AND GEODYNAMIC OVERVIEW

The geodynamic framework of the Austroalpine and Southalpine domains during Middle-Late Triassic is complicated by the short timescales, variety of magma types, and overprinting by Alpine orogenesis. Magmas with calc-alkaline to shoshonitic affinity intruded in several localities of the Southern Alps, Dynarides and Hellenides between ~242 and 227±6 Ma (Barbieri et al., 1982; Pamić, 1984; Gianolla, 1992; Mundil *et al.*, 1996; Pe-Piper, 1998; Armienti *et al.*, 2003; Beccaluva *et al.*, 2005; Cassinis *et al.*, 2008; Bellieni *et al.*, 2010; Beltràn-Trivino *et al.*, 2016; Bianchini *et al.*, 2018; Storck *et al.*, 2018; Wotzlaw *et al.*, 2018). Simultaneously, scattered intrusions of alkaline magmas emplaced between 231±1 and 227±7 Ma along the Periadriatic lineament (Karawanken) and in the Carpathians (Ditrau) area (Lippolt & Pidgeon, 1974; Dallmeyer *et al.*, 1997; Morogan *et al.*, 2000; Visonà & Zanferrari, 2000; Batki *et al.*, 2014; Pál-Molnár *et al.*, 2015).

The close relationship between the orogenic magmatism and the onset of extensional-transtensional tectonics (Doglioni, 1984, 1987, 2007; Stampfli & Borel, 2002; 2004) led some to hypothesize various possible geodynamic scenarios for the Southern Alps. They include: i) aborted rifting in a passive margin (Bernoulli & Lemoine, 1980); ii) active mantle upwelling (Stähle *et al.*, 2001); iii) arc system at the Paleo-Tethys NW limb (Castellarin *et al.*, 1988); iv) back-arc development connected to the subduction of the Paleo-Tethys (Ziegler & Stampfli, 2001; Stampfli & Borel, 2002; 2004; Stampfli *et al.*, 2002; Armienti *et al.*, 2003; Stampfli, 2005; Cassinis *et al.*, 2008; Schmid *et al.*, 2008; Zanetti *et al.*, 2013); v) anorogenic rifting with subduction signature inherited from the Hercynian orogeny (Sloman, 1989; Bonadiman *et al.*, 1994; Pe-Piper, 1998; Beltràn-Trivino *et al.*, 2016). Other authors, trying to encompass the Austroalpine and Carnian-Dinaric domains in the geodynamic reconstruction, hypothesized: vi)

the presence, beneath the Southern Alps-Austroalpine and Carnian-Dinaric plates, of different mantle sources affected by Palaeozoic subduction-related and plume-related processes, respectively (Visonà & Zanferrari, 2000); and vii) the existence of a Palaeozoic oceanic basin between Austroalpine and Southern Alps, closed by a subduction dipping beneath the latter (Bianchini *et al.*, 2018).

MATERIALS AND METHODS

Whole-rock major and trace element analyses were carried out at the Department of Physics and Earth Sciences of the University of Ferrara using an ARL Advant-XP automated X-ray fluorescence spectrometer. Full matrix correction procedure and intensities were completed following Traill & Lachance (1966). Accuracy and precision are better than 2-5% for major elements and 5-10% for trace elements. Detection limits are 0.01 wt% and 1-3 ppm for most of the major and trace element concentrations, respectively.

Rb, Sr, Y, Zr, Nb, Hf, Ta, Th, U, and rare-earth elements (REE) were analyzed at the Department of Physics and Earth Sciences of the University of Ferrara by inductively coupled plasma-mass spectrometry (ICP-MS) using a Thermo Series X spectrometer. Precision and accuracy were better than 10% for all elements, well above the detection limit.

Mineral phase major element compositions were analyzed at the Department of Lithospheric Research of the University of Wien, using a CAMECA SX100 electron microprobe equipped with four WD and one ED spectrometers. The operating conditions were as follows: 15 kV accelerating voltage, 20 nA beam current, and 20 s counting time on peak position. Natural and synthetic standards were used for calibration, and PAP corrections were applied to the intensity data (Pouchou & Pichoir, 1991).

Trace element concentration of pyroxene and amphibole crystals was carried out at the CNR - Istituto di Georisorse of Pavia by laser ablation microprobe-inductively coupled plasma-mass spectrometry (LAM-ICP-MS). The basic set and protocol were described by Tiepolo *et al.*

(2003). NIST 610 and NIST 612 standard glasses were used to calibrate relative element sensitivity. Precision and accuracy for trace element analyses were assessed by standard sample BCR-2 (reference values from USGS Geochemical Reference Materials Database). Each analysis was corrected with internal standards using CaO for both clinopyroxene and amphibole. The detection limit was function of the ablation volume and counting time and was therefore calculated for each analysis; indeed, ablation volume greatly depends on instrument configuration. As a consequence, the detection limit reduces if spot size, beam power and cell gas flow are decreased. A 40-100 μm beam diameter and 20 μm s1 scanning rate were used. The theoretical detection limit ranges from 10 to 20 ppb for REE, Ba, Th, U, Zr and are about 2 ppm for Ti.

Whole-rock $^{87}Sr/^{86}Sr$ and $^{143}Nd/^{144}Nd$ analyses were made at the Scottish Universities Environmental Research Centre (SUERC) by thermal ionization mass spectrometry (TIMS) following procedures described by Casetta *et al.* (2018*a*). Eight measurements of SRM-987 and 12 of JNdi-1 made during the course of this analytical programme yielded mean values of 0.710244±0.000016, and 0.512079±0.000018 (2 SD), consistent with the consensus values of ~0.71025 and ~0.51210.

$^{40}Ar/^{39}Ar$ analyses on amphibole and plagioclase separates were made at SUERC. Samples for $^{40}Ar/^{39}Ar$ dating were prepared using the methods described in Mark *et al.* (2011*a*). All samples were subsequently cleaned in de-ionised water. They were parcelled in high purity Al discs for irradiation. International standards Fish Canyon sanidine (FCs) (28.294 ± 0.036 Ma, Renne *et al.*, 2011; Morgan *et al.*, 2014) and GA1550 biotite (99.738 ± 0.104 Ma, Renne *et al.*, 2011) were loaded adjacent to the samples to permit accurate characterisation of the neutron flux (J parameter). Samples were irradiated for 50 hours in the Cd-lined facility of the CLICIT Facility at the OSU TRIGA reactor. Standards were analyzed on a MAP 215-50 system (described below briefly and in more detail by Ellis *et al.*, 2012) - FCs was analyzed by CO_2 laser total fusion as single crystals (n = 20). GA1550 (n = 20) was also analyzed by CO_2 laser total fusion

and step-heated using a CO_2 scanning laser (n = 5) (Barfod *et al.*, 2014). Using GA1550 the J-parameter was determined to a precision approaching 0.1% uncertainty.

Wafers were loaded into an Ultra-High-Vacuum (UHV) laser cell with a SiO_2 window. In situ UVLAMP Ar extraction was conducted using a New Wave UP-213 nm UV laser system (described in Moore *et al.*, 2011). 50 × 50 × 5 μm^3 (amounts of ablated material approximately 1250 μm^3) raster pits were made in mineral surfaces to extract the Ar isotopes. All gas fractions were subjected to 180 seconds of purification by exposure to two SAES GP50 getters (one maintained at room temperature, the other held at ca. 450˚C). A cold finger was maintained at -95.5˚C using a mixture of dry ice ($CO_{2[S]}$) and acetone. Ion beam intensities (i.e., Ar isotope intensities and hence ratios) were measured using a MAP 215-50 mass spectrometer in peak jumping mode. Measurements were made using a Balzers SEV-217 electron multiplier. The system had a measured sensitivity of 1.12×10^{-13} moles/Volt. The extraction and cleanup, as well as mass spectrometer inlet and measurement protocols and data acquisition were automated. Blanks (full extraction line and mass spectrometer) were made following every two analyses of unknowns. The average blank ± standard deviation (n = 28) from the entire blank run sequence was used to correct raw isotope measurements from unknowns. Mass discrimination was monitored by analysis of air pipette aliquots after every five analyses of unknowns (n = 13, 7.21 x 10^{-14} moles ^{40}Ar, $^{40}Ar/^{36}Ar$ = 289.67 ± 0.63).

The samples were step-heated using a CO_2 laser (approximately 500-1500˚C, optical pyrometer measurements). Extracted gases were subjected to 300 seconds of purification by exposure to two SAES GP50 getters (one maintained at room temperature, the other held at ca. 450˚C). A cold finger was maintained at -95.5˚C using a mixture of dry ice ($CO_{2[S]}$) and acetone. Ion beam intensities were measured using a MAP 215-50 mass spectrometer in peak jumping mode. Measurements were made using a Balzers SEV-217 electron multiplier. The system had a measured sensitivity of 1.12×10^{-13} moles/Volt. The extraction and cleanup, as well as mass spectrometer inlet and measurement protocols and data acquisition were automated. Blanks

(full extraction line and mass spectrometer) were made following every analysis of an unknown. The average blank ± standard deviation for each experiment (n = 14) from the entire blank run sequence was used to correct raw isotope measurements from unknowns. Mass discrimination was monitored by analysis of air pipette aliquots after every three analyses.

All Ar isotope data were corrected for backgrounds, mass discrimination, and reactor-produced nuclides and processed using standard data reduction protocols and reported according to the criteria of Renne *et al.* (2009). The atmospheric argon isotope ratios of Lee *et al.* (2006), which have been independently verified by Mark *et al.* (2011*b*), were employed. The $^{40}Ar/^{39}Ar$ ages for were determined relative to the statistical optimization model of Renne *et al.* (2010; 2011) and are reported including analytical and full systematic uncertainties at the 2 sigma level. All raw Ar/Ar data with associated parameters are presented in Electronic Appendix 1.

PETROGRAPHY AND WHOLE-ROCK GEOCHEMISTRY

Petrography

The lamprophyres are part of a swarm of dykes that intrudes the Predazzo Intrusive Complex, the overlying volcanites and the Permo-Triassic sedimentary host rocks (Fig. 1). The dykes are mainly porphyritic basalts to trachytes, the great majority of them having the same high-K calc-alkaline to shoshonitic affinity of the intrusive rocks (Casetta *et al.*, 2018*a*; 2018*b*). Lamprophyres are 20-200 cm in thickness, NNW-SSW to N-S oriented and can be easily distinguished by their greenish colour, strongly contrasting with the pink granitic/syenogranitic body that they preferentially intrude (Fig. 1; see also Lucchini *et al.*, 1969). Contacts are generally sharp, and no significant thermometamorphic structures are present, although intense alteration often obscures hand-sample scale textures.

A distinctive feature is the common presence of carbonate-bearing ocelli, feldspar and amphibole megacrysts (up to 5 cm), and xenoliths (Fig. 1; Vardabasso, 1929; Lucchini *et al.*, 1969; 1982). The latters are mainly cumulate clinopyroxenites (Morten, 1980) or fragments of

the Triassic intrusive rocks and the Permian basement, but also a few spinel lherzolites can be found (Carraro & Visonà, 2003). The petrology and geochemistry of lamprophyres led Lucchini *et al.* (1969) to classify them as camptonites, an alkaline variety of lamprophyres characterized by abundant plagioclase (modally more abundant than K-feldspar), and the absence of leucite and Na-foids (Rock, 1991).

The dykes are panidiomorphic, with, in order of decreasing abundance, amphibole, plagioclase, clinopyroxene and olivine phenocrysts, embedded in a microcrystalline assemblage of amphibole, plagioclase, clinopyroxene, K-feldspar and Fe-Ti oxides (Fig. 2). Accessory phases include carbonate, ilmenite, titanite, apatite and analcime. The modal abundances are: amphibole 35-55 vol.%, plagioclase 30-40 vol.%, clinopyroxene 0-10 vol.%, olivine 0-10 vol.%, K-feldspar 2-6 vol.%, Fe-Ti oxides 3-6 vol.%. Clinopyroxene and olivine are only absent in MA1 sample (Fig. 2b), where the presence of plagioclase, K-feldspar and Fe-Ti oxides strongly increases. Carbonate is present as pseudomorphic phase replacing olivine, in secondary veins/fractures, or as a major constituent of small (200-250 μm in diameter) spherical ocelli, variably distributed and surrounded by the orthogonal growth of multiple small plagioclase, amphibole and/or clinopyroxene crystals (see the following section for a more detailed descripton). These features confirm the definition of camptonites proposed by the previous authors for all Predazzo lamprophyres.

Amphibole, pale brown to reddish in colour, occurs as euhedral, elongate crystals as both phenocrysts and in the groundmass. In sample MA1, amphibole is often acicular and has a pale brown to yellowish colour (Fig. 2b). It ranges in size from 20-30 μm (groundmass) to 2.5 mm (phenocryst), excluding megacrysts, whose colour ranges from dark brown to black.

Plagioclase crystals are generally euhedral and vary in size between 10-20 and 400-450 μm. Larger plagioclase xenocrysts, fragments and xenoliths (0.5-1 mm) of crustal origin can be easily distinguished from the phenocrysts by their rounded shape and by the presence of well developed reaction rims made of Fe-Ti oxides, secondary feldspar and rare clinopyroxene.

Clinopyroxene, pale brown in colour, is less abundant and smaller than amphibole, rarely exceeding 150-200 μm in size among the phenocrysts. Relicts of bigger euhedral crystals (1-2 mm) are almost totally replaced by plagioclase, amphibole and Fe-Ti oxides, resulting in an "atoll-like" shape, where only the outermost rim of clinopyroxene is preserved. The formation of secondary epidote and chlorite often occurs at the expense of clinopyroxene.

Olivine phenocrysts (100-350 μm) are rare and usually pseudomorphosed by calcite and serpentine. This kind of alteration, typical in lamprophyres, is indicated by the general term pilite (Velde, 1968; Rock, 1991). K-feldspar and Fe-Ti oxides are present only in the groundmass, rarely exceeding 40-50 μm in size.

Whole-rock major and trace element chemistry

Predazzo camptonites generally have a SiO_2 range of 44.1 to 47.9 wt%, 1.6-3.2 Na_2O wt% and 1.0-3.7 K_2O wt%; sample MA1 is an exception, and has higher silica (52.8 wt%) and alkali contents (2.9 Na_2O wt%; 5.0 K_2O wt%; Table 1). Mg# is variable, varying between 37 and 70, and mainly controlled by a wide range in MgO. Again, sample MA1 has the lowest FeO content, and is probably more differentiated than the rest of the samples. All lamprophyres have a K-affinity (Fig. 3), and their CaO contents are variable depending upon alteration and presence of carbonates. In the Al_2O_3-MgO-CaO and $SiO_2/10$-CaO-$TiO_2\times4$ ternary diagrams, all samples plot in the alkaline lamprophyres field (Rock, 1987; 1991), and are enriched in Al_2O_3 with respect to the Cretaceous to Oligocene Italian lamprophyres (Stoppa *et al.*, 2014, and references therein). CIPW norm calculations highlight the moderate to strong Si-undersaturation, with 1-13% normative nepheline for all samples and 3-5% normative leucite for two samples with high K/Si. MgO is negatively correlated with compatible elements, such as Ni (237-27 ppm) and Cr (585-14 ppm; Fig. 3).

Whole-rock chondrite-normalized incompatible element patterns (Fig. 4) have positive anomalies in Nb, Ta, Zr, Ti and LILE (especially Sr), and negative anomalies in Th and U.

These features are similar to the Central Iberia lamprophyres (Scarrow *et al.*, 2011). Predazzo lamprophyre patterns resemble those of alkaline rocks, but, when compared to the average composition of oceanic island basalts, they are depleted in all elements except Rb, Ba and Sr. This feature is even more evident when compared to the worldwide camptonites (Fig. 4; Rock, 1991). Chondrite-normalized REE patterns are characterised by LREE enrichment and flat M-HREE profiles, with absence of Eu negative anomaly, consistent with the lack of significant plagioclase fractionation (Fig. 4). The less differentiated camptonite (Mg# 70) is slightly LREE-depleted with respect to the other samples. The Gd_N/Yb_N ratios of Predazzo camptonites range between 1.7 and 2.7, contrasting with the typical steep-sloping shape of OIB rocks in general, and of camptonites in particular (Fig. 4; Sun & McDonough, 1989; Rock, 1991). Compared to the other Italian lamprophyres (Galassi *et al.*, 1994; Vichi *et al.*, 2005; Stoppa, 2008; Stoppa *et al.*, 2014), Predazzo camptonites are generally depleted in all incompatible elements, except for Rb and K. A common feature is the absence of a Ta-Nb-Ti negative anomaly (Fig. 4). The HFSE distribution in the less differentiated Predazzo camptonites fall in the OIB field on a Th_N vs. Nb_N tectonic discrimination diagram (Fig. 5a; Saccani, 2015), suggesting a within-plate setting. The alkaline nature of Predazzo lamprophyres is clearly evidenced by the Ti/Y vs. Nb/Y and Zr/Y vs. Zr diagrams (Fig. 5b-c; Pearce & Norry, 1979; Pearce, 1982), as well as by the Th-Hf-Ta and Zr-Nb-Y ternary diagrams (Fig. 5e-f; Wood, 1980; Meschede, 1986).

MINERAL CHEMISTRY AND TEXTURAL RELATIONSHIPS

Major element composition of amphibole, clinopyroxene, feldspars, oxides and trace element analyses of amphibole and clinopyroxene were determined on representative lamprophyre samples. The intense state of alteration of olivine in pilite prevented its chemical analysis: according to Carraro & Visonà (2003), olivine phenocrysts in the less evolved Predazzo camptonites range in composition from $Fo_{72.5}$ to $Fo_{87.5}$, suggesting a primitive, mantle-derived nature of these rocks.

Amphibole

We adopted the Locock (2014) a.p.f.u. amphibole classification, consistent with the recommendations of the IMA-CNMNC subcommittee on amphiboles (Table 2; Hawthorne *et al.*, 2012; Oberti *et al.*, 2012). This cation site distribution assigns the proper nomenclature while minimizing the OH and Fe^{3+} effects. Amphibole in Predazzo camptonites belongs to both the ^{W}(OH, F, Cl)- and the ^{W}(O)-dominant (oxo-amphibole) groups, and to the Ca subgroup. Its composition, extremely variable between the less and the more differentiated samples, varies from pargasite to ferri-kaersutite, Ti-rich magnesio-hastingsite and Ti-rich ferro-ferri-sadanagaite (Mg# from 28 to 75; Table 2). The sadanagaitic composition is quite rare and represents the most Si-poor variety of amphibole reported from lamprophyres (Rock, 1991). In terms of CaO/Na_2O and Al_2O_3/TiO_2 ratios, most of the analyzed amphiboles are similar to those reported by Rock (1991) from alkaline lamprophyres (Fig. 6). Some crystals have a quite high Al_2O_3/TiO_2 ratio, similar to that of calc-alkaline hastingsites, but maintaining a CaO/Na_2O ratio comparable to alkaline kaersutites (Fig. 6).

Amphibole textural features and major element composition

Optical and electron microscope observations, coupled with major element chemical data, enabled us to identify the occurrence of five distinct textural types of amphibole, following a scheme analogous to that proposed for plagioclase and clinopyroxene crystals at Mt. Etna by Giacomoni *et al.* (2014; 2016).

Type 1 amphiboles (Fig. 7a) are the most common and occur both phenocrysts and in the groundmass. They have euhedral contour with homogeneous pale brown to orange rounded dissolved cores; the more differentiated is the host rock, the more elongated is the crystal shape, becoming acicular in sample MA1. *Type 1* crystals are pargasitic to Ti-rich magnesio-hastingsitic (Mg# = 71-74), usually surrounded by a reddish ferri-kaersutitic rim (Mg# =59-66)

with euhedral shape, in optical continuity with the cores. In *Type 1* crystals an intermediate magnesio-hastingsitic (Mg# = 72-74) overgrowth is often visible by means of electron microscope. Groundmass amphiboles reflect the composition of the outermost rims of the phenocrysts (ferri-kaersutite to Ti-rich magnesio-hastingsite). *Type 2* crystals (Fig. 7b), Ti-rich magnesio-hastingsitic in composition, have brown rounded cores (Mg# = 62-64), characterized by the presence of dispersed Fe-Ti oxides and melt pockets, and ferri-kaersutitic rims (Mg# = 60-68). The cores are often surrounded by magnesio-hastingsitic intermediate overgrowths analogous to those documented in *Type 1* amphiboles. Both the intermediate overgrowth and the external rim are in optical continuity with the core. *Type 3* crystals (Fig. 7c) have blackish dusty cores with euhedral edges. As in case of *Type 1* crystals, they are surrounded by Ti-rich magnesio-hastingsitic to ferri-kaersutitic rims (Mg# 53-70). *Type 4* amphiboles (Fig. 7d) are those previously defined xenocrysts. They usually are cm in size, black coloured and markedly altered, sometimes being resorbed in entire portions. Their Ti-rich magnesio-hastingsitic core (Mg# 51-62) is often pervaded by the incipient formation of fibrous minerals and micrometric veins bearing Fe-Ti oxides. The outer portions of the core present strongly dusty resorbed zones comparable to those recognized in *Type 3* crystals cores. *Type 4* xenocrysts are surrounded by a pale brown to reddish magnesio-hastingsitic to ferri-kaersutitic rim (Mg# ~68). *Type 5* amphiboles (Fig. 7e), documented only in sample MA1, occur both as phenocrysts and centimeter-scale megacrysts. They have dark brown Ti-rich ferri-sadanagaitic to Ti-rich ferro-ferri-sadanagaitic cores (Mg# = 29-39) and pale brown Ti-rich magnesio-hastingsitic rims (Mg# 68-72), grown in optical continuity. With respect to *Type 4* xenocrysts, megacrysts are identified by their euhedral habitus and the absence of resorption/alteration features. It should be noticed that, although important indicators of the physico-chemical conditions of the magmatic system, *Type 2* to *Type 5* are much rarer than *Type 1* amphiboles, rarely exceeding 1-5 vol.% of the specimens.

Amphibole trace element composition

Due to the small size and general alteration of most of the amphiboles, in situ trace element analyses were performed only on *Type 1* (both core/rim of the larger phenocrysts and smaller groundmass specimens), *Type 2* (rim) crystals and *Type 4* (core/rim) xenocrysts (Table 3). Chondrite-normalized incompatible element patterns have Ba, Sr positive spikes and Th, U and Zr negative anomalies; REE patterns are convex-upward (Fig. 8). *Type 4* amphibole core and *Type 1* groundmass crystals have the most Nb-, Zr-, Hf-, and REE-enriched composition, whereas *Type 1* phenocrysts have the less enriched patterns, relatively Zr-Hf-Nb-depleted at the core and REE-depleted at the rim. In all amphiboles, rims are generally REE-depleted with respect to the related cores (Fig. 8).

Clinopyroxene

Clinopyroxene is generally aluminian- to ferrian-titanian-diopside (Fig. 6; Table 4). Large clinopyroxene phenocrysts are typically zoned in Mg#, ranging from ~82 in the centres to 68-72 in the rims. Smaller phenocrysts have Mg# down to 64, being similar in composition to the outermost rim of the larger "atoll-like" clinopyroxene crystals. TiO_2 content reaches high values (5.2 wt%), as already highlighted by Carraro & Visonà (2003).

Clinopyroxene trace element analyses were performed on euhedral phenocrysts as well as on the outermost rims of the larger crystal with evident compositional zoning (Table 3; Fig.8) No significant trace element compositional variations are present between the smaller phenocrysts and the rims of the larger crystals.

Feldspar

From textural relationships, plagioclase and K-feldspar crystallization occurs later than olivine, clinopyroxene and amphibole. Plagioclase compositions vary from An_{74} to An_{23} (Fig. 6; Table

5). K-Feldspar, usually present as groundmass phase, becames modally and dimensionally significant in sample MA1, where it ranges in composition from Or_{54} to Or_{57} (Fig. 6; Table 5).

Fe-Ti oxides

Fe-Ti oxides are widespread in the groundmass assemblage of all camptonites and generally have TiO_2 and Al_2O_3 contents ranging from 12.1 to 19.0 wt% and from 2.3 to 7.8 wt%, respectively (Fig. 6; Table 6). Micrometer-sized Ti-magnetite crystals can be also found included in *Type 2* amphibole cores or within the reaction assemblages pervading some clinopyroxene crystals and *Type 4* amphibole xenocrysts.

CARBONATE OCELLI

Rounded ocellar structures with carbonatic composition were identified in all Predazzo camptonites. Unfortunately, the remarkable alteration of the dykes prevented any accurate evaluation of their distribution at the macro-scale. Sample MA1 is the only ocelli-free, consistently with its more differentiated character (Rock, 1991). The ocelli-hosted carbonate can be subdivided in two groups (Fig. 9; Table 7): i) dolomite-ankerite type (FeO = 5.0-14.4 wt%; MgO = 12.7-18.7 wt%); and ii) magnesite-siderite type (FeO = 27.5-39.0 wt%; MgO = 14.3-24.0 wt%). These compositions are similar to those identified by Rock (1991) for the worldwide carbonate-bearing lamprophyres (Fig. 9). SrO content is low in all carbonate types, reaching the maximum values of 0.16-0.30 wt% in some dolomite-ankerite grains; BaO was often below the EMPA detection limit. MnO content varies from 0.24 to 0.62 wt%. Some of the ocelli are texturally composite, including both smaller dolomite-ankerite crystals and larger well-developed magnesite-siderite ones, the latters mainly occurring in the inner portions; some others are instead constituted of sole dolomite-ankerite crystals (Fig. 9).

An intriguing topic in the study of carbonates in magmatic rocks is the determination of their primary (carbonatitic) or secondary (hydrothermal) origin. If the carbonate ocelli are derived

from a melt, the relationship between lamprophyric and carbonatitic melts would be strengthened by Predazzo camptonites, and liquid immiscibility processes probably drove the generation of the carbonate ocelli globular structures (Rock, 1991; Le Roex & Lanyon, 1998; Leat *et al.*, 2000; Vichi *et al.*, 2005). If not, their nature would be linked to the occurrence of late-stage hydrothermal processes. From a textural point of view, carbonate ocelli in Predazzo camptonites are characterized by: i) spherical shape, easily distinguishable from secondary-filled amygdalae, elongated in shape; ii) flow-aligned tangential growth of high-temperature-forming silicates (plagioclase, amphibole and/or clinopyroxene); and iii) lack of more typically hydrothermal minerals, such as zeolites (Fig. 9). According to Vichi *et al.* (2005) and Gozzi *et al.* (2014), all these features support the primary magmatic nature of the ocelli, and, therefore, the existence of carbonatitic-like droplets within the silicate melt.

To discriminate between primary and secondary carbonates, some authors have suggested that low SrO (<0.6 wt%) is consistent with a late-stage origin (Hay & O'Neil, 1983; Hogarth, 1989; Leat *et al.*, 2000), whereas some others suggested that carbonates with SrO >0.3 wt% and MnO >0.2 wt% can be considered primary (Vichi *et al.*, 2005). Alternatively, the magnesite-siderite carbonates in carbonatitic complexes often have low SrO contents (Buckley & Woolley, 1990; Zaitsev *et al.*, 2004). When plotting our data in a CaO/MgO vs. SrO + MnO space, which discriminates between high temperature and late-stage secondary carbonates (Vichi *et al.*, 2005), a positive correlation is displayed by most of the magnesite-siderite crystals, whereas an almost constant CaO/MgO accompanies a large scattered (SrO + MnO) sum for the dolomite-ankerite grains (Fig. 9). Such a feature is consistent with a late-stage crystallization of the magnesite-siderite crystals, and a magmatic origin for the dolomite-ankerite grains. This hypothesis is also supported by the occurrence of magnesite-siderite-free ocelli in the analyzed camptonites. A similar combination has been also recognized by Leat *et al.* (2000) in carbonate ocelli inside the Middle Jurassic lamprophyres of the Ferrar region (Antarctica): according to these authors, an earlier formation of magmatic calcite-dolomite was followed by a late-stage

deposition of Fe-rich, Sr-poor carbonates towards the core of the ocelli. Such an interpretation, well fitting both the chemical and textural features of the carbonate ocelli of Predazzo lamprophyres, lead us to hypothesize that magnesite-siderite precipitation probably occurred during late-stage hydrothermal fluid circulation, whereas dolomite-ankerite crystallization was primary (magmatic), likely derived from a carbonatitic-like melt that coexisted with the lamprophyric one. It is not clear whether these carbonatites are primary melts generated by mantle partial melting or formed by exsolution of immiscible carbonate fractions from alkaline magmas (Wallace & Green, 1988). The almost perfectly rounded shape of the analyzed ocelli seems to favour immiscibility, however further studies are required to investigate the association between carbonatites and lamprophyres in the Southern Alps subcontinental lithospheric mantle.

AGE AND ISOTOPIC SIGNATURE OF PREDAZZO CAMPTONITES

$^{40}Ar/^{39}Ar$ geochronology

The $^{40}Ar/^{39}Ar$ incremental heating method was applied to amphibole and plagioclase separates from two different camptonite samples (FF2 and FF37). Results and age spectra are shown in Fig. 10. Sample FF2 (plagioclase): The data defined a plateau (>90% ^{39}Ar, n = 16, MSWD 0.9) with an age of 218.90 ± 0.59 Ma. The younger discordant steps in the age spectrum likely related to alteration of the plagioclase. Sample FF37 (amphibole): The data defined a plateau (>50% ^{39}Ar, n = 6, MSWD 1.98) with an age of 219.70 ± 0.73 Ma. Younger apparent ages in the early steps of amphibole age spectrum, concomitant with high K/Ca ratios, were probably due to secondary alteration. The plagioclase and amphibole age are in good agreement and define a crystallisation age for the Predazzo camptonites of 219.22 ± 0.46/0.73 Ma (2σ; analytical/full systematic uncertainties).

$^{87}Sr/^{86}Sr$ and $^{143}Nd/^{144}Nd$ isotopes

Whole-rock $^{87}Sr/^{86}Sr$ and $^{143}Nd/^{144}Nd$ isotopic ratios were measured on representative samples among the Predazzo lamprophyres (Table 1). Initial isotopic ratios, respectively named $^{87}Sr/^{86}Sr_i$ and $^{143}Nd/^{144}Nd_i$, were corrected to an age of 220 Ma, in accordance with the $^{40}Ar/^{39}Ar$ dating results. Lamprophyres have $^{87}Sr/^{86}Sr_i$ values ranging between 0.7033 and 0.7040, for a $^{143}Nd/^{144}Nd_i$ range of 0.51260-0.51265 (Fig. 11). The isotopic data, in accordance to what hypothesized by Marrocchino *et al.* (2002), highlight a discrepancy between the isotopic signature of the lamprophyres and their "hosting" Predazzo Intrusive Complex (Casetta *et al.*, 2018*a*). The lamprophyres isotopic signature lies in fact between the DMM and the EM I mantle end-members, in contrast to that of the Predazzo intrusive rocks, purely EM I-like (Fig. 11).

LAMPROPHYRE DIFFERENTIATION

The differentiation processes of worldwide alkaline lamprophyres are often characterized by the occurrence, both at local (ocelli, veins, globules) and regional scale (coeval dykes/plutons), of co-magmatic intermediate/felsic rocks, mainly foid-syenitic in composition (Rock, 1987; 1991). In these samples, the Ni, Cr decrease at decreasing MgO (Fig. 3), together with the mineral phase compositional variations, are consistent with fractional crystallization. The absence of a significant interaction with crustal components during ascent/emplacement is supported by the high whole-rock MgO, Cr and Ni contents, the presence of forsteritic olivine and the initial $^{87}Sr/^{86}Sr$ and $^{143}Nd/^{144}Nd$ values that approach the DMM isotopic component. These features point towards a mantle-derived origin for our samples, in accordance with most of the worldwide alkaline lamprophyres (Rock, 1991).

The extent of fractional crystallization was estimated assuming Rayleigh distillation (e.g. Shaw, 1970). Assuming Zr as perfectly incompatible element (e.g. a mineral-melt distribution coefficient of zero), the most differentiated camptonite MA1 was generated by ~40% fractional crystallization of a starting primitive camptonitic melt. This estimate is consistent with mass balance calculations from major elements. Major element vectors (Fig. 12) show that ~35%

fractional crystallization of an assemblage made of olivine (19.1%), clinopyroxene (53.4%), amphibole (19.1%) and Ti-magnetite (8.4%) from a starting primitive camptonitic magma can in fact reproduce the MA1 composition.

T-P-fO_2 CONDITIONS OF CRYSTALLIZATION AND WATER CONTENT OF LAMPROPHYRIC MELTS

The determination of T-P-fO_2 parameters and water content of lamprophyric systems is challenging. Following Rock (1987, 1991), we assume that the whole-rock samples approximate the composition of melt + suspended crystals + volatiles. On this basis, the physico-chemical crystallization conditions of Predazzo camptonites were estimated by means of several thermo-, oxy-barometric and hygrometric equations applied to chosen mineral (clinopyroxene, Ti-magnetite, amphibole)-melt pairs. Errors related to each applied method are reported in Table 8.

Equilibrium between clinopyroxene (Cpx) phenocrysts and camptonitic melt was evaluated by means of their Fe-Mg partitioning, assuming a $^{Cpx\text{-}Liq}Kd_{Fe\text{-}Mg}$ of 0.26±0.05 (Akinin *et al.*, 2005), which ideally reflect clinopyroxene equilibrium conditions in an alkali-dominated basic melt (i.e. camptonites; Ubide *et al.*, 2014). Since most of clinopyroxene-liquid thermobarometers require as input the H_2O content of the crystallizing melt, and this parameter is highly variable in the lamprophyre system, *T* and *P* of clinopyroxene crystallization were determined by means of the single-mineral H_2O-independent equations 32a and 32d of Putirka (2008), in turn derived by the *T*-dependent barometer and the *P*-independent thermometer of Putirka *et al.* (1996). This rational scheme enabled us to retrieve the *T-P* path of clinopyroxene crystallization without implying any circular reference. The equilibrium between amphibole (Amp) crystals and the camptonitic melts was evaluated by means of the *T*- and *P*-independent $^{Amp\text{-}Liq}Kd_{Fe\text{-}Mg}$ exchange coefficient, which should be 0.28±0.11 in conditions of equilibrium (Putirka, 2016). The H_2O content of the melt from which amphibole crystallized was calculated by the single-mineral

hygrometer of Ridolfi *et al.* (2010). Afterwards, the *T-P* conditions of amphibole crystallization were calculated by means of the amphibole-melt *P*-independent thermometer (Equation 5) and the *T*-independent, H_2O-dependent barometer (Equation 7b) of Putirka (2016). In this latter equation, the H_2O values obtained by the Ridolfi *et al.* (2010) hygrometer were used as input. The oxygen fugacity of the magmatic system was calculated by means of the oxy-barometer of Ishibashi (2013), based on the Fe^{2+}/Fe^{3+} partitioning between spinel and melt.

Clinopyroxene and Ti-magnetite crystallization conditions

Equilibrium check results indicated that most of the clinopyroxene phenocrysts were not in equilibrium with the high Mg# (59-65) camptonitic melts ($^{Cpx\text{-}Liq}Kd_{Fe\text{-}Mg}$ = 0.32-0.96), requiring instead a more evolved melt to attain equilibrium (Mg# 44-49). The disequilibrium is also supported by the compositional zoning between cores (Mg# 82) and rims (Mg# 68) of many crystals, as well as by the dusty reaction zones of the larger phenocrysts. The few crystals attaining equilibrium belong to slightly more evolved camptonitic samples ($^{Cpx\text{-}Liq}Kd_{Fe\text{-}Mg}$ = 0.17-0.40). Thermobarometric results indicate that clinopyroxene in equilibrium with their host rock composition crystallized at *P* of 490±180 MPa and *T* of 1087±27°C (Table 8). According to these ranges, *T-P* values of 1100-1050°C and 500 MPa were considered to apply the Ishibashi (2013) oxy-barometer to Ti-magnetite crystals. Results yielded a fO_2 interval of -8.3/-10.0 log fO_2 at 1100°C, and a -9.4/-11.0 log fO_2 range at 1050°C (between -1 and +1 FMQ; Table 8).

Amphibole crystallization conditions

Amphibole crystals in the less evolved camptonite resulted not in equilibrium with their host rock composition, having an $^{Amp\text{-}Liq}Kd_{Fe\text{-}Mg}$ of 0.42-0.89. On the other side, equilibrium was attained by some crystals in the more evolved MA1 sample ($^{Amp\text{-}Liq}Kd_{Fe\text{-}Mg}$ = 0.29-1.0). As expected, *Type 4* xenocrysts and *Type 5* amphiboles cores yielded extreme disequilibrium conditions, with $^{Amp\text{-}Liq}Kd_{Fe\text{-}Mg}$ values as high as 1.94.

The Ridolfi *et al.* (2010) hygrometer indicates that *Type 1*, *Type 2* and *Type 3* amphiboles crystallized at water contents of 7.3±0.3 wt% in the less evolved camptonitic melt, and 6.8±0.7 wt% in the more differentiated one (Table 8). Higher values were calculated for *Type 4* xenocrysts and *Type 5* amphibole cores, which yielded H_2O contents up to 9.8 wt%. By considering only the crystals in equilibrium with their host rock composition, a range of 6.4±0.3 H_2O wt% is obtained. Putirka (2016) thermobarometers yielded *T*-*P* intervals of 1074-927°C and 1230-470 MPa for all amphibole crystals (Table 8). The highest *P* were calculated for *Type 4* xenocrysts (1190±50 MPa) and *Type 5* amphiboles cores (1030±50 MPa), at corresponding crystallization *T* of 1037±21°C and 952±21°C, respectively (Table 8). It is worth noting that, due to the significant disequilibrium between *Type 4* and *Type 5* crystals and the melt, these values should be considered with caution. By taking into account only the crystals in equilibrium with the host rock, *T*-*P* ranges of 1027±12°C and 600±60 MPa are obtained. These values can likely represent the shallower amphibole crystallization conditions in the magmatic system. The deeper crystallization conditions can be instead roughly approached by some *Type 1*, *Type 2* and *Type 3* crystals close to the equilibrium with the host camptonite ($^{Amp\text{-}Liq}Kd_{Fe\text{-}Mg}$ = 0.42-0.46), which yield *P* and *T* up to 1160 MPa and 1067°C. In any case, the obtained *T*-*P* ranges are consistent with the experimental simulations proposed by Pilet *et al.* (2010), who demonstrated that kaersutite crystallization can start at 1130°C and 1.5 GPa in volatile-enriched (5-6 H_2O wt%) basanitic melts, thus in conditions similar to those of Predazzo camptonites. If combined to the thermobarometric results obtained by clinopyroxene, these *T*-*P* values suggest that crystallization in the lamprophyric system occurred continuously between 690 and 230 MPa, at *T* decreasing from 1124 to ~1000°C, with an H_2O content ≥ 6.4±0.3 wt%.

Interpretation of amphibole textures

A correlation between the obtained *T*-*P* and H_2O results and the previously identified textures enable us to infer amphibole crystallization processes. The homogeneous composition of *Type*

1 amphibole cores, close to the equilibrium with the less evolved melt ($^{Amp\text{-}Liq}Kd_{Fe\text{-}Mg}$ = 0.42-0.58) records a growth at high *T-P* (1057±12°C; 980±50 MPa), and 7.5±0.3 H_2O wt% in the melt. The crystallization of *Type 1* crystals continued during differentiation of the melt towards more evolved compositions (MA1 sample), where crystals attain equilibrium ($^{Amp\text{-}Liq}Kd_{Fe\text{-}Mg}$ = 0.32-0.36), at *T-P* down to 1013±34°C and 740±120 MPa, and water content of 7.3±0.9 wt%. *Type 2* crystal cores, in marked disequilibrium with the melt ($^{Amp\text{-}Liq}Kd_{Fe\text{-}Mg}$ = 0.73-0.80), record crystallization *T* and *P* of 1004±3°C and 900±10 MPa, at 7.0±0.1 H_2O wt%. The rounded shape of both *Type 1* and *Type 2* cores reflects an event of dissolution after reaction with a melt undersaturated in amphibole. Subsequently, the melt differentiated and re-saturated in amphibole, allowing the precipitation of the rims at lower *T-P* (1048±15°C, 750±110 MPa *Type 1*; 1029±24°C and 750±20 MPa *Type 2*) and H_2O content (6.9±0.3 wt%; Fig. 7). The magnesio-hastingsitic overgrowth in both *Type 1* and *Type 2* crystals, similar to the diopsidic bands identified by Petrone *et al.* (2018) in clinopyroxenes from Stromboli volcano (Aeolian Islands), probably formed in response of new pulse of primitive melts that introduced additional high *T* components (Mg and Ca) in the magmatic system. An abrupt *T* increase (from 1051 to 1071°C) is recorded in this intermediate overgrowth (Figg. 7a and 7b), which can provide the evidence of small-scale mixing dynamics between differentiated and primitive batches inside the magmatic system. Dusty zones of *Type 3* amphibole cores formed as result of pseudomorphic replacement by interface-coupled dissolution-precipitation processes, resulting in Ti-magnetite, plagioclase and clinopyroxene formation at the interface (Ruiz-Agudo *et al.*, 2014). The overgrowth of a newly formed rim in *Type 3* crystals is likely concomitant with the formation of *Type 1* and *Type 2* rims. *Type 3* rim, in fact, approaches the equilibrium towards the more evolved camptonitic melt ($^{Amp\text{-}Liq}Kd_{Fe\text{-}Mg}$ = 0.34-0.69). Its crystallization conditions are the following: *T* = 1017±40°C; *P* = 760±120 MPa; melt H_2O content = 7.2±0.4 wt%. *Type 4* xenocrysts probably represent relicts of larger crystals of deep crustal origin, brought to the surface by the ascent of lamprophyres. The incipient alteration and resorption features of their

cores suggest disequilibrium with the hosting melt, as also confirmed by the high $^{Amp\text{-}Liq}Kd_{Fe\text{-}Mg}$ (1.22). Their dusty portions probably formed as consequence of interface-coupled dissolution-precipitation. The outermost rim, compositionally analogous to most phenocryst rims and groundmass crystals (*Type 1, Type 2* and *Type 3*) represent a late overgrowth approaching the equilibrium with the melt ($^{Amp\text{-}Liq}Kd_{Fe\text{-}Mg}$ down to 0.61), as evidenced by the crystallization *T* (1051±9°C), *P* (1180±50 MPa) and H_2O (8.6±0.3 wt%). The sharp edges and optical continuity between *Type 5* amphiboles core and rim, as well as the absence of resorption zones, suggest that this texture is a consequence of a magnesio-hastingsitic overgrowth around preexisting sadanagaitic (Mg# = 29-39) crystals (Fig. 7e). The high $^{Amp\text{-}Liq}Kd_{Fe\text{-}Mg}$ of the cores (1.18 to 1.94) indicates significant disequilibrium with respect to the host rock composition, implying that they would attain equilibrium only in an extremely differentiated melt. The related thermobarometric results, which should be considered with caution, suggest high *P* (1030±50 MPa) and low *T* (952±21°C) of crystallization, at high water content (up to 9.8 wt%). The peculiar composition of *Type 5* cores, rare even in lamprophyres (Rock, 1991), makes it difficult to clearly define their origin, deserving further studies. *Type 5* rims represent a subsequent growth in equilibrium with the melt ($^{Amp\text{-}Liq}Kd_{Fe\text{-}Mg}$ = 0.29-0.55), at *T* of 1015±18°C, *P* of 570±60 MPa and H_2O content down to 5.8 wt%.

The observed simple dissolution and pseudomorphic replacement textures indicate a very dynamic regime of the lamprophyres magmatic system. Chemical zoning associated with dissolution-reprecipitation textures suggest that amphibole stability was affected by *T* changes due to small scale mixing between variably differentiated and/or volatile-rich melts. The repeated occurrence of such small-scale mixing processes resulted in fact in multiple and abrupt changes of amphibole liquidus conditions during lamprophyre differentiation.

LAMPROPHYRE MANTLE SOURCE AND MELTING MODEL

An intriguing topic is the nature of the mantle source from which Predazzo lamprophyres were generated, especially in the light of their HFSE/REE distribution and Sr-Nd isotopic signature. Indirect evidence of the minimum depth of segregation is provided by the lherzolite xenoliths, which record a re-equilibration process at about 45 km of depth, in the spinel stability field (Carraro & Visonà, 2003). The Zr/Y (6-11), Lu/Hf (0.07-0.12) and Dy_N/Yb_N (1.1-1.7) ratios of Predazzo lamprophyres suggest that garnet played a significant role during melting in their mantle source, as also suggested by Pinzuti *et al.* (2013) for Asal Rift magmas. However, the La_N/Yb_N and Gd_N/Yb_N ratios of the less evolved camptonites are not very high, suggesting that their source differs from those of the "typical" alkaline lamprophyres and OIB magmas (Sun & McDonough, 1989; Rock, 1991). According to the Sr-Nd isotopic data (Fig. 11), lamprophyres were generated by a depleted mantle, as also confirmed by the Nb/La vs. La/Yb diagram of Smith *et al.* (1999), which indicates that an asthenospheric contribution was required for their generation (Fig. 13a).

On the basis of these constraints, we modelled the nature of the mantle domain from which Predazzo lamprophyres were segregated by non-modal batch melting (Shaw, 1970). To account for the HFSE and REE budget of our samples, several mantle melting domains were used as starting point of our simulations. The modal composition and melting proportion of each of the considered mantle sources are reported in Table 9. A first discrimination between the role of spinel and garnet in the hypothetical source was put forward by using as starting mantle domains a spinel- and a garnet-bearing fertile lherzolites with Primordial Mantle (PM; Sun & McDonough, 1989) composition (curves II and III in Fig. 13). Consistently with the Sr-Nd isotopic data, a melting path was also proposed by using as starting source a depleted mantle composition (DMM; Workman & Hart, 2005; curve I in Fig. 13). The obtained melting curves suggest that none of the chosen starting components were able to reproduce the Sm/Yb ratio of Predazzo lamprophyres (Fig. 13). Their Gd/Yb ratio was better approximated by the melting curve of the garnet-bearing source, even if the match was not perfect (curve III in Fig. 13).

Consequently, amphibole and/or phlogopite were introduced as additional components of the starting mantle domains in our simulations. The calculated curves showed that garnet-amphibole- (curve V), garnet-phlogopite- (curve VI) and garnet-spinel-amphibole-bearing (curve IV) sources are able to account for the Sm/Yb and Gd/Yb ratios of our samples (Fig. 13), though the garnet-phlogopite-lherzolite assemblage was not able to reproduce the HREE systematics. Among the melting trends of garnet-amphibole- and the garnet-spinel-amphibole-bearing sources, the former better reproduced the features of the less evolved camptonites, both in the Sm/Yb, La/Yb and Gd/Yb ratios and in the REE pattern (Fig. 13d). Accordingly, we suggest that the Predazzo lamprophyres could have been generated by low melting percentages (1.0 to 2.5%) of a garnet-amphibole-bearing lherzolite, with a fertile PM starting composition (Sun & McDonough, 1989).

Such mantle source modal composition and melting degrees are similar to those proposed by Batki *et al.* (2014) for the generation of Ditrau lamprophyres (1-4% partial melting). However, the mantle source composition required by Predazzo lamprophyres is more depleted than the Ditrau one, being this latter a REE-enriched mantle with significant contribution of asthenospheric HIMU-OIB-like components (EAM, Seghedi *et al.*, 2004; Batki *et al.*, 2014). The presence of a LILE- and volatiles-enriched garnet-bearing mantle source with an asthenospheric signature was also proposed by Stoppa *et al.* (2014) to model the genesis of the Cretaceous to Oligocenic alkaline/ultramafic lamprophyres of Central-Southern Italy, whose REE patterns are strongly LREE-enriched and HREE-depleted with respect to the Predazzo ones. The involvement of amphibole and garnet during melting was required to simulate the relatively low LREE/HREE ratios of Predazzo lamprophyres, as well as to get rid of their H_2O-CO_2-alkali-rich nature. Considering that the spinel-garnet transition in a continental lithospheric setting occurs at 60-90 km (2-3 GPa; Takahashi & Kushiro, 1983; Falloon & Green, 1988; Kinzler & Grove, 1992; Robinson & Wood, 1998; Pinzuti *et al.*, 2013), we can constrain the melting region of Predazzo lamprophyres to >60 km depth. Amphibole stability in the mantle

is limited to ~3 GPa (Frost, 2006; Fumagalli *et al.*, 2009; Tumiati *et al.*, 2013; Mandler & Grove, 2016), suggesting that the mantle source depth is <90 km. Based on these constraints, we suggest that a depth of 70-80 km is most likely for the source region of these camptonites. Similar depths are also consistent with those proposed by Hammouda & Keshav (2015), according to whom carbonatite and silicate melts can coexist between 2 and 2.6 GPa (ca. 60-80 km) along the convecting mantle adiabat (asthenosphere).

GEODYNAMIC IMPLICATIONS

The magmatism of the Dolomitic Area

The late-stage occurrence of alkaline lamprophyric dykes in intrusive complexes often acquires a double significance, since they do not only act as younger chronological boundary of the magmatic episodes, but they also constitute the most primitive (and least contaminated by the crust) magma types (Rock, 1991). In the case of the Predazzo area, several authors suggested a close relationship between the alkaline lamprophyres and the host pluton (Lucchini *et al.*, 1969; 1982; Carraro & Visonà, 2003). The new $^{40}Ar/^{39}Ar$ age results (from 218.90 ± 0.59/0.66 to 219.70 ± 0.73/0.85 Ma; Fig. 10) lead us to point out that the lamprophyric rocks belong to a distinct magmatic pulse that occurred about 17-20 Ma later than the emplacement of the Predazzo Intrusive Complex (U-Pb zircon age of 238.075 ± 0.087 Ma, Storck *et al.*, 2018). Moreover, since the entire Ladinian volcano-plutonic event in the Dolomitic Area has a limited duration (from 239.04±0.04 to 237.77±0.05 Ma; Brack *et al.*, 1996; Mundil *et al.*, 1996; Mietto et al., 2012; Abbas *et al.*, 2018; Storck *et al.*, 2018; Wotzlaw *et al.*, 2018), it is evident that the lamprophyres represent a distinct magmatic event. This chronological gap is also reinforced by the geochemical discrepancies: despite showing a K-affinity comparable to that of the high-K calc-alkaline to shoshonitic volcano-plutonic rocks of the entire Dolomitic Area (Bonadiman *et al.*, 1994; Casetta *et al.*, 2018*a*; 2018*b*), camptonites have peculiar trace element profiles and Sr-Nd isotopic signature (Figg. 4 and 11). In fact, whereas the Ladinian high-K calc-alkaline to

shoshonitic rocks display the typical subduction-related incompatible element patterns, alkaline lamprophyres lack any Ta-Nb-Ti and U-Th negative anomaly, suggesting the involvement of an OIB-like component in their mantle source. The $^{87}Sr/^{86}Sr_i$ and $^{143}Nd/^{144}Nd_i$ signature of Predazzo camptonites points towards a genesis from a mantle source more depleted than the EM I-like source that produced the Ladinian high-K calc-alkaline to shoshonitic rocks. As shown in Fig. 11, in fact, they plot close to the DMM end-member (Workman & Hart, 2005), suggesting that a significant contribution of the asthenospheric mantle was involved in their genesis. This feature confirms a time-related progressive depletion of the mantle source beneath the Dolomitic Area during Middle-Late Triassic, as already hypothesized for the source of Predazzo Intrusive Complex by Casetta *et al.* (2018*a*). Our study indicates that the magmatic activity in the Dolomitic Area was not confined to the Ladinian, but re-activated at about 218.5-220.5 Ma, with the emplacement of a small alkaline pulse generated from a $^{143}Nd/^{144}Nd$-enriched mantle domain. At shallow depth, the ascent of such small melts was probably favoured by extensional-transtensional dynamics, to which lamprophyres are often associated (e.g. Scarrow *et al.*, 2011, and reference therein). The (if any) relationships between Predazzo lamprophyres and the Triassic NE-SW transtensive-transpressive regimes of the Dolomitic Area (Doglioni, 2007; Doglioni & Carminati, 2008; Abbas *et al.*, 2018), however, has never been investigated, and requires further studies, especially in the light of the new age data. The occurrence of extensional dynamics during lamprophyres ascent is also implied by the amphibole and clinopyroxene *T-P* path of crystallization. In contrast to the Ladinian magmatic event, when the crystallization of the high-K calc-alkaline to shoshonitic melts occurred preferentially in batches located at shallow crustal depths (1.4-5.6 km; Casetta *et al.*, 2018*a*), lamprophyres crystallization started at 24 km (considering a $\Delta P/\Delta z$ of 29 MPa/km) and continued towards the surface (at least until 8 km). Such a condition is consistent with the presence of a polybaric vertical plumbing system and suggests that the fractional crystallization and (small-scale) mixing processes recorded by amphibole crystals took place en route to the

surface, without implying the presence of a magma chamber. This hypothesis, fostered by the presence of mantle xenoliths in few Predazzo camptonites, further suggest that lamprophyres are unrelated to the host plutonic complex.

Late-stage magmas or alkaline precursors?

When considered at a geodynamic scale, the significance of Predazzo lamprophyres is intriguing, since several magmatic episodes with variable geochemical affinity shaped the Southalpine-Austroalpine and Carnic-Dinaric domains from Permian to Middle-Late Triassic. The most similar and chronologically closer magmatic occurrence was documented in the Ditrau Alkaline Massif (Carpathians), where late-stage alkaline lamprophyres (camptonites) intruded a Middle-Triassic (231-227 Ma) alkaline intrusion (Dallmeyer *et al.*, 1997; Morogan *et al.*, 2000; Pana *et al.*, 2000; Batki *et al.*, 2014; Pál-Molnár *et al.*, 2015). The major and trace elements and isotopic similarities between the Ditrau lamprophyres and the host pluton led to interpret them as the parental magmas of the intrusive suite (Batki *et al.*, 2014). Such a model cannot be applied to the Predazzo case, where the geochronological and geochemical discrepancies between the alkaline lamprophyres and the plutonic complex rule out any possible correlation between camptonites and the trachybasaltic/shoshonitic rocks. Notwithstanding a slight relative depletion in Th, U, Nb, Zr and LREE with respect to the Ditrau lamprophyres, Predazzo lamprophyres have comparable Sr-Nd isotopic signature (Figg. 4 and 11), suggesting that similar mantle sources were involved in their genesis. According to Batki *et al.* (2014), Ditrau lamprophyres were generated in an early extensional phase of the Middle Triassic to Jurassic rifting that separated the Getic microplate from the Bucovinian margin (Batki *et al.*, 2014), thus representing the Alpine Tethys rift portion located northward of the Meliata basin (Stampfli *et al.*, 2002; Stampfli, 2005). Precursors of the Tethyan opening were also documented in the Brescian Alps, not far from the Dolomitic Area, where intra-plate tholeiitic

lavas and dykes with depleted Sr-Nd isotopic signature emplaced almost simultaneously with the Predazzo lamprophyres, at about 217±3 Ma (Cassinis *et al.*, 2008).

Coeval magmatic occurrences were also recognized in the Western Alps, where alkaline dykes, generated by an upwelling mantle with significant asthenospheric contribution, emplaced in the Finero area between 190-212.5 and 225±13 Ma (Stähle *et al.*, 1990; 2001; Schaltegger *et al.*, 2015). Moreover, ages of 215±35 Ma and 220±4 Ma were determined by Morishita *et al.* (2008) and Malitch *et al.* (2017), respectively, for the formation of the metasomatic apatite-rich and chromitite layers in the Finero peridotite. This temporal overlap, bolstered by the similar Sr-Nd isotopic systematics between the alkaline dykes and the apatite-rich layers (Fig. 11), led several authors (Ferrario & Garuti, 1990; Morishita *et al.*, 2003; 2008; Zaccarini *et al.*, 2004) to associate all these occurrences to a unique alkaline-carbonatitic magmatic event. The generation of such H_2O-CO_2-rich fluids was attributed to mantle upwelling dynamics in a continental rifting setting (Zaccarini *et al.*, 2004). Further evidence of an intimate association between alkaline and carbonatitic magmas in the Western Alps has been recently provided by Galli *et al.* (2019), who documented the existence of alkaline-carbonatitic bodies with emplacement age of 185-195 Ma throughout the Ivrea zone.

The 219.22 ± 0.73 Ma occurrence of alkaline lamprophyres at Predazzo can be easily incorporated in such a context, taking into account that their Sr-Nd isotopic signature totally overlap those of the alkaline dykes and the apatite-rich layers at Finero (Fig. 11; Stähle *et al.*, 1990; 2001; Morishita *et al.*, 2008). The less differentiated alkaline dykes intruded at Finero (Stähle *et al.*, 2001) are also characterized by trace element patterns comparable to those of Predazzo lamprophyres, except for Nb, Ta and Zr, slightly enriched in the formers. A marked U-Th depletion characterizes both Predazzo lamprophyres and the alkaline dykes at Finero, and their REE patterns almost totally overlap. Furthermore, the Sr-Nb enrichment of Predazzo lamprophyres matches the main features of the apatite-bearing assemblages at Finero (Zanetti *et al.*, 1999), confirming the involvement of a carbonate-rich component in their genesis. This

parallelism is also supported by the presence, in Predazzo camptonites, of carbonate ocelli with a dolomite-ankerite composition comparable to that of the interstitial dolomite grains in the Finero peridotite (Zanetti *et al.*, 1999).

According to our findings, Predazzo lamprophyres can be considered as an expression of the 190-225 Ma alkaline-carbonatitic magmatism that intruded the subcontinental mantle portion beneath the Southern Alps (Ferrario & Garuti, 1990; Stähle *et al.*, 1990; 2001; Zanetti *et al.*, 1999; Morishita *et al.*, 2003; 2008; Zaccarini *et al.*, 2004; Matsumoto *et al.*, 2005; Raffone *et al.*, 2006; Schaltegger *et al.*, 2015; Malitch *et al.*, 2017). This magmatic pulse, characterized by a mantle-upwelling signature, is distinguished from the previous, subduction-related, K- and LILE-rich metasomatic episode that produced amphibole and phlogopite in the Finero peridotite (Fig. 11; Coltorti & Siena, 1984; Morishita *et al.*, 2003; 2008; Malitch *et al.*, 2017). According to the U-Pb zircon ages (190-180 Ma and 230-180 Ma) proposed by Zanetti *et al.* (2016) and Langone *et al.* (2018), the alkaline-carbonatitic metasomatism affected the subcontinental mantle immediately prior to its exhumation, which was precisely related to the extensional stages of the Alpine Tethys rift.

Rather than to a late-stage episode connected to the Middle Triassic high-K calc-alkaline to shoshonitic (orogenic) magmatism, the generation of Predazzo lamprophyres should be considered, together with the Ditrau lamprophyres, the Brescian Alps basalts and the Ivrea alkaline-carbonatitic magmas, as a Late Triassic precursor of the Alpine Tethys rifting event. This hypothesis is supported by their depleted Sr-Nd isotopic signature, consistent with a genesis from a mantle source influenced by an asthenospheric contribution (Fig. 11). Further evidence is given by the incompatible elements pattern of the alkaline lamprophyres that, when compared to the Ladinian shoshonitic rocks of the Dolomitic Area, appear depleted in U, Th, K and La, more than enriched in Nb and Ta (Fig. 4). Such a feature is consistent with the progressive shift of the magmatism from orogenic-like to anorogenic, and thus to a progressive

evolution of the subcontinental mantle source towards a more depleted, asthenospheric-related nature.

CONCLUSIVE REMARKS

The petrological, geochronological and isotopic study of the Predazzo alkaline lamprophyres enabled us to provide new insights on the geodynamic evolution of the Dolomitic Area and the Southern Alps during Middle-Late Triassic. The most relevant findings can be summarized as follows:

1. The compositional spectrum of Predazzo alkaline lamprophyres (camptonites) can be explained by assuming 35-40% fractional crystallization of olivine, clinopyroxene, amphibole and Ti-magnetite from an initial primitive camptonitic melt.
2. Amphibole textural and compositional features suggest that the lamprophyre magmatic system was subjected to small scale mixing between variably differentiated and/or volatile rich melts during differentiation. Moreover, the occurrence, composition and textural features of carbonate-bearing ocelli suggest that a carbonatitic melt was intimately associated to the alkaline lamprophyric one.
3. $^{40}Ar/^{39}Ar$ ages of Predazzo alkaline lamprophyres demonstrated that they were emplaced at 219.22 ± 0.73 Ma (Late Triassic; $^{40}Ar/^{39}Ar$; 2σ; full systematic uncertainties), suggesting an origin unrelated to the short-lived Ladinian high-K calc-alkaline to shoshonitic magmatism of the Predazzo-Mt. Monzoni intrusions in the Dolomitic Area.
4. The difference between alkaline lamprophyres and the host Ladinian rocks is illustrated by the absence of Ta-Nb-Ti negative anomalies, the presence of U-Th negative peaks, and their HFSE distribution, which point towards a genesis in an intra-plate geodynamic setting, from a garnet-bearing mantle source. This is also confirmed by their Sr-Nd isotopic systematics, which are consistent with a depleted mantle contribution in their source, in contrast to the

pure EM I-like signature of the Predazzo-Mt.Monzoni Ladinian intrusions, which was ascribed to a subduction-modified mantle.

5. Thermo-, oxy-barometric and hygrometric calculations based on clinopyroxene, amphibole and Ti-magnetite composition suggest that the crystallization in the lamprophyre magmatic system occurred at least between 690 and 230 MPa, a *T* decreasing from 1124 to ~1000°C. The oxygen fugacity of the magmatic system varied between -1 and +1 FMQ, whereas the H_2O content of the lamprophyric melts resulted ≥ 6.4±0.3 wt%, decreasing with decreasing temperature. These results strengthen the distinction between lamprophyres and the Ladinian high-K calc-alkaline to shoshonitic magmatism: whereas the latter was dominated by crystallization processes at shallow crustal levels (1.4-5.6 km; Casetta *et al.*, 2018), lamprophyres started crystallizing at about 24 km and continued towards the surface, probably in an extensional-transtensional tectonic regime.
6. Mantle melting models suggest that low melting percentages (1.0-2.5%) of a fertile garnet-amphibole-bearing lherzolite can account for the generation of Predazzo lamprophyres. The melting region was probably located between 70 and 80 km of depth.
7. Predazzo lamprophyres are temporally, spatially and geochemically correlable to several magmatic occurrences of the Southern Alps-Carpathians area: i) the Ditrau alkaline lamprophyres (Batki *et al.*, 2014); ii) the Brescian Alps intra-plate tholeiitic lavas and dykes (Cassinis *et al.*, 2008); and iii) the alkaline dykes, apatite-rich and chromitite layers in the Ivrea zone (Ferrario & Garuti, 1990; Stähle *et al.*, 1990; 2001; Morishita *et al.*, 2003; 2008; Zaccarini *et al.*, 2004; Schaltegger *et al.*, 2015; Malitch *et al.*, 2017; Galli *et al.*, 2019). A further geochemical and geochronological comparison with the alkaline magmas at Karawanken (Austroalpine domain, Visonà & Zanferrari, 2000) is instead required, since the only available age data for this complex (230±9 Ma, Lippolt & Pidgeon, 1974) overlaps with both the ~237 Ma high-K calc-alkaline to shoshonitic and the 218.5-220.5 Ma alkaline lamprophyres of the Dolomitic Area.

8. Rather than a late-stage episode related to the Ladinian high-K calc-alkaline to shoshonitic magmatism of the Dolomitic Area, Predazzo lamprophyres should be considered part of the alkaline-carbonatitic magmatic pulse that intruded the Southern Alps subcontinental mantle between 225 and 190 Ma. Such a magmatic event likely represents a precursor of the rifting stage connected to the Alpine Tethys opening, as also suggested by its asthenospheric-influenced Sr-Nd isotopic signature. The generation of such H_2O-CO_2-rich alkaline-carbonatitic melts is therefore ascribable to mantle upwelling dynamics in a continental rifting setting (Stähle *et al.*, 1990; 2001; Zaccarini *et al.*, 2004; Batki *et al.*, 2014; Schaltegger *et al.*, 2015; Galli *et al.*, 2019).
9. Predazzo alkaline lamprophyres can be considered as geochemical and geochronological markers of the shift from orogenic-like to anorogenic magmatism in the Southern Alps. Their Sr-Nd isotopic signature and incompatible elements pattern suggest that the mantle source that generated the Ladinian (~237 Ma) subduction-related magmas was progressively being depleted, during Late Triassic, by the asthenospheric influx related to the Alpine Tethys opening.

FUNDING

This work was supported by The University Institute for Higher Studies (IUSS) Mobility Research Programme of the University of Ferrara [grant numbers 570, 571] for Long Period, 2016/2017 to [FC], the Italian National Research Program [PRIN_2017 Project 20178LPCPW] to [MC] and the Italian National Research Program [PRIN_2015/prot. 20158A9] to [CB]

ACKNOWLEDGEMENTS

NERC are acknowledged for continued funding of the Argon Isotope Facility at SUERC. Alberto Zanetti is acknowledged for LAM-ICP-MS analyses. Anne Kelly, Vincent Gallagher, Ross Dymock and Jim Imlach are thanked for making the Sr and Nd isotopic analyses and the

$^{40}Ar/^{39}Ar$ measurements at SUERC. Francesco Stoppa, Matteo Masotta and Brian Upton are acknowledged for their constructive comments to an earlier version of the paper. Editor Valentin Troll is thanked for his careful editorial guidance.

REFERENCES

Abbas, H., Michail, M., Cifelli, F., Mattei, M., Gianolla, P., Lustrino, M. & Carminati, E. (2018). Emplacement modes of the Ladinian plutonic rocks of the Dolomites: Insights from anisotropy of magnetic susceptibility. *Journal of Structural Geology* **113**, 42-61.

Akinin, V. V., Sobolev, A. V., Ntaflos, T. & Richter, W. (2005). Clinopyroxene megacrysts from Enmelen melanephelinitic volcanoes (Chukchi Peninsula, Russia): application to composition and evolution of mantle melts. *Contributions to Mineralogy and Petrology* **150(1)**, 85-101.

Armienti, P., Corazzato, C., Groppelli, G., Natoli, E. & Pasquarè, G. (2003). Geological and petrographical study of Montecampione Triassic subvolcanic bodies (Southern Alps, Italy): preliminary geodynamic results. *Italian Journal of Geosciences* **2**, 67-78.

Barbieri, G., De Vecchi, G. P., De Zanche, V., Mietto, P. & Sedea, R. (1982). Stratigrafia e petrologia del magmatismo triassico nell'area di Recoaro. Guida alla geologia del Sudalpino centro-orientale. *Società Geologica Italiana - Guide Geologiche Regionali*, 179-187.

Barfod, D. N., Mark, D. F., Tait, A., Dymock, R. C. & Imlach, J. (2014). *Argon extraction from geological samples by CO2 scanning laser step-heating*. In: Jourdan, F., Mark, D.F., & Verati, C. (eds.) *Advances in $^{40}Ar/^{39}Ar$ dating: from archaeology to planetary sciences*. Geological Society of London Special Publication **378**, 79-90.

Barry, T. L., Saunders, A. D., Kempton, P. D., Windley, B. F., Pringle, M. S., Dorjnamjaa, D. & Saandar, S. (2003). Petrogenesis of Cenozoic basalts from Mongolia: evidence for the role of asthenospheric versus metasomatized lithospheric mantle sources. *Journal of Petrology* **44(1)**, 55-91.

Batki, A., Pál-Molnár, E., Dobosi, G. & Skelton, A. (2014). Petrogenetic significance of ocellar camptonite dykes in the Ditrău Alkaline Massif, Romania. *Lithos* **200**, 181-196.

Beccaluva, L., Coltorti, M., Saccani, E., Siena, F. & Zeda, O. (2005). *Triassic Magmatism and Jurassic Ophiolites at the Margins of the Adria Plate*. In: Finetti, I.R. (ed.) *Crop Project: Deep Seismic Exploration of the Central Mediterranean and Italy*. Elsevier **28**, 607-622.

Bellieni, G., Fioretti, A. M., Marzoli, A. & Visonà, D. (2010). Permo-Paleogene magmatism in the eastern Alps. *Rendiconti Lincei* **21**, S51-S71.

Beltrán-Triviño, A., Winkler, W., von Quadt, A. & Gallhofer, D. (2016). Triassic magmatism on the transition from Variscan to Alpine cycles: evidence from U–Pb, Hf, and geochemistry of detrital minerals. *Swiss Journal of Geosciences* **109(3)**, 309-328.

Bernoulli, D. & Lemoine, M. (1980). Birth and Early Evolution of the Tethys: the Overall Situation. *Mémoires du Bureau de recherches géologiques et minières* **115**, 168-179.

Bianchini, G., Natali, C., Shibata, T. & Yoshikawa, M. (2018). Basic dykes crosscutting the crystalline basement of Valsugana (Italy): new evidence of early Triassic volcanism in the Southern Alps. *Tectonics* **37(7)**, 2080-2093.

Bonadiman, C., Coltorti, M. & Siena, F. (1994). Petrogenesis and *T*-fO_2 estimates of Mt. Monzoni complex (Central Dolomites, Southern Alps): a Triassic shoshonitic intrusion in a trascurrent geodynamic setting. *European Journal of Mineralogy* **6**, 943-966.

Brack, P., Mundil, R., Oberli, F., Meier, M. & Rieber, H. (1996). Biostratigraphic and radiometric age data question the Milankovitch characteristics of the Latemar cycles (Southern Alps, Italy). *Geology* **24(4)**, 371-375.

Buckley, H. A. & Woolley, A. R. (1990). Carbonates of the magnesite-siderite series from four carbonatite complexes. *Mineralogical Magazine* **54(376)**, 413-418.

Carraro, A. & Visonà, D. (2003). Mantle xenoliths in Triassic camptonite dykes of the Predazzo Area (Dolomites, Northern Italy). *European Journal of Mineralogy* **15(1)**, 103-115.

Casetta, F., Coltorti, M., Ickert, R. B., Bonadiman, C., Giacomoni, P. P. & Ntaflos, T. (2018a). Intrusion of shoshonitic magmas at shallow crustal depth: *T–P* path, H_2O estimates, and AFC modeling of the Middle Triassic Predazzo Intrusive Complex (Southern Alps, Italy). *Contributions to Mineralogy and Petrology* **173(7)**, 57.

Casetta, F., Coltorti, M. & Marrocchino, E. (2018b). Petrological evolution of the Middle Triassic Predazzo Intrusive Complex, Italian Alps. *International Geology Review* **60(8)**, 977-997.

Cassinis, G., Cortesogno, L., Gaggero, L., Perotti, C. R. & Buzzi, L. (2008). Permian to Triassic geodynamic and magmatic evolution of the Brescian Prealps (eastern Lombardy, Italy): *Italian Journal of Geosciences* **127(3)**, 501-518.

Castellarin, A., Lucchini, F., Rossi, P. L., Selli, L. & Simboli, G. (1988). The Middle Triassic magmatic-tectonic arc development in the Southern Alps. *Tectonophysics* **146(1-4)**, 79-89.

Coltorti, M. & Siena, F. (1984). Mantle tectonite and fractionate peridotite at Finero (Italian Western Alps). *Neues Jahrbuch fur Mineralogie-Abhandlungen* **149(3)**, 225-244.

Dal Piaz, G., Bistacchi, A. & Massironi, M. (2003). Geological outline of the Alps. *Episodes* **26(3)**, 175-180.

Dallmeyer, D.R., Kräutner, H.G. & Neubauer, F. (1997). Middle-late Triassic $^{40}Ar/^{39}Ar$ hornblende ages for early intrusions within the Ditrau alkaline massif, Rumania: Implications for Alpine rifting in the Carpathian orogen. *Geologica Carpathica* **48(6)**, 347-352.

Doglioni, C. (1984). Triassic diapiric structure in the central Dolomites (Northen Italy). *Eclogae Geologicae Helvetiae* **77**, 2.

Doglioni, C. (1987). Tectonics of the Dolomites (Southern Alps, Northern Italy). *Journal of Structural Geology* **9**, 181-193.

Doglioni, C. (2007). Tectonics of the Dolomites. *Bulletin für angewandte Geologie* **12(2)**, 11-15.

Doglioni, C., & Carminati, E. (2008). Structural styles and Dolomites field trip. *Memorie Descrittive della Carta Geologica d'Italia* **82**, 301.

Ellis, B. S., Mark, D. F., Pritchard, C. J. & Wolff, J. A. (2012). Temporal dissection of the Huckleberry Ridge Tuff using the $^{40}Ar/^{39}Ar$ dating technique. *Quaternary Geochronology* **9**, 34-41.

Falloon, T. J. & Green, D. H. (1988). Anhydrous partial melting of peridotite from 8 to 35 kb and the petrogenesis of MORB. *Journal of Petrology* **1**, 379-414.

Ferrario, A. & Garuti, G. (1990). Platinum-group mineral inclusions in chromitites of the Finero mafic-ultramafic complex (Ivrea-Zone, Italy). *Mineralogy and Petrology* **41(2-4)**, 125-143.

Frost, D.J. (2006). The stability of hydrous mantle phases. *Reviews in Mineralogy and Geochemistry* **62(1)**, 243-271.

Fujimaki, H., Tatsumoto, M. & Aoki, K. I. (1984). Partition coefficients of Hf, Zr, and REE between phenocrysts and groundmasses. *Journal of Geophysical Research: Solid Earth* **89(S02)**, B662-B672.

Fumagalli, P., Zanchetta, S. & Poli, S. (2009). Alkali in phlogopite and amphibole and their effects on phase relations in metasomatized peridotites: a high-pressure study. *Contributions to Mineralogy and Petrology* **158(6)**, 723.

Galassi, B., Monese, A., Ogniben, G., Siena, F. & Vaccaro, C. (1994). Age and nature of lamprophyric dykes at Calceranica (Trento). *Mineralogica et Petrographica Acta* **37**, 163-171.

Galli, A., Grassi, D., Sartori, G., Gianola, O., Burg, J. P. & Schmidt, M. W. (2019). Jurassic carbonatite and alkaline magmatism in the Ivrea zone (European Alps) related to the breakup of Pangea. *Geology*.

Gasparotto, G. & Simboli, G. (1991). Mineralogia, petrografia e schemi evolutivi delle magmatiti triassiche del complesso di Cima Pape (Dolomiti Orientali). *Mineralogica et Petrografica Acta* **34**, 205-234.

Giacomoni, P. P., Coltorti, M., Bryce, J. G., Fahnestock, M. F. & Guitreau, M. (2016). Mt. Etna plumbing system revealed by combined textural, compositional, and thermobarometric studies in clinopyroxenes. *Contributions to Mineralogy and Petrology* **171(4)**, 34.

Giacomoni, P. P., Ferlito, C., Coltorti, M., Bonadiman, C. & Lanzafame, G. (2014). Plagioclase as archive of magma ascent dynamics on "open conduit" volcanoes: The 2001-2006 eruptive period at Mt. Etna. *Earth-Science Reviews* **138**, 371-393.

Gianolla, P. (1992). Evoluzione mediotriassica del vulcanismo di Rio Freddo (Api Giulie, Italia). *Memorie di Scienze Geologiche* **44**, 193-209.

Gozzi, F., Gaeta, M., Freda, C., Mollo, S., Di Rocco, T., Marra, F., ... & Pack, A. (2014). Primary magmatic calcite reveals origin from crustal carbonate. *Lithos* **190**, 191-203.

Hammouda, T., & Keshav, S. (2015). Melting in the mantle in the presence of carbon: Review of experiments and discussion on the origin of carbonatites. *Chemical Geology* **418**, 171-188.

Hawthorne, F. C., Oberti, R., Harlow, G. E., Maresch, W. V., Martin, R. F., Schumacher, J. C. & Welch, M.D. (2012). Nomenclature of the amphibole supergroup. *American Mineralogist* **97(11-12)**, 2031-2048.

Hay, R. L. & O'Neil, J. R. (1983). Carbonatite tuffs in the Laetolil Beds of Tanzania and the Kaiserstuhl in Germany. *Contributions to Mineralogy and Petrology* **82(4)**, 403-406.

Hogarth, D. D. (1989). *Pyrochlore, apatite and amphibole: distinctive minerals in carbonatite*. In: Bell, K. (ed.) *Carbonatites: Genesis and Evolution*. Unwin Hyman, London, 103-148.

Ickert, R. B. (2013). Algorithms for estimating uncertainties in initial radiogenic isotope ratios and model ages. *Chemical Geology* **340**, 131-138.

Ishibashi H. (2013). Spinel-melt oxygen barometry: a method and application to Cenozoic alkali basaltic magmas from the Higashi-Matsuura district, NW Kyushu. *Japan Geoscience Reports* **40**, 21-32.

Kinzler, R. J. & Grove, T. L. (1992). Primary magmas of mid-ocean ridge basalts 1. Experiments and methods. *Journal of Geophysical Research: Solid Earth* **97(B5)**, 6885-6906.

Kress, V. C. & Carmichael, I. S. (1991). The compressibility of silicate liquids containing Fe_2O_3 and the effect of composition, temperature, oxygen fugacity and pressure on their redox states. *Contributions to Mineralogy and Petrology* **108(1-2)**, 82-92.

Langone, A., Zanetti, A., Daczko, N. R., Piazolo, S., Tiepolo, M. & Mazzucchelli, M. (2018). Zircon U-Pb Dating of a Lower Crustal Shear Zone: A Case Study From the Northern Sector of the Ivrea-Verbano Zone (Val Cannobina, Italy). *Tectonics* **37(1)**, 322-342.

Leat, P. T., Riley, T. R., Storey, B. C., Kelley, S. P. & Millar, I. L. (2000). Middle Jurassic ultramafic lamprophyre dyke within the Ferrar magmatic province, Pensacola Mountains, Antarctica. *Mineralogical Magazine* **64(1)**, 95-111.

Lee, J-Y., Marti, K., Severinghaus, J. P., Kawamura, K., Yoo, H. S., Lee, J. B., & Kim, J. S. (2006). A redetermination of the isotopic abundances of atmospheric Ar. *Geochimica et Cosmochimica Acta* **70**, 4507-4512.

Le Maitre, R.W., Bateman, P., Dudek, A., Keller, J., Lameyre, L., Sabine, P. A., ... & Zanettin, B., 1989. *A classification of igneous rocks and glossary of terms: recommendations of the IUGS Commission on the Systematics of Igneous Rocks.*

Le Maitre, R. W., Streckeisen, A., Zanettin, B., Le Bas, M. J., Bonin, B., Bateman, P., … & Lameyre, J. (2002). *Igneous rocks. A classification and glossary of terms. Recommendations of the IUGS Subcomission on the Systematics of Igneous Rocks.* Cambridge University Press.

Le Roex, A. P. & Lanyon, R. (1998). Isotope and trace element geochemistry of Cretaceous Damaraland lamprophyres and carbonatites, northwestern Namibia: Evidence for plume-lithosphere interactions. *Journal of Petrology* **39(6)**, 1117-1146.

Lippolt, H. & Pidgeon, R. (1974). Isotopic mineral ages of a diorite from the Eisenkappel intrusion, Austria. *Zeitschrift für Naturforschung* **29a**.

Locock, A. J. (2014). An Excel spreadsheet to classify chemical analyses of amphiboles following the IMA 2012 recommendations. *Computers & Geosciences* **62**, 1-11.

Lu, Y. J., McCuaig, T. C., Li, Z. X., Jourdan, F., Hart, C. J., Hou, Z. Q. & Tang, S.H. (2015). Paleogene post-collisional lamprophyres in western Yunnan, western Yangtze Craton: mantle source and tectonic implications. *Lithos* **233**, 139-161.

Lucchini, F., Mezzetti, R. & Simboli, G. (1969). The lamprophyres of the area Predazzo-Monzoni: camptonites. *Mineralogica et Petrografica Acta* **15**, 109-145.

Lucchini, F., Rossi, P. L. & Simboli, G. (1982). *Il magmatismo triassico dell'area di Predazzo (Alpi Meridionali, Italia)*. In: Castellarin, A. & Vai, G. B. (eds.). *Guida alla Geologia del Sudalpino centro-orientale*. Guide Geologiche Regionali Società Geologica Italiana, 221-230.

Lugmair, G. W. & Marti, K. (1978). Lunar initial $^{143}Nd/^{144}Nd$: differential evolution of Lunar crust and mantle. *Earth and Planetary Science Letters* **39**, 349-357.

Malitch, K. N., Belousova, E. A., Griffin, W. L., Badanina, I. Y., Knauf, V. V., O'Reilly, S. Y. & Pearson, N.J. (2017). Laurite and zircon from the Finero chromitites (Italy): New insights into evolution of the subcontinental mantle. *Ore Geology Reviews* **90**, 210-225.

Mandler, B. E. & Grove, T. L. (2016). Controls on the stability and composition of amphibole in the Earth's mantle. *Contributions to Mineralogy and Petrology* **171(8-9)**, 68.

Mark, D. F., Rice, C. M., Lee, M. R., Fallick, A. E., Boyce, A., Trewin, N. H. & Lee, J. K. W. (2011a). $^{40}Ar/^{39}Ar$ dating of hydrothermal activity, biota and gold mineralization in the Rhynie hot-spring system, Aberdeenshire, Scotland. *Geochimica et Cosmochimica Acta* **75**, 555-569.

Mark, D. F., Stuart, F. M. & De Podesta, M. (2011b). New high-precision measurements of the isotopic composition of atmospheric argon. *Geochimica et Cosmochimica Acta* **75(23)**, 7494-7501.

Marrocchino, E., Coltorti, M., Visonà, D. & Thirwall, M. F. (2002). Petrology of Predazzo magmatic complex (Trento, Italy). *Geochimica et Cosmochimica Acta* **66(15a)**, A486-A486.

Matsumoto, T., Morishita, T., Matsuda, J. I., Fujioka, T., Takebe, M., Yamamoto, K. & Arai, S. (2005). Noble gases in the Finero phlogopite-peridotites, western Italian Alps. *Earth and Planetary Science Letters* **238(1-2)**, 130-145.

Mazzucchelli, M., Rivalenti, G., Brunelli, D., Zanetti, A. & Boari, E. (2009). Formation of highly refractory dunite by focused percolation of pyroxenite-derived melt in the Balmuccia peridotite massif (Italy). *Journal of Petrology* **50(7)**, 1205-1233.

McKenzie, D. A. N. & O'nions, R. K. (1991). Partial melt distributions from inversion of rare earth element concentrations. *Journal of Petrology* **32(5)**, 1021-1091.

Meschede, M. (1986). A method of discriminating between different types of mid-ocean ridge basalts and continental tholeiites with the Nb-Zr-Y diagram. *Chemical geology* **56(3-4)**, 207-218.

Mietto, P., Manfrin, S., Preto, N., Rigo, M., Roghi, G., Furin, S., Gianolla, P., Posenato, R., ... & Bowring, S.A. (2012). The Global Boundary Stratotype Section and Point (GSSP) of the Carnian Stage (Late Triassic) at Prati di Stuores/ Stuores Wiesen Section (Southern Alps, NE Italy). *Episodes* **35(3)**, 414-430.

Moore, J. M., Kuhn, B. K., Mark, D. F. & Tsikos, H. (2011). A sugilite-bearing assemblage from the Wolhaarkop breccia, Bruce iron-ore mine, South Africa: Evidence for alkali metasomatism and ^{40}Ar-^{39}Ar dating. *European Journal of Mineralogy* **23(4)**, 661-673.

Morgan, L. E., Mark, D. F., Imlach, J., Barfod, D. & Dymock, R. (2014). FCs-EK: a new sampling of the Fish Canyon Tuff ^{40}Ar/^{39}Ar neutron flux monitor. *Geological Society of London, Special Publications* **378(1)**, 63-67.

Morimoto, N. (1988). Nomenclature of pyroxenes. *Mineralogy and Petrology* **39(1)**, 55-76.

Morishita, T., Arai, S. & Tamura, A. (2003). Petrology of an apatite-rich layer in the Finero phlogopite–peridotite, Italian Western Alps; implications for evolution of a metasomatising agent. *Lithos* **69(1-2)**, 37-49.

Morishita, T., Hattori, K. H., Terada, K., Matsumoto, T., Yamamoto, K., Takebe, M., ... & Arai, S. (2008). Geochemistry of apatite-rich layers in the Finero phlogopite–peridotite massif (Italian Western Alps) and ion microprobe dating of apatite. *Chemical Geology* **251(1-4)**, 99-111.

Morogan, V., Upton, B. G. J., & Fitton, J. G. (2000). The petrology of the Ditrau alkaline complex, Eastern Carpathians. *Mineralogy and Petrology* **69(3-4)**, 227-265.

Morten, L. (1980). Mineral chemistry of ultramafic inclusions from the Predazzo volcanic rocks. Dolomite Region, north Italy. *Journal of Mineralogy and Geochemistry* **138**, 259-273.

Mukasa, S.B. & Shervais, J. W. (1999). Growth of subcontinental lithosphere: evidence from repeated dike injections in the Balmuccia lherzolite massif, Italian Alps. *Lithos* **48**, 287-316.

Mundil, R., Brack, P. & Laurenzi, M. A. (1996). High resolution U/Pb single zircon age determinations: new constraints on the timing of Middle Triassic magmatism in the Southern Alps. *Conference abstract, 78° Riunione estiva S.G.I.*

Oberti, R., Cannillo, E. & Toscani, G. (2012). How to name amphiboles after the IMA2012 report: rules of thumb and a new PC program for monoclinic amphiboles. *Periodico di Mineralogia* **81(2)**, 257-267.

Pál-Molnár, E., Batki, A., Almási, E., Kiss, B., Upton, B. G., Markl, G., ... & Harangi, S. (2015). Origin of mafic and ultramafic cumulates from the Ditrău Alkaline Massif, Romania. *Lithos* **239**, 1-18.

Pamić, J. J. (1984). Triassic magmatism of the Dinarides in Yugoslavia. *Tectonophysics* **109(3-4)**, 273-307.

Pană, D., Balintoni, I. & Heaman, L. (2000). Precise U-Pb zircon dating of the syenite phase from the Ditrau alkaline igneous complex. *Studia UBB Geologia* **45(1)**, 79-90.

Pandey, A., Rao, N. C., Chakrabarti, R., Pandit, D., Pankaj, P., Kumar, A. & Sahoo, S. (2017a). Petrogenesis of a Mesoproterozoic shoshonitic lamprophyre dyke from the Wajrakarur kimberlite field, eastern Dharwar craton, southern India: geochemical and Sr-Nd isotopic evidence for a modified sub-continental lithospheric mantle source. *Lithos* **292**, 218-233.

Pandey, A., Rao, N. C., Pandit, D., Pankaj, P., Pandey, R., Sahoo, S. & Kumar, A. (2017b). Subduction–tectonics in the evolution of the eastern Dharwar craton, southern India: Insights from the post-collisional calc-alkaline lamprophyres at the western margin of the Cuddapah basin. *Precambrian Research* **298**, 235-251.

Pearce, J. A. (1982). *Trace element characteristics of lavas from destructive plate boundaries.* In: Thorpe E. S. (ed.) *Andesites.* New York, John Wiley and Sons **8**, 525-548.

Pearce, J. A. & Norry, M. J. (1979). Petrogenetic implications of Ti, Zr, Y, and Nb variations in volcanic rocks. *Contributions to Mineralogy and Petrology* **69(1)**, 33-47.

Pe-Piper, G. (1998). The nature of Triassic extension-related magmatism in Greece: evidence from Nd and Pb isotope geochemistry. *Geological Magazine* **135(3)**, 331-348.

Petrone, C. M., Braschi, E., Francalanci, L., Casalini, M. & Tommasini, S. (2018). Rapid mixing and short storage timescale in the magma dynamics of a steady-state volcano. *Earth and Planetary Science Letters* **492**, 206-221.

Pilet, S., Ulmer, P. & Villiger, S. (2010). Liquid line of descent of a basanitic liquid at 1.5 GPa: constraints on the formation of metasomatic veins. *Contributions to Mineralogy and Petrology* **159(5)**, 621-643.

Pinzuti, P., Humler, E., Manighetti, I. & Gaudemer, Y. (2013). Petrological constraints on melt generation beneath the Asal Rift (Djibouti) using quaternary basalts. *Geochemistry, Geophysics, Geosystems* **14(8)**, 2932-2953.

Pouchou, J. L. & Pichoir, F. (1991). *Quantitative analysis of homogeneous or stratified microvolumes applying the model "PAP"*. In: *Electron probe quantitation*. Springer US, 31-75.

Putirka, K. D., Johnson, M., Kinzler, R., Longhi, J. & Walker, D. (1996). Thermobarometry of mafic igneous rocks based on clinopyroxene-liquid equilibria, 0–30 kbar. *Contributions to Mineralogy and Petrology* **123(1)**, 92-108.

Putirka, K. D. (2008). Thermometers and barometers for volcanic systems. *Reviews in Mineralogy and Geochemistry* **69(1)**, 61-120.

Putirka, K. D. (2016). Amphibole thermometers and barometers for igneous systems and some implications for eruption mechanisms of felsic magmas at arc volcanoes. *American Mineralogist* **101(4)**, 841-858.

Raffone, N., Le Fèvre, B., Ottolini, L., Vannucci, R. & Zanetti, A. (2006). Light-lithophile element metasomatism of Finero peridotite (W Alps): a secondary-ion mass spectrometry study. *Microchimica Acta* **155(1-2)**, 251-255.

Renne, P. R., Deino, A. L., Hames, W. E., Heizler, M. T., Hemming, S. R., Hodges, K. V., Koppers, A. A. P., Mark, D. F., … & Wijbrans, J.R. (2009). Data Reporting Norms for $^{40}Ar/^{39}Ar$ Geochronology. *Quaternary Geochronology* **4**, 346-352.

Renne, P. R., Mundil, R., Balco, G., Min, K. & Ludwig, K. R. (2010). Joint determination of ^{40}K decay constants and $^{40}Ar^*/^{40}K$ for the Fish Canyon sanidine standard, and improved accuracy for $^{40}Ar/^{39}Ar$ geochronology. *Geochimica et Cosmochimica Acta* **74**, 5349-5367.

Renne, P. R., Balco, G., Ludwig, K. R., Mundil, R. & Min, K. (2011). Response to comment by W.H. Schwarz *et al.* on 'Joint determination of ^{40}K decay constants and $^{40}Ar^*/^{40}K$ for the Fish Canyon sanidine standard, and improved accuracy for $^{40}Ar/^{39}Ar$ geochronology' by P.R. Renne *et al.*, 2010. *Geochimica et Cosmochimica Acta* **75**, 5097-5100.

Ridolfi, F., Renzulli, A. & Puerini, M. (2010). Stability and chemical equilibrium of amphibole in calc-alkaline magmas: an overview, new thermobarometric formulations and application to subduction-related volcanoes. *Contributions to Mineralogy and Petrology* **160(1)**, 45-66.

Robinson, J. A. C. & Wood, B. J. (1998). The depth of the spinel to garnet transition at the peridotite solidus. *Earth and Planetary Science Letters* **164(1-2)**, 277-284.

Rock, N. M. S. (1987). The nature and origin of lamprophyres: an overview. *Geological Society of London, Special Publications* **30(1)**, 191-226.

Rock, N. M. S. (1991). *Lamprophyres*. Springer.

Rotenberg, E., Davis, D. W., Amelin, Y., Ghosh, S. & Bergquist, B. A. (2012). Determination of the decay-constant of ^{87}Rb by laboratory accumulation of ^{87}Sr. *Geochimica et Cosmochimica Acta* **85**, 41-57.

Ruiz-Agudo, E., Putnis, C. V. & Putnis, A. (2014). Coupled dissolution and precipitation at mineral–fluid interfaces. *Chemical Geology* **383**, 132-146.

Saccani, E. (2015). A new method of discriminating different types of post-Archean ophiolitic basalts and their tectonic significance using Th-Nb and Ce-Dy-Yb systematics. *Geoscience Frontiers* **6(4)**, 481-501.

Scarrow, J. H., Molina, J. F., Bea, F., Montero, P. & Vaughan, A. P. (2011). Lamprophyre dikes as tectonic markers of late orogenic transtension timing and kinematics: A case study from the Central Iberian Zone. *Tectonics*, **30(4)**.

Schaltegger, U., Ulianov, A., Müntener, O., Ovtcharova, M., Peytcheva, I., Vonlanthen, P., Vennemann, T., Antognini, A. & Girlanda, F. (2015). Megacrystic zircon with planar fractures in miaskite-type nepheline pegmatites formed at high pressures in the lower crust (Ivrea Zone, southern Alps, Switzerland). *American Mineralogist* **100(1)**, 83-94.

Schmid, M. S., Bernoulli, D., Fügenschuh, B., Georgiev, N., Kounov, A., Matenco, L., Oberhansli, R., Pleuger, J., Schefer, S., Ustaszewski, K. & Van Hinsbergen, D. (2016).

Tectonic units of the Alpine collision zone between Eastern Alps and Western Turkey: *Unpublished map*.

Schmid, S. M., Bernoulli, D., Fügenschuh, B., Matenco, L., Schefer, S., Schuster, R., Tischler, M. & Ustaszewski, K. (2008). The Alpine-Carpathian-Dinaridic orogenic system: correlation and evolution of tectonic units. *Swiss Journal of Geosciences* **101(1)**, 139-183.

Schmidt, K. H., Bottazzi, P., Vannucci, R. & Mengel, K. (1999). Trace element partitioning between phlogopite, clinopyroxene and leucite lamproite melt. *Earth and Planetary Science Letters* **168(3)**, 287-299.

Seghedi, I., Downes, H., Vaselli, O., Szakács, A., Balogh, K. & Pécskay, Z. (2004). Post-collisional Tertiary-Quaternary mafic alkalicmagmatism in the Carpathian–Pannonian region: a review. *Tectonophysics* **393**, 43–62.

Shaw, D. M. (1970). Trace element fractionation during anatexis. *Geochimica et Cosmochimica Acta* **34(2)**, 237-243.

Sloman, L. E. (1989). Triassic shoshonites from the dolomites, northern Italy: Alkaline arc rocks in a strike-slip setting. *Journal of Geophysical Research: Solid Earth* **94(B4)**, 4655-4666.

Smith, E. I., Sanchez, A., Walker, J. D. & Wang, K. (1999). Geochemistry of mafic magmas in the Hurricane Volcanic field, Utah: implications for small-and large-scale chemical variability of the lithospheric mantle. *The Journal of Geology* **107(4)**, 433-448.

Soder, C. & Romer, R. L. (2018). Post-collisional potassic–ultrapotassic magmatism of the Variscan Orogen: implications for mantle metasomatism during continental subduction. *Journal of Petrology* **59(6)**, 1007-1034.

Stahle, V., Frenzel, G., Hess, J. C., Saupé, F., Schmidt, S. T. & Schneider, W. (2001). Permian metabasalt and Triassic alkaline dykes in the northern Ivrea zone: clues to the post-Variscan geodynamic evolution of the Southern Alps. *Schweizerische Mineralogische und Petrographische Mitteilungen* **81(1)**, 1-21.

Stähle, V., Frenzel, G., Kober, B., Michard, A., Puchelt, H. & Schneider, W. (1990). Zircon syenite pegmatites in the Finero peridotite (Ivrea zone): evidence for a syenite from a mantle source. *Earth and Planetary Science Letters* **101(2-4)**, 196-205.

Stampfli, G.M. (2005). *Plate Tectonics of the Apulia-Adria Microcontinents*. In: Finetti, I. R. (ed.) *Crop Project: Deep Seismic Exploration of the Central Mediterranean and Italy*. Elsevier **28**, 747-766.

Stampfli, G. M. & Borel, G. D. (2002). A plate tectonic model for the Paleozoic and Mesozoic constrained by dynamic plate boundaries and restored synthetic oceanic isochrones. *Earth and Planetary Science Letters* **196(1)**, 17-33.

Stampfli, G. M. & Borel, G. D. (2004). *The TRANSMED transects in space and time: constraints on the paleotectonic evolution of the Mediterranean domain*. In: The TRANSMED Atlas: The Mediterranean region from crust to mantle, 53-80.

Stampfli, G. M., Borel, G. D., Marchant, R. & Mosar, J. (2002). Western Alps geological constraints on western Tethyan reconstructions. *Journal of the Virtual Explorer* **8**, 77.

Stoppa, F. (2008). *Alkaline and ultramafic lamprophyres in Italy: Distribution, mineral phases, and bulk rock data. Deep-Seated Magmatism, Its Sources and Plumes*. Publishing House of the Institute of Geography, SB RAS, 209-238.

Stoppa, F., Rukhlov, A.S., Bell, K., Schiazza, M. & Vichi, G. (2014). Lamprophyres of Italy: early cretaceous alkaline lamprophyres of southern Tuscany, Italy. *Lithos* **188**, 97-112.

Storck, J-C., Brack, P., Wotzlaw, J-F & Ulmer, P. (2018). Timing and evolution of Middle Triassic magmatism in the Southern Alps (Northern Italy). *Journal of the Geological Society* **123**.

Sun, S. & McDonough, W. F. (1989). *Chemical and isotopic systematics of oceanic basalts: implication for mantle and processes*. In: Saunders A. D. & Norry M. J. (eds.) *Magmatism in the Ocean Basins*. Geological Society, Special Publications, **42**, 313-345.

Takahashi, E. & Kushiro, I. (1983). Melting of a dry peridotite at high pressures and basalt magma genesis. *American Mineralogist* **68(9-10)**, 859-879.

Tiepolo, M., Bottazzi, P., Palenzona, M. & Vannucci, R. (2003). A laser probe coupled with ICP–double-focusing sector-field mass spectrometer for in situ analysis of geological samples and U-Pb dating of zircon. *The Canadian Mineralogist* **41(2)**, 259-272.

Traill, R. J. & Lachance, G. R. (1966). A practical solution to the matrix problem in X-ray analysis. II. Application to a multicomponent alloy system. Canadian Spectroscopy **11(3)**, 63-71.

Tumiati, S., Fumagalli, P., Tiraboschi, C. & Poli, S. (2013). An experimental study on COH-bearing peridotite up to 3.2 GPa and implications for crust–mantle recycling. *Journal of Petrology* **54(3)**, 453-479.

Ubide, T., Galé, C., Arranz, E., Lago, M. & Larrea, P. (2014). Clinopyroxene and amphibole crystal populations in a lamprophyre sill from the Catalonian Coastal Ranges (NE Spain): a record of magma history and a window to mineral-melt partitioning. *Lithos* **184**, 225-242.

Vardabasso, S. (1929). Rapporti tra attività magmatica e vicende tettoniche nella provincia petrografica di Predazzo. *Studi Trentini di Scienze Naturali* **11**.

Velde, D. (1968). Les transformations de l'olivine dans les lamprophyres et lamproites; une etude de la pilite. *Bulletin de la Société Géologique de France* **7(5)**, 601-612.

Vichi, G., Stoppa, F. & Wall, F. (2005). The carbonate fraction in carbonatitic Italian lamprophyres. *Lithos* **85(1-4)**, 154-170.

Visonà, D. & Zanferrari, A (2000). Some constraints on geochemical features in the Triassic mantle of the easternmost Austroalpine-Southalpine domain: evidence from the Karawanken pluton (Carinthia, Austria). *International Journal of Earth Sciences* **89(1)**, 40-51.

Voshage, H., Hunziker, J. C., Hofmann, A. W. & Zingg, A. (1987). A Nd and Sr isotopic study of the Ivrea zone, Southern Alps, N-Italy. *Contributions to Mineralogy and Petrology* **97**, 31-42.

Wallace, M.E. & Green, D.H. (1988). An experimental determination of primary carbonatite magma composition. *Nature* **335**, 343-346.

Whitney, D. L. & Evans, B. W. (2010). Abbreviations for names of rock-forming minerals. *American Mineralogist* **95**, 185-187.

Wood, D.A. (1980). The application of a Th-Hf-Ta diagram to problems of tectonomagmatic classification and to establishing the nature of crustal contamination of basaltic lavas of the British Tertiary Volcanic Province. *Earth and Planetary Science Letters* **50(1)**, 11-30.

Woolley, A. R., Bergman, S. C., Edgar, A. D., Le Bas, M. J., Mitchell, R. H., Rock, N. M. S. & Scott Smith, B. H. (1996). Classification of lamprophyres, lamproites, kimberlites, and the kalsilitic, melilitic, and leucitic rocks. *The Canadian Mineralogist* **34(2)**, 175-186.

Workman, R. K. & Hart, S. R. (2005). Major and trace element composition of the depleted MORB mantle (DMM). *Earth and Planetary Science Letters* **231(1)**, 53-72.

Wotzlaw, J. F., Brack, P. & Storck, J. C. (2018). High-resolution stratigraphy and zircon U–Pb geochronology of the Middle Triassic Buchenstein Formation (Dolomites, northern Italy): precession-forcing of hemipelagic carbonate sedimentation and calibration of the Anisian-Ladinian boundary interval. *Journal of the Geological Society* **175(1)**, 71-85.

Zaccarini, F., Stumpfl, E. F. & Garuti, G. (2004). Zirconolite and Zr–Th–U minerals in chromitites of the Finero complex, Western Alps, Italy: evidence for carbonatite-type metasomatism in a subcontinental mantle plume. *The Canadian Mineralogist* **42(6)**, 1825-1845.

Zack, T. & Brumm, R. (1998). *Ilmenite/liquid partition coefficients of 26 trace elements determined through ilmenite/clinopyroxene partitioning in garnet pyroxene*. In: Gurney, J. J., Gurney, J. L., Pascoe, M. D. & Richardson, S. H. (eds.) *7th International Kimberlite Conference*. Red Roof Design, Cape Town, 986-988.

Zaitsev, A. N., Sitnikova, M. A., Subbotin, V. V., Fernández-Suárez, J., Jeffries, T. E. & Wall, F. (2004). Sallanlatvi complex: a rare example of magnesite and siderite carbonatites.

Phoscorites and carbonatites from mantle to mine: the key example of the Kola Alkaline Province. *Mineralogical Society of London*, 201-245.

Zanetti, A., Giovanardi, T., Langone, A., Tiepolo, M., Wu, F. Y., Dallai, L. & Mazzucchelli, M. (2016). Origin and age of zircon-bearing chromitite layers from the Finero phlogopite peridotite (Ivrea-Verbano Zone, Western Alps) and geodynamic consequences. *Lithos* **262**, 58-74.

Zanetti, A., Mazzucchelli, M., Rivalenti, G. & Vannucci, R. (1999). The Finero phlogopite-peridotite massif: an example of subduction-related metasomatism. *Contributions to Mineralogy and Petrology* **134(2-3)**, 107-122.

Zanetti, A., Mazzucchelli, M., Sinigoi, S., Giovanardi, T., Peressini, G. & Fanning, M. (2013). SHRIMP U–Pb Zircon Triassic intrusion age of the Finero mafic complex (Ivrea–Verbano zone, Western Alps) and its geodynamic implications. *Journal of Petrology* **54(11)**, 2235-2265.

Ziegler, P. A. & Stampfli, G. M. (2001). Late Palaeozoic-Early Mesozoic plate boundary reorganization: collapse of the Variscan orogen and opening of Neotethys. *Natura Bresciana* **25**, 17-34.

Zindler, A. & Hart, S. R. (1986). Chemical geodynamics. *Annual Review of Earth and Planetary Sciences* **14**, 493-571.

FIGURE CAPTIONS

Fig. 1. (colour online)

(**a**) Map of the tectonic units of the eastern portion of the Alps (partly modified from Castellarin *et al.*, 1988; Dal Piaz *et al.*, 2003; Schmid *et al.*, 2016). LO: Ligurian Ophiolites; AM: deformed Adriatic margin; AD: Adriatic Microplate; SA: Southern Alps; DI: Dinarides; SM: Southern margin of Meliata; HB: Eoalpine High-Pressure Belt; TW: Tauern tectonic Window; EW: Engadine tectonic Window; OTW: Ossola-Tessin tectonic Window; EA: Eastern Austroalpine;

H: Helvetic domain; M: Molasse foredeep. The Middle Triassic magmatic occurrences in the Southern Alps domain are evidenced in black. They are, from west to east: Brescian Alps, Alto Vicentino, Valsugana, Dolomitic Area (identified by the circle), Carnia and Karawanken. (**b**) Simplified geological map of the Predazzo Intrusive Complex (PIC), showing the occurrence of lamprophyric dykes (modified from Casetta *et al.*, 2018*a*). SS: Shoshonitic Silica Saturated unit; SU: Shoshonitic Silica Undersaturated unit; GU: Granitic Unit. (**c**) Lamprophyric dyke intruded in the syenogranites (Sygr) at Predazzo. (**d**) Amphibole megacryst (indicated by the arrow) and (**e**) clinopyroxenitic xenolith included in the lamprophyric rocks.

Fig. 2. (colour online)

Photomicrographs in transmitted plane-polarized light of (**a**) a less evolved and (**b**) a more evolved (sample MA1) camptonite. Amp: amphibole; Cpx: clinopyroxene; Ol: olivine; Pl: plagioclase; Ti-Mag: Ti-magnetite. Mineral abbreviations following Whitney & Evans (2010).

Fig. 3. (colour online)

(**a**) K_2O vs. Na_2O diagram, (**b**) Cr vs. MgO and (**c**) Ni vs. MgO variations diagrams for Predazzo camptonites. (**d**) Al_2O_3-MgO-CaO and (**e**) $SiO_2/10$-CaO-$TiO_2\times4$ ternary diagrams showing the composition of Predazzo camptonites compared to those of worldwide alkaline lamprophyres (AL), ultramafic lamprophyres (UML) and calc-alkaline lamprophyres (CAL; data from Rock, 1991). The compositional field of Cretaceous to Oligocenic Italian lamprophyres (grey field) is also reported for comparison (data from Stoppa *et al.*, 2014).

Fig. 4. (colour online)

Chondrite-normalized (Sun & McDonough, 1989) trace element (**a**) and REE patterns (**b**) of Predazzo camptonites. The OIB pattern (Sun & McDonough, 1989), the average composition of the worldwide camptonites (Rock, 1991), Italian lamprophyres (Galassi *et al.*, 1994; Vichi

et al., 2005; Stoppa *et al.*, 2008; 2014), Ditrau lamprophyres (Batki *et al.*, 2014) and Predazzo Intrusive Complex Shoshonitic Silica Saturated (SS) and Undersaturated (SU) rocks (Casetta *et al.*, 2018a; 2018*b*) are reported for comparison.

Fig. 5. (colour online)

Trace element discrimination diagrams for Predazzo camptonites: (**a**) Th_N vs. Nb_N diagram (Saccani, 2015); (**b**) Ti/Y vs. Nb/Y diagram (Pearce, 1982); (**c**) Zr/Y vs. Zr diagram (Pearce and Norry, 1979); (**d**) Th-Hf-Ta ternary diagram (Wood, 1980); (**e**) Zr-Nb-Y ternary diagram (Meschede, 1986). Fractional Crystallization (FC) and Assimilation and Fractional Crystallization (AFC) vectors reported in (**a**) are in accordance with Saccani (2015).

Fig. 6. (colour online)

Mineral phase classification diagrams showing the composition of the main crystals of Predazzo camptonites. (**a**) Orthoclase (Or)-Albite (Ab)-Anorthite (An) ternary diagram for plagioclase and K-Feldspar; (**b**) Rutile (Rt)-Wustite (Wus)-Hematite (Hem) ternary diagram for Fe-Ti oxide; (**c**) Wollastonite (Wo)-Enstatite (En)-Ferrosilite (Fs) diagram for clinopyroxene (after Morimoto, 1988). (**d**) CaO/Na_2O vs. Al_2O_3/TiO_2 diagram for amphibole (after Rock, 1991). Compositional field of kaersutite in ultramafic (UML) and alkaline lamprophyres (AL), hastingsite in calc-alkaline lamprophyres (CAL), and K-richterite, arfvedsonite and eckermannite in lamproites (LL) are also reported in (**d**) for comparison (data from Rock, 1991).

Fig. 7. (colour online)

Photomicrographs in transmitted plane-polarized light, back scattered SEM images and core-to-rim compositional (Mg# and TiO_2) profiles of (**a**) *Type 1*, (**b**) *Type 2*, (**c**) *Type 3*, (**d**) *Type 4* and (**e**) *Type 5* amphiboles recognized in Predazzo camptonites. For each amphibole type, the determination of the water content (H_2O wt%) dissolved in the melt obtained by the equation

of Ridolfi *et al.* (2010) and the crystallization temperature (*T*°C) calculated by means of Putirka (2016) thermometer are also reported.

Fig. 8. (colour online)

Chondrite-normalized (Sun & McDonough, 1989) trace element (**a, c**) and REE (**b, d**) patterns of amphibole (Amp) and clinopyroxene (Cpx) crystals analysed in Predazzo camptonites. Solid lines: core composition; dotted lines: rim composition.

Fig. 9. (colour online)

Compositional and textural features of the carbonate ocelli inside Predazzo camptonites. (**a**) Calcite-magnesite-siderite ternary diagram and (**b**) SrO + MnO vs. CaO/MgO diagram (after Vichi *et al.*, 2005) showing the composition of carbonates from the inner and outer portions of the ocelli. Grey fields in (**a**) are referred to the composition of carbonates documented in worldwide lamprophyres (data from Rock, 1991). Dotted arrow in (**b**) represent the positive correlation between SrO + MnO and CaO/MgO, typical of low-temperature (low-*T*) carbonates (Vichi *et al.*, 2005). (**c, d, e**) Back scattered SEM images of carbonate ocelli composed of (**c, d**) both dolomite-ankerite/magnesite-siderite or (**e**) dolomite-ankerite crystals only. The flow-aligned tangential growth of amphibole, plagioclase and clinopyroxene is particularly evident in (**d**) and (**e**).

Fig. 10. (colour online)

$^{40}Ar/^{39}Ar$ age spectra for mineral separates from Predazzo camptonites, with apparent ages and K/Ca ratios spectra plotted against the cumulative percentage of ^{39}Ar released. (**a**) Age spectrum yielded by amphibole crystals from sample FF37; (**b**) age spectrum yielded by plagioclase crystals from sample FF2. Plateau ages are indicated in bold.

Fig. 11. (colour online)

$^{87}Sr/^{86}Sr$ vs. $^{143}Nd/^{144}Nd$ diagram showing the isotopic signature of Predazzo camptonites corrected to 220 Ma. Fields indicate the Sr-Nd isotopic signature of the: Finero (Voshage *et al.*, 1987), Balmuccia and Baldissero peridotites (Mukasa & Shervais 1999; Mazzucchelli *et al.*, 2009); alkaline dykes intruded in the Finero peridotite (220 Ma; Stahle *et al.*, 2001); apatite-rich layers of the Finero peridotite (215 Ma; Morishita *et al.*, 2008); Ditrau lamprophyres (220 Ma; Batki *et al.*, 2014); Predazzo Intrusive Complex (PIC) Shoshonitic Silica Saturated (SS) and Undersaturated (SU) rocks (234 Ma; Casetta *et al.*, 2018*a*). DMM (Workman & Hart, 2005) and EM I (Zindler & Hart, 1986) mantle end-members (corrected to 220 Ma) are also reported for comparison.

Fig. 12. (colour online)

(**a**) FeO vs. MgO and (**b**) Al_2O_3/TiO_2 vs. MgO diagrams showing the fractional crystallization (FC) vectors used to simulate the compositional trend of Predazzo camptonites. The dotted vectors represent the contribution of the single mineral phases during fractional crystallization; the black solid arrows represent the sum vector at 35% fractional crystallization. The relative percentages of fractionation of the single phases are also reported. Ol: olivine; Cpx: clinopyroxene; Amp: amphibole; Ti-Mag: Ti-magnetite; Pl: plagioclase.

Fig. 13. (colour online)

(**a**) Nb/La vs. La/Yb diagram (Smith *et al.*, 1999) used to discriminate between the contribution of lithosphere and asthenosphere in the mantle source of Predazzo camptonites. (**b**) Gd/Yb vs. La/Yb and (**c**) Sm/Yb vs. La/Sm diagrams for the less differentiated Predazzo camptonites. Melting curves in (**b**) and (**c**) are modelled using the non-modal batch melting equations of Shaw (1970). Starting mantle sources: I = Spl-lherzolite with DMM composition (Workman & Hart, 2005); II = Spl-lherzolite; III = Grt-lherzolite; IV = Spl-Grt-Amp-lherzolite; V = Grt-

Amp-lherzolite; VI = Grt-Phl-lherzolite. Starting REE composition of II, III, IV, V and VI sources is fertile PM of Sun & McDonough (1989). Source modal composition, melting proportions and partition coefficients for olivine, orthopyroxene, clinopyroxene, spinel, garnet, amphibole and phlogopite are reported in Table 9. (**d**) Chondrite-normalized (Sun & McDonough, 1989) REE patterns of Predazzo less differentiated camptonites compared to those simulated by partial melting of a garnet-amphibole-lherzolite (curve V) at partial melting degrees of 0.5 to 10%.

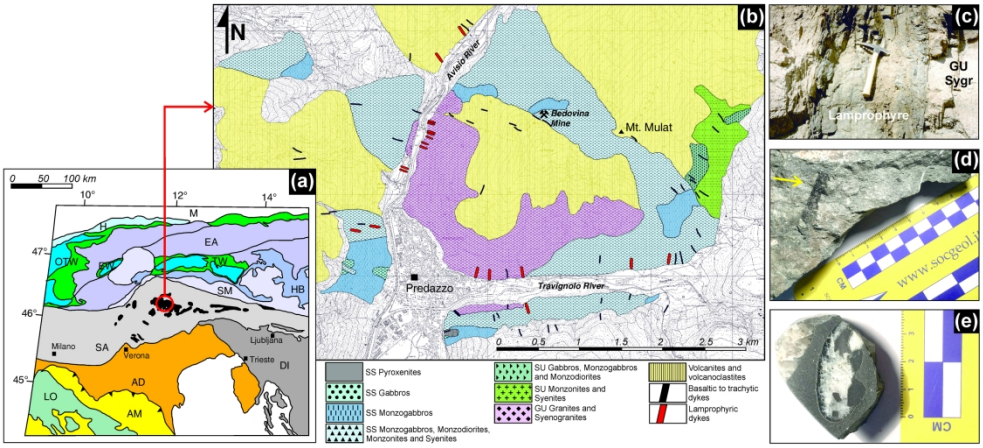

Fig. 1. (colour online)
(a) Map of the tectonic units of the eastern portion of the Alps (partly modified from Castellarin et al., 1988; Dal Piaz et al., 2003; Schmid et al., 2016). LO: Ligurian Ophiolites; AM: deformed Adriatic margin; AD: Adriatic Microplate; SA: Southern Alps; DI: Dinarides; SM: Southern margin of Meliata; HB: Eoalpine High-Pressure Belt; TW: Tauern tectonic Window; EW: Engadine tectonic Window; OTW: Ossola-Tessin tectonic Window; EA: Eastern Austroalpine; H: Helvetic domain; M: Molasse foredeep. The Middle Triassic magmatic occurrences in the Southern Alps domain are evidenced in black. They are, from west to east: Brescian Alps, Alto Vicentino, Valsugana, Dolomitic Area (identified by the circle), Carnia and Karawanken. (b) Simplified geological map of the Predazzo Intrusive Complex (PIC), showing the occurrence of lamprophyric dykes (modified from Casetta et al., 2018a). SS: Shoshonitic Silica Saturated unit; SU: Shoshonitic Silica Undersaturated unit; GU: Granitic Unit. (c) Lamprophyric dyke intruded in the syenogranites (Sygr) at Predazzo. (d) Amphibole megacryst (indicated by the arrow) and (e) clinopyroxenitic xenolith included in the lamprophyric rocks.

250x116mm (300 x 300 DPI)

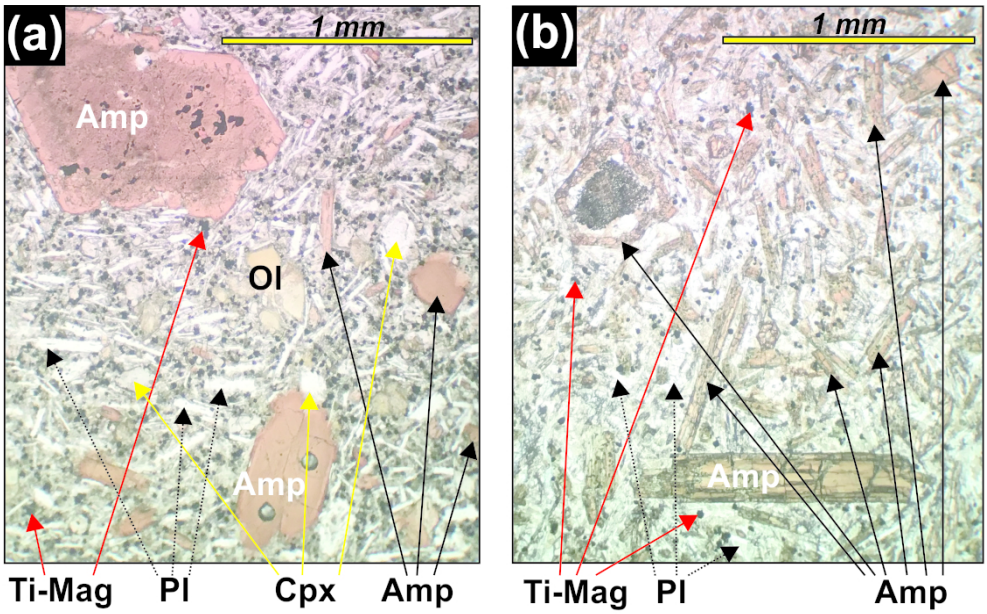

Fig. 2. (colour online)
Photomicrographs in transmitted plane-polarized light of (a) a less evolved and (b) a more evolved (sample MA1) camptonite. Amp: amphibole; Cpx: clinopyroxene; Ol: olivine; Pl: plagioclase; Ti-Mag: Ti-magnetite. Mineral abbreviations following Whitney & Evans (2010).

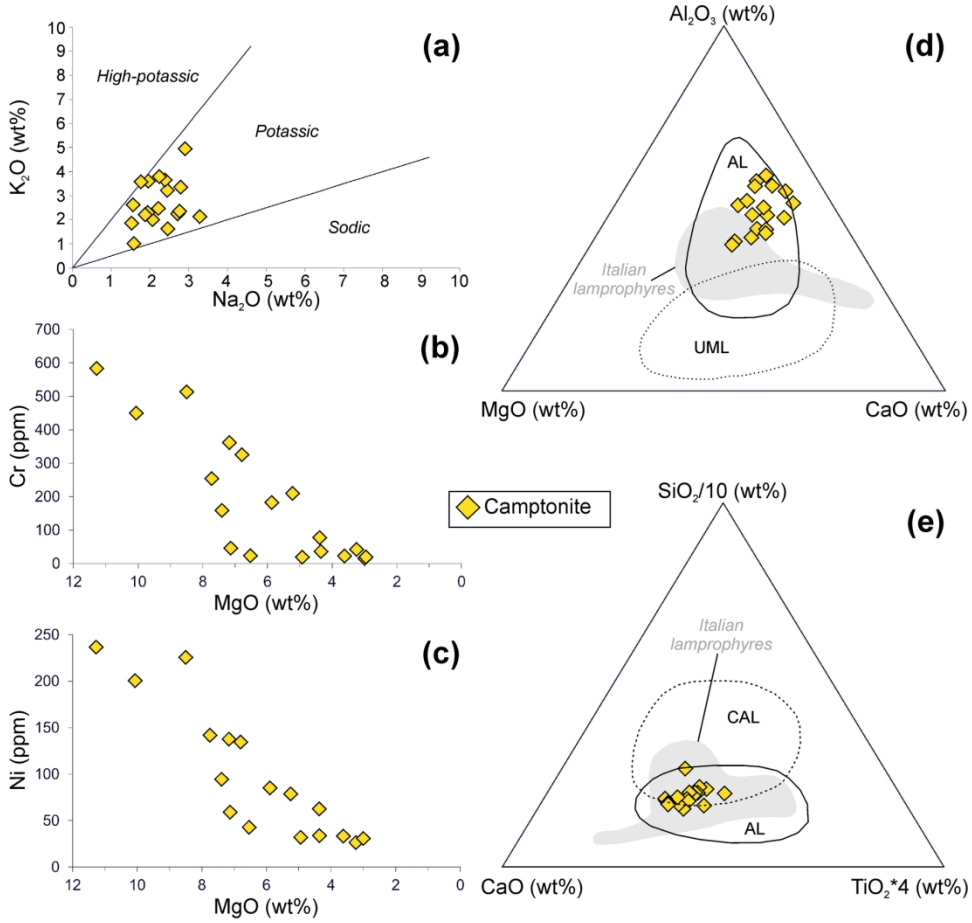

Fig. 3. (colour online)
(a) K2O vs. Na2O diagram, (b) Cr vs. MgO and (c) Ni vs. MgO variations diagrams for Predazzo camptonites. (d) Al2O3-MgO-CaO and (e) SiO2/10-CaO-TiO2×4 ternary diagrams showing the composition of Predazzo camptonites compared to those of worldwide alkaline lamprophyres (AL), ultramafic lamprophyres (UML) and calc-alkaline lamprophyres (CAL; data from Rock, 1991). The compositional field of Cretaceous to Oligocenic Italian lamprophyres (grey field) is also reported for comparison (data from Stoppa et al., 2014).

168x161mm (300 x 300 DPI)

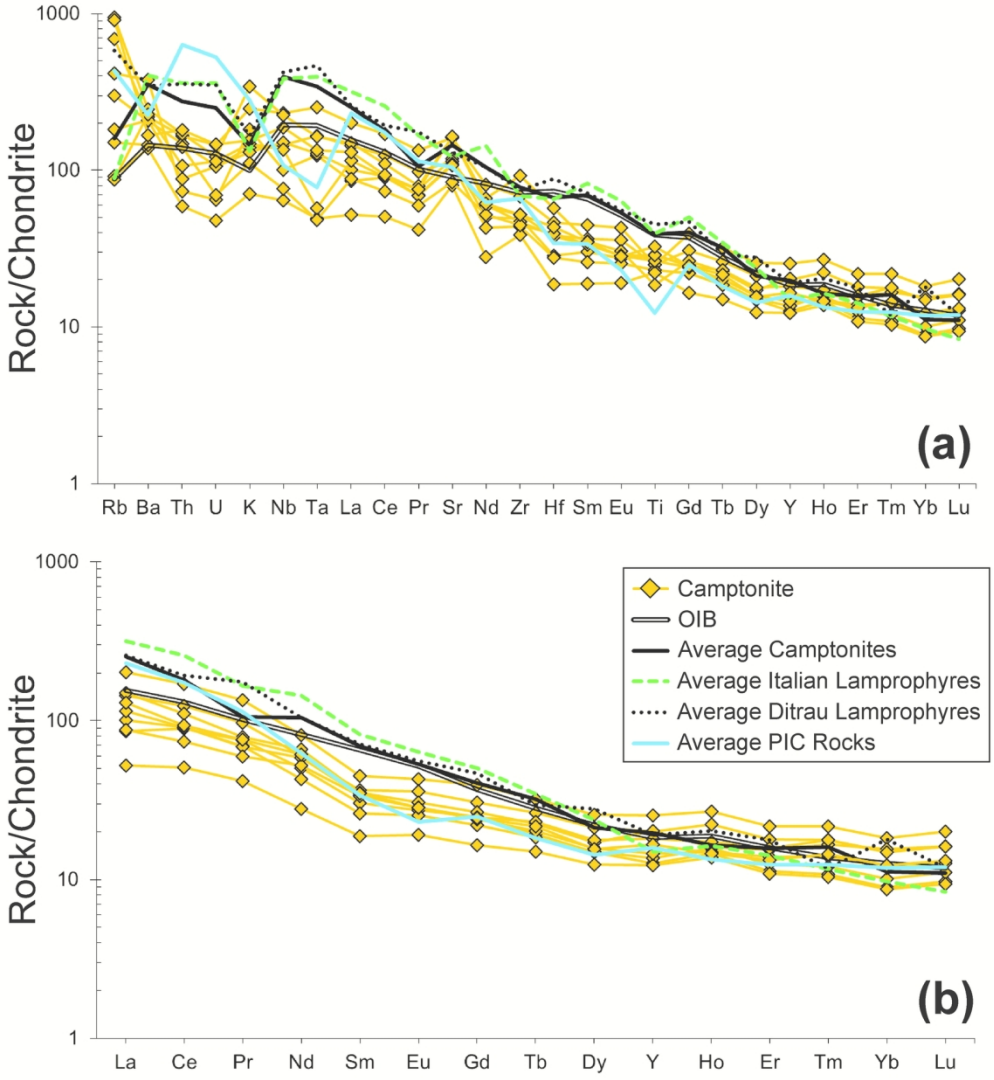

Fig. 4. (colour online)
Chondrite-normalized (Sun & McDonough, 1989) trace element (a) and REE patterns (b) of Predazzo camptonites. The OIB pattern (Sun & McDonough, 1989), the average composition of the worldwide camptonites (Rock, 1991), Italian lamprophyres (Galassi et al., 1994; Vichi et al., 2005; Stoppa et al., 2008; 2014), Ditrau lamprophyres (Batki et al., 2014) and Predazzo Intrusive Complex Shoshonitic Silica Saturated (SS) and Undersaturated (SU) rocks (Casetta et al., 2018a; 2018b) are reported for comparison.

154x170mm (300 x 300 DPI)

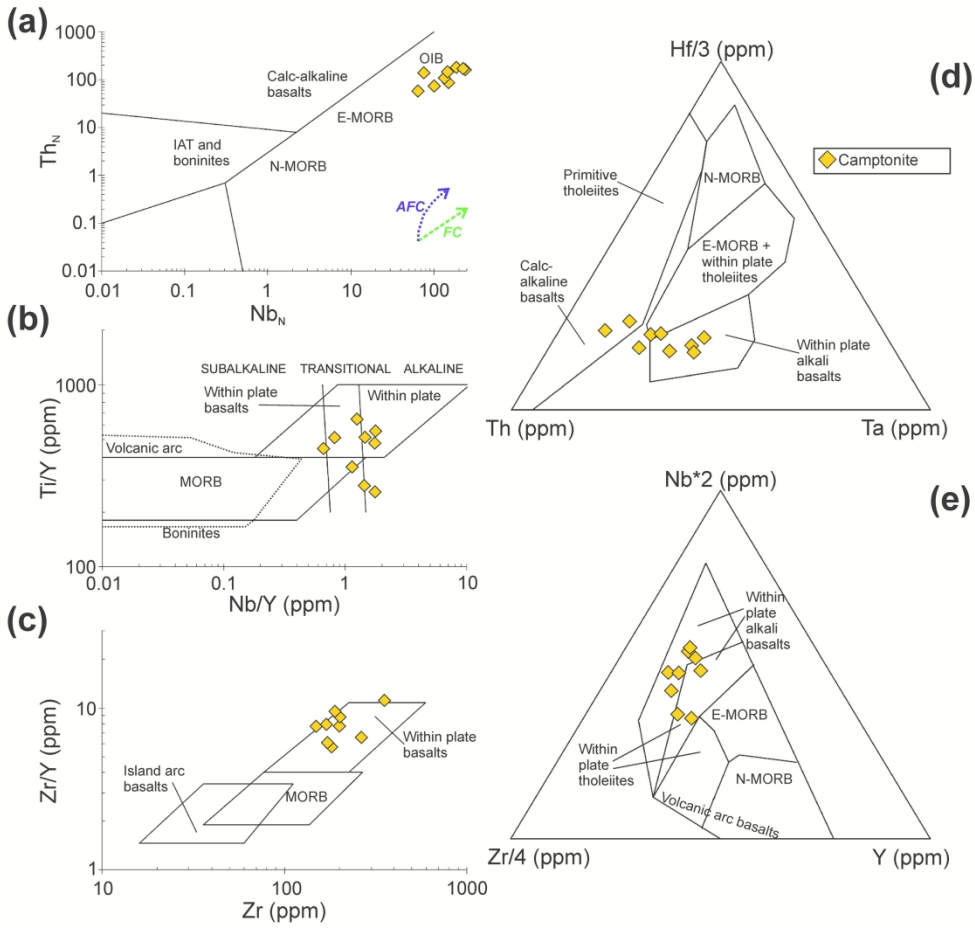

Fig. 5. (colour online)
Trace element discrimination diagrams for Predazzo camptonites: (a) ThN vs. NbN diagram (Saccani, 2015); (b) Ti/Y vs. Nb/Y diagram (Pearce, 1982); (c) Zr/Y vs. Zr diagram (Pearce and Norry, 1979); (d) Th-Hf-Ta ternary diagram (Wood, 1980); (e) Zr-Nb-Y ternary diagram (Meschede, 1986). Fractional Crystallization (FC) and Assimilation and Fractional Crystallization (AFC) vectors reported in (a) are in accordance with Saccani (2015).

225x210mm (300 x 300 DPI)

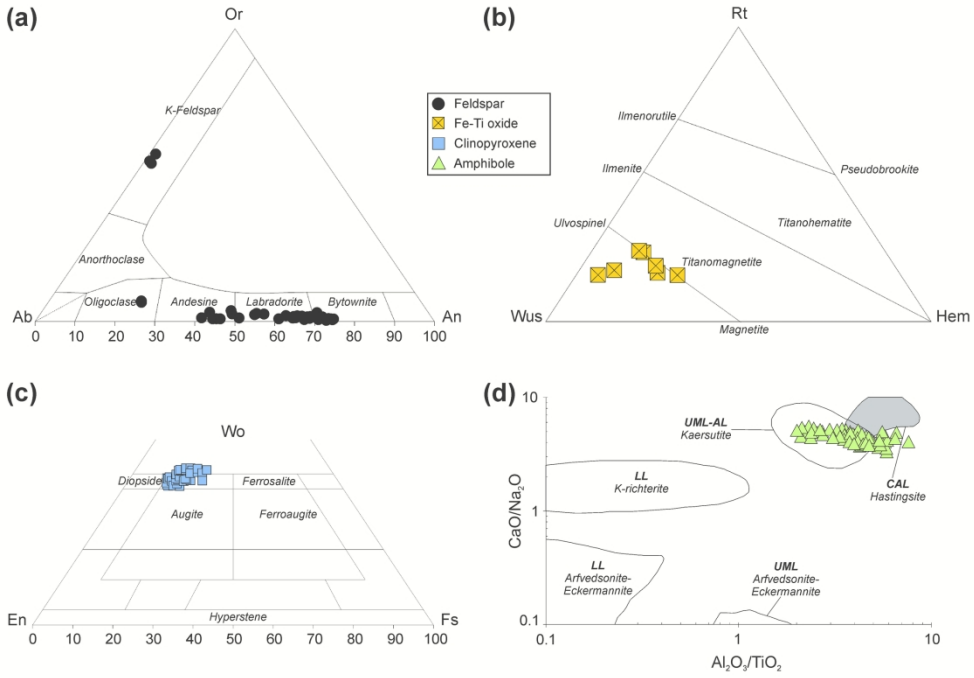

Fig. 6. (colour online)
Mineral phase classification diagrams showing the composition of the main crystals of Predazzo camptonites. (a) Orthoclase (Or)-Albite (Ab)-Anorthite (An) ternary diagram for plagioclase and K-Feldspar; (b) Rutile (Rt)-Wustite (Wus)-Hematite (Hem) ternary diagram for Fe-Ti oxide; (c) Wollastonite (Wo)-Enstatite (En)-Ferrosilite (Fs) diagram for clinopyroxene (after Morimoto, 1988). (d) CaO/Na2O vs. Al2O3/TiO2 diagram for amphibole (after Rock, 1991). Compositional field of kaersutite in ultramafic (UML) and alkaline lamprophyres (AL), hastingsite in calc-alkaline lamprophyres (CAL), and K-richterite, arfvedsonite and eckermannite in lamproites (LL) are also reported in (d) for comparison (data from Rock, 1991).

219x152mm (300 x 300 DPI)

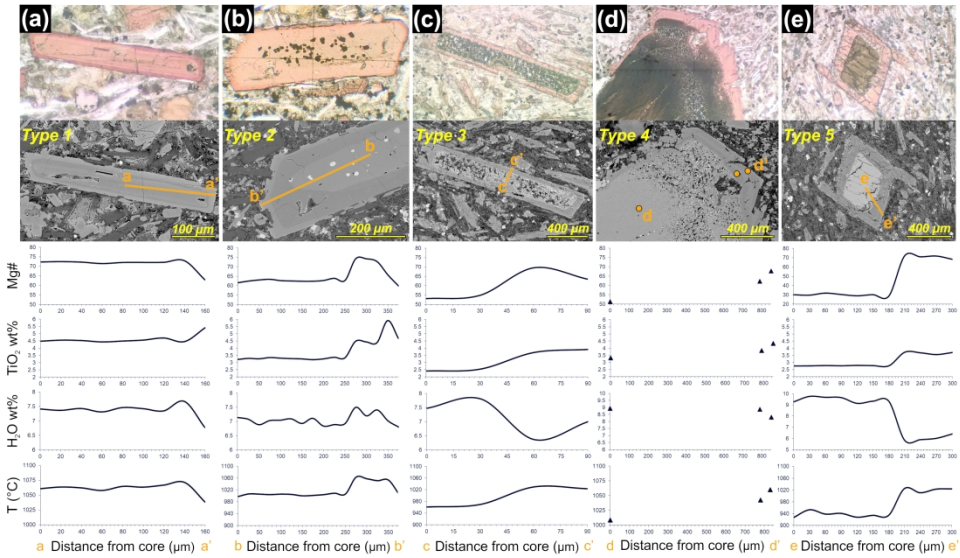

Fig. 7. (colour online)
Photomicrographs in transmitted plane-polarized light, back scattered SEM images and core-to-rim compositional (Mg# and TiO2) profiles of (a) Type 1, (b) Type 2, (c) Type 3, (d) Type 4 and (e) Type 5 amphiboles recognized in Predazzo camptonites. For each amphibole type, the determination of the water content (H2O wt%) dissolved in the melt obtained by the equation of Ridolfi et al. (2010) and the crystallization temperature (T°C) calculated by means of Putirka (2016) thermometer are also reported.

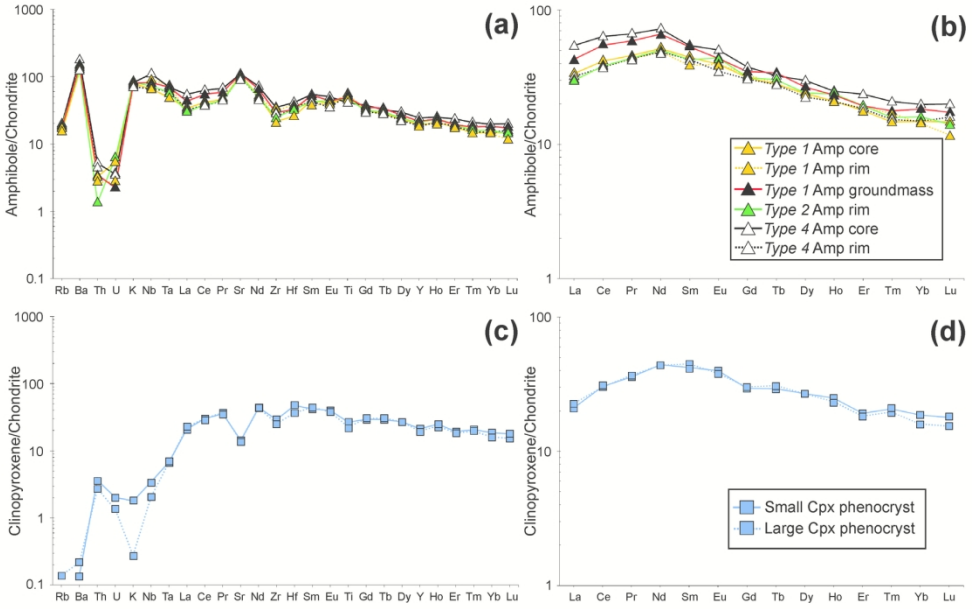

Fig. 8. (colour online)
Chondrite-normalized (Sun & McDonough, 1989) trace element (a, c) and REE (b, d) patterns of amphibole (Amp) and clinopyroxene (Cpx) crystals analysed in Predazzo camptonites. Solid lines: core composition; dotted lines: rim composition.

159x101mm (300 x 300 DPI)

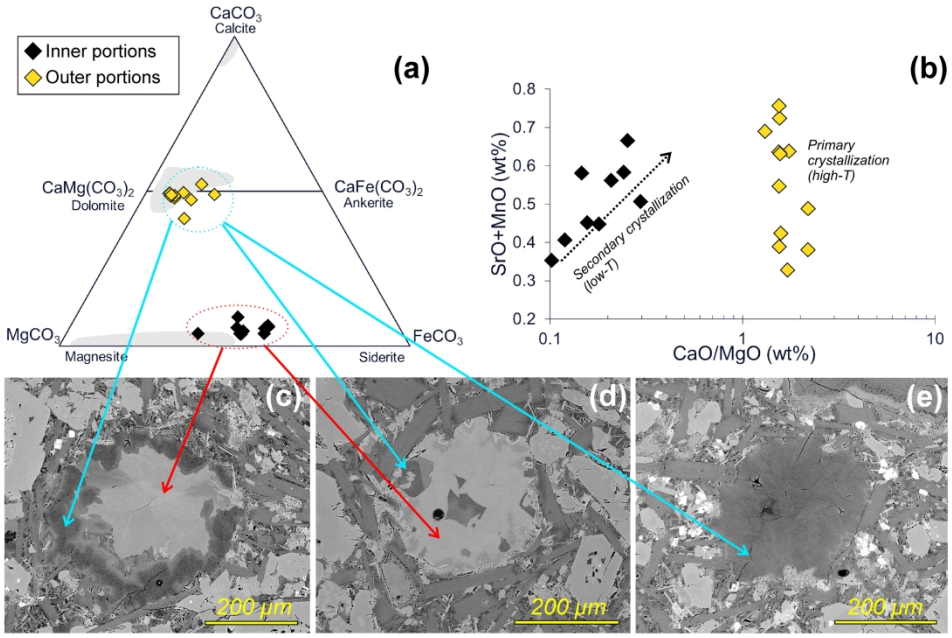

Fig. 9. (colour online)
Compositional and textural features of the carbonate ocelli inside Predazzo camptonites. (a) Calcite-magnesite-siderite ternary diagram and (b) SrO + MnO vs. CaO/MgO diagram (after Vichi et al., 2005) showing the composition of carbonates from the inner and outer portions of the ocelli. Grey fields in (a) are referred to the composition of carbonates documented in worldwide lamprophyres (data from Rock, 1991). Dotted arrow in (b) represent the positive correlation between SrO + MnO and CaO/MgO, typical of low-temperature (low-T) carbonates (Vichi et al., 2005). (c, d, e) Back scattered SEM images of carbonate ocelli composed of (c, d) both dolomite-ankerite/magnesite-siderite or (e) dolomite-ankerite crystals only. The flow-aligned tangential growth of amphibole, plagioclase and clinopyroxene is particularly evident in (d) and (e).

232x153mm (300 x 300 DPI)

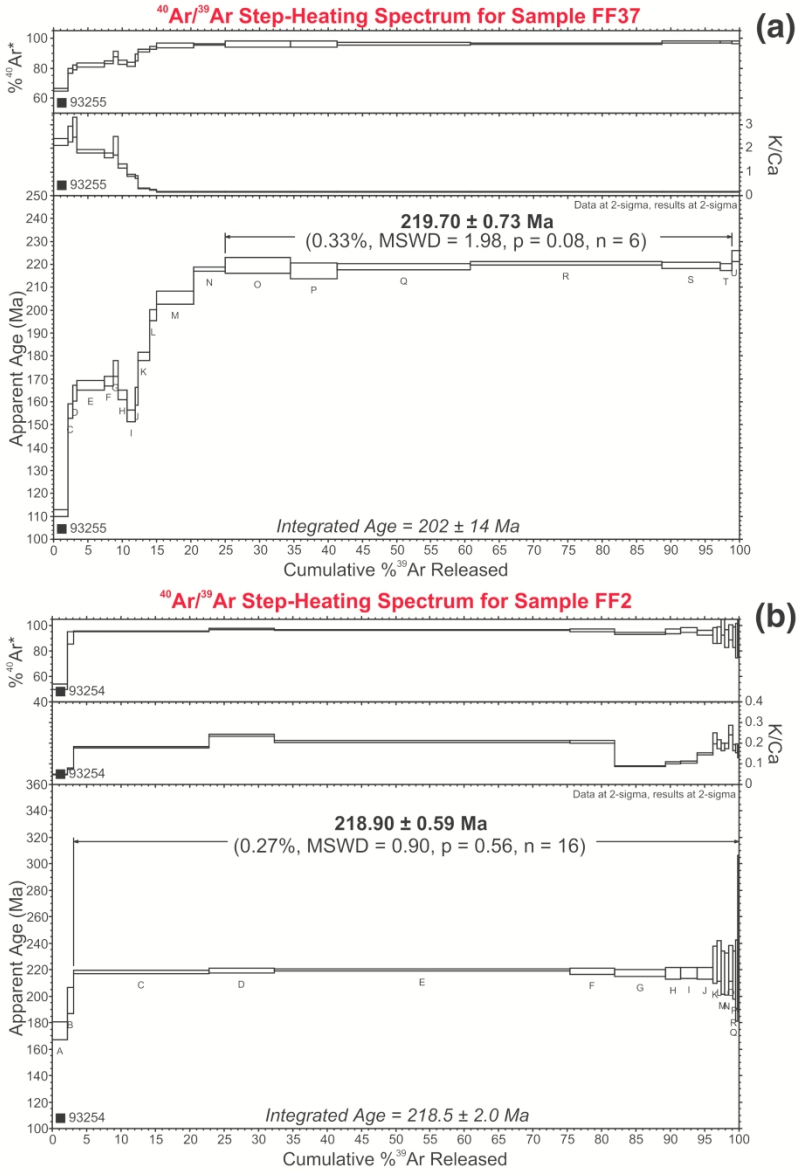

Fig. 10. (colour online)
40Ar/39Ar age spectra for mineral separates from Predazzo camptonites, with apparent ages and K/Ca ratios spectra plotted against the cumulative percentage of 39Ar released. (a) Age spectrum yielded by amphibole crystals from sample FF37; (b) age spectrum yielded by plagioclase crystals from sample FF2. Plateau ages are indicated in bold.

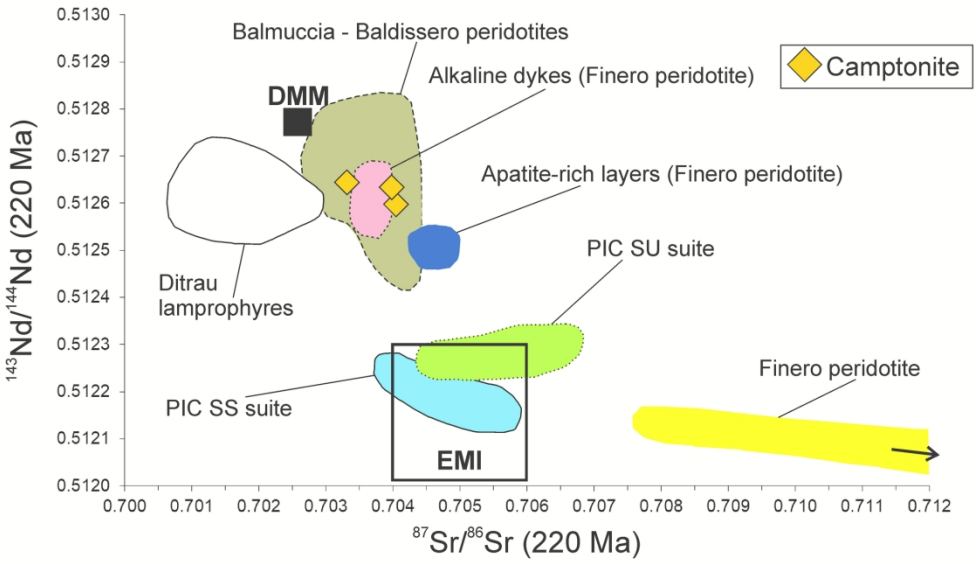

Fig. 11. (colour online)
87Sr/86Sr vs. 143Nd/144Nd diagram showing the isotopic signature of Predazzo camptonites corrected to 220 Ma. Fields indicate the Sr-Nd isotopic signature of the: Finero (Voshage et al., 1987), Balmuccia and Baldissero peridotites (Mukasa & Shervais 1999; Mazzucchelli et al., 2009); alkaline dykes intruded in the Finero peridotite (220 Ma; Stahle et al., 2001); apatite-rich layers of the Finero peridotite (215 Ma; Morishita et al., 2008); Ditrau lamprophyres (220 Ma; Batki et al., 2014); Predazzo Intrusive Complex (PIC) Shoshonitic Silica Saturated (SS) and Undersaturated (SU) rocks (234 Ma; Casetta et al., 2018a). DMM (Workman & Hart, 2005) and EM I (Zindler & Hart, 1986) mantle end-members (corrected to 220 Ma) are also reported for comparison.

188x114mm (300 x 300 DPI)

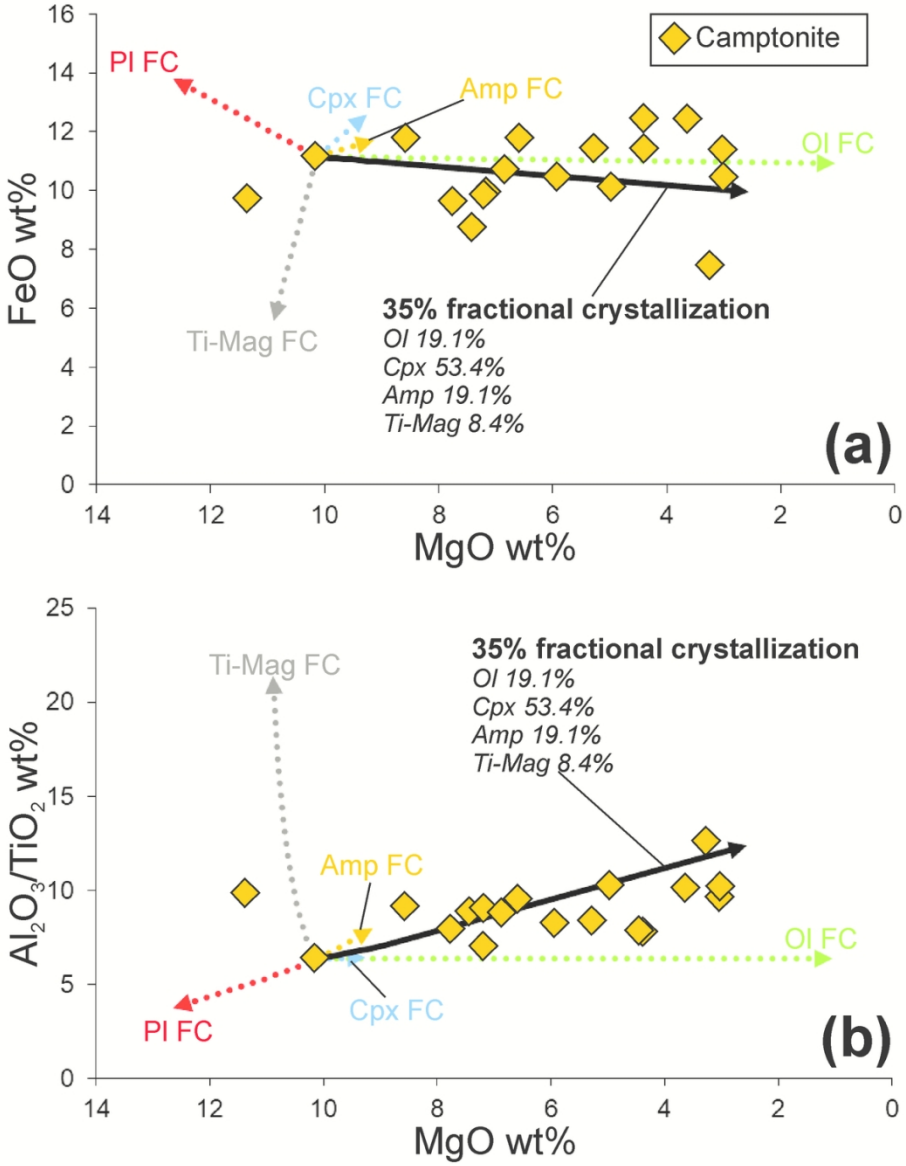

Fig. 12. (colour online)
(a) FeO vs. MgO and (b) Al2O3/TiO2 vs. MgO diagrams showing the fractional crystallization (FC) vectors used to simulate the compositional trend of Predazzo camptonites. The dotted vectors represent the contribution of the single mineral phases during fractional crystallization; the black solid arrows represent the sum vector at 35% fractional crystallization. The relative percentages of fractionation of the single phases are also reported. Ol: olivine; Cpx: clinopyroxene; Amp: amphibole; Ti-Mag: Ti-magnetite; Pl: plagioclase.

108x134mm (300 x 300 DPI)

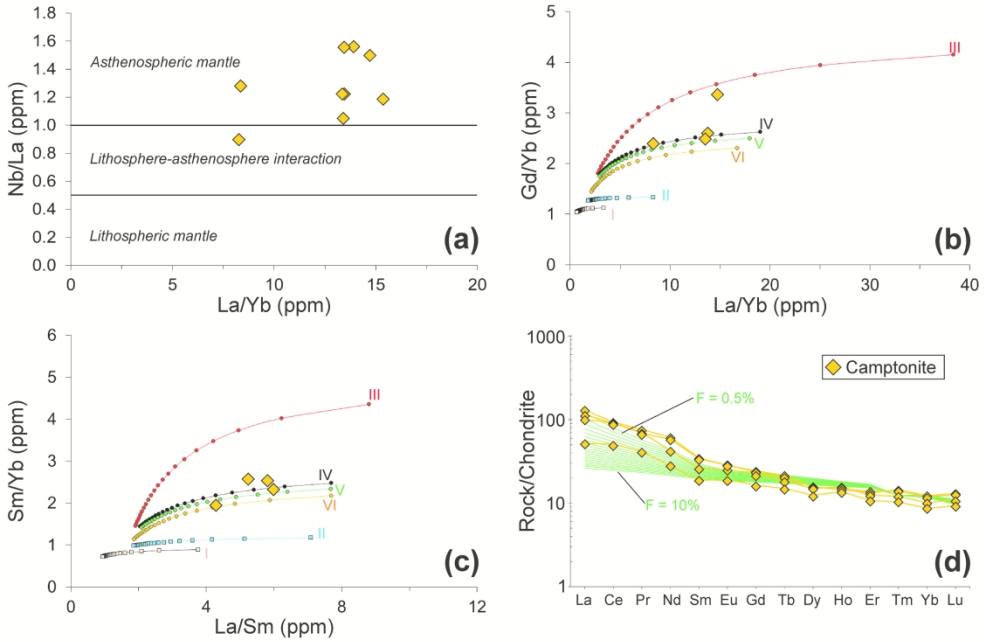

Fig. 13. (colour online)
(a) Nb/La vs. La/Yb diagram (Smith et al., 1999) used to discriminate between the contribution of lithosphere and asthenosphere in the mantle source of Predazzo camptonites. (b) Gd/Yb vs. La/Yb and (c) Sm/Yb vs. La/Sm diagrams for the less differentiated Predazzo camptonites. Melting curves in (b) and (c) are modelled using the non-modal batch melting equations of Shaw (1970). Starting mantle sources: I = Spl-lherzolite with DMM composition (Workman & Hart, 2005); II = Spl-lherzolite; III = Grt-lherzolite; IV = Spl-Grt-Amp-lherzolite; V = Grt-Amp-lherzolite; VI = Grt-Phl-lherzolite. Starting REE composition of II, III, IV, V and VI sources is fertile PM of Sun & McDonough (1989). Source modal composition, melting proportions and partition coefficients for olivine, orthopyroxene, clinopyroxene, spinel, garnet, amphibole and phlogopite are reported in Table 9. (d) Chondrite-normalized (Sun & McDonough, 1989) REE patterns of Predazzo less differentiated camptonites compared to those simulated by partial melting of a garnet-amphibole-lherzolite (curve V) at partial melting degrees of 0.5 to 10%.

239x161mm (300 x 300 DPI)

Table 1: Whole-rock major, trace element composition and $^{87}Sr/^{86}Sr$ and $^{143}Nd/^{144}Nd$ isotopes of Predazzo lamprophyres. Fe_2O_3 and FeO were calculated by considering a Fe_2O_3/ FeO ratio of 0.15, in agreement with a fO_2 around +1FMQ buffer (Kress & Carmichael, 1991). Mg# = MgO/[MgO+FeO] mol%; n.d. = not detected. All trace element (ppm) were analysed by ICP-MS except Pb, Zn, Ni, Co, Cr, V and Ba (XRF). The trace element composition of samples labelled with (*) was entirely determined by XRF. Sr-Nd isotopic ratios were corrected for 220 Ma of radiogenic ingrowth using the trace element abundances determined by ICP-MS, the decay rates of Rotenberg *et al.* (2012) and Lugmair & Marti (1978). Initial ratios (i) and uncertainties (2σ) were propagated according to Ickert (2013).
Camp: Camptonite

Lithology	Camp	Camp	Camp	Camp	Camp	Camp	Camp	Camp	Camp	Camp	Camp	Camp	Camp	Camp	Camp	Camp	Camp
Sample	**222***	**A 71***	**FF2***	**FF17***	**FF22***	**FF26***	**S3***	**FF37***	**FF38***	**EM97**	**EM99**	**FF14**	**EM20A**	**EM87**	**EM37A**	**FC80**	**MA5**	**MA1**
Oxide (wt%)																		
SiO_2	47.22	47.90	45.00	44.29	45.02	46.20	47.72	45.86	45.63	45.74	47.00	44.07	45.24	44.59	44.73	45.16	46.67	52.81
TiO_2	2.00	1.83	1.87	2.13	2.31	2.30	2.00	1.82	1.91	2.14	1.85	2.41	1.84	1.71	1.65	1.96	2.13	1.37
Al_2O_3	16.74	18.82	17.97	17.01	16.23	18.15	17.77	18.46	18.36	17.62	18.78	15.29	16.39	15.75	16.25	17.74	16.65	17.45
Fe_2O_3	1.50	1.33	1.49	1.26	1.30	1.63	1.15	1.63	1.55	1.37	1.37	1.46	1.41	1.55	1.29	1.31	1.50	0.98
FeO	9.99	8.83	9.91	8.45	8.65	10.86	7.65	10.83	10.32	9.15	9.10	9.74	9.38	10.30	8.54	8.71	10.02	6.53
MnO	0.23	0.19	0.23	0.19	0.23	0.17	0.18	0.18	0.15	0.20	0.20	0.18	0.22	0.20	0.20	0.18	0.17	0.16
MgO	5.24	4.93	2.99	7.72	7.15	4.36	7.39	3.60	6.53	5.88	3.00	10.06	6.80	8.49	11.28	7.13	4.37	3.23
CaO	11.25	9.71	13.88	13.43	14.24	9.05	9.66	10.73	10.26	13.03	12.49	11.92	13.81	13.21	12.86	11.80	13.95	8.83
Na_2O	2.77	1.95	2.45	2.73	1.92	2.81	2.40	2.23	2.20	1.56	1.75	1.89	2.08	1.54	1.59	3.27	2.47	2.90
K_2O	2.38	3.61	3.25	2.27	2.29	3.37	3.66	3.74	2.48	2.64	3.58	2.25	2.01	1.89	1.02	2.14	1.61	4.97
P_2O_5	0.68	0.90	0.95	0.51	0.65	1.10	0.43	0.92	0.60	0.65	0.86	0.73	0.81	0.78	0.60	0.60	0.44	0.77
Tot.	100.00	100.00	100.00	100.00	100.00	100.00	100.00	100.00	100.00	100.00	100.00	100.00	100.00	100.00	100.00	100.00	100.00	100.00
Mg#	48.30	49.90	34.97	61.94	59.58	41.68	63.24	37.20	52.99	53.41	36.96	64.77	56.34	59.52	70.19	59.33	43.75	46.88
LOI	6.65	3.72	6.39	4.92	5.41	5.88	5.52	5.53	4.81	5.33	6.53	5.70	6.11	5.13	6.68	5.17	7.36	5.94
Trace element (ppm)																		
Pb	28.0	8.20	12.0	13.0	10.0	11.0	15.4	26.0	13.7	5.60	22.2	11.0	12.2	15.8	21.4	16.0	34.0	8.7
Zn	128	79.5	69.0	65.0	79.0	119	143	124	216	110	122	97.0	90.1	88.0	107	80.7	145	77.9
Ni	79.0	31.8	31.0	143	138	34.0	94.5	33.0	43.3	85.5	30.9	201	135	226	237	59.4	62.8	27.3
Co	30.0	28.8	28.0	40.0	43.0	26.0	32.7	34.0	43.0	30.3	34.5	45.0	32.4	44.4	48.4	40.6	41.6	25.8
Cr	211	19.8	14.0	254	364	37.0	161	23.0	24.9	185	16.0	449	326	514	585	46.8	78.9	42.2
V	144	112	124	238	231	134	197	130	187	222	125	220	167	170	212	191	223	92.8
Rb	52.0	82.8	239	114	48.0	105	102	238	54.0	146	242	318	105	63.9	32.0	30.5	52.7	331
Ba	535	790	528	542	510	571	991	522	576	910	525	405	496	504	334	546	350	590
Sr	1187	1305	1247	661	807	1545	1085	1183	1069	862	1175	1190	829	795	581	780	609	1181
Nb	45.0	58.4	60.0	16.0	30.0	72.0	n.d.	63.0	n.d.	24.9	56.9	46.2	35.8	37.2	15.8	33.3	18.8	55.2
Zr	187	321	309	211	241	251	262	333	212	190	264	201	182	170	150	202	173	356
Hf										3.03	4.96	4.62	4.08	2.95	1.99	4.02	4.19	6.11
U										0.52	1.16	1.18	0.86	0.85	0.38	0.91	0.56	0.98
Th										2.13	4.83	5.26	4.29	2.55	1.71	3.10	4.09	4.96
Y	22.0	31.6	25.0	24.0	23.0	26.0	33.3	27.0	30.3	19.9	39.8	26.0	31.4	21.5	19.4	22.8	28.5	31.9
Ta										1.74	3.53	1.88	2.32	1.80	0.69	0.80	0.68	2.30
La	45.0	71.5	38.0	11.0	27.0	61.0	55.9	37.0	48.4	20.4	47.7	30.9	34.0	23.8	12.3	27.2	20.8	35.4
Ce	79.0	121	125	64.0	42.0	109	93.8	86.0	49.5	54.8	105	57.2	76.2	55.9	31.1	55.6	45.1	67.5
Pr										7.17	12.8	7.21	9.27	6.61	3.96	6.53	5.65	7.51
Nd										23.4	37.8	28.7	28.1	20.0	13.0	27.2	24.3	31.0
Sm										4.62	6.86	5.32	5.58	3.98	2.88	5.19	5.13	5.37
Eu										1.58	2.50	1.64	2.08	1.48	1.11	1.65	1.65	1.77
Gd										5.10	8.08	5.01	6.29	4.54	3.39	4.92	5.05	5.45
Tb										0.72	1.20	0.81	0.98	0.69	0.56	0.76	0.86	0.84
Dy										3.76	6.53	3.96	5.39	3.81	3.16	3.99	4.53	4.34
Ho										0.82	1.52	0.83	1.26	0.89	0.78	0.84	0.98	0.91
Er										1.88	3.59	2.20	2.97	2.07	1.80	2.31	2.61	2.55
Tm										0.28	0.55	0.37	0.45	0.31	0.26	0.36	0.45	0.43
Yb										1.52	3.10	2.09	2.54	1.71	1.48	2.02	2.52	2.64
Lu										0.25	0.51	0.33	0.41	0.28	0.24	0.32	0.41	0.41
$^{87}Sr/^{86}Sr$												0.706376				0.704373		0.705787
$^{87}Rb/^{86}Sr$												0.7733				0.1129		0.8098
$^{87}Sr/^{86}Sr_{(i)}$												0.703996				0.704025		0.703295
2σ												0.000031				0.000020		0.000030
$^{143}Nd/^{144}Nd$												0.512795				0.512765		0.512796
$^{147}Sm/^{144}Nd$												0.1118				0.1152		0.1047
$^{143}Nd/^{144}Nd_{(i)}$												0.512634				0.512599		0.512645
2σ												0.000006				0.000006		0.000007

Table 2: Major element core to rim analyses and a.p.f.u. calculation of representative amphibole types from Predazzo lamprophyres. A.p.f.u. were calculated using the Lockock (2014) computation; the classification follows the recommendations of the IMA-CNMNC subcommittee on amphiboles (Hawthorne *et al.*, 2012; Oberti *et al.*, 2012). Mg# = Mg/[Mg+Fe] mol%, assuming all Fe as Fe^{2+}

Sample	FC80 - Camptonite									FC80 – Camptonite															
Amphibole type	*Type 1*									*Type 2*															
Name	Am1_c	Am1_tr1	Am1_tr2	Am1_tr3	Am1_tr4	Am1_tr5	Am1_tr6	Am1_tr7	Am1_r	Am4_c	Am4_tr1	Am4_tr2	Am4_tr3	Am4_tr4	Am4_tr5	Am4_tr6	Am4_tr7	Am4_tr8	Am4_tr9	Am4_tr10	Am4_tr11	Am4_tr12	Am4_tr13	Am4_tr14	Am4_r
Oxyde (wt%)																									
SiO_2	39.456	39.460	39.315	39.213	39.224	39.412	39.345	38.865	39.353	39.687	39.567	39.625	39.816	39.634	39.599	39.801	39.721	39.715	39.835	39.503	39.735	39.958	40.207	39.575	40.113
TiO_2	4.475	4.548	4.522	4.426	4.487	4.553	4.696	4.450	5.407	3.208	3.285	3.254	3.343	3.300	3.269	3.248	3.195	3.249	3.362	3.320	4.475	4.431	4.384	5.920	4.671
Al_2O_3	15.137	15.130	15.154	15.117	15.197	15.145	15.034	15.553	12.907	14.502	14.608	14.513	14.422	14.436	14.522	14.435	14.547	14.532	14.488	14.456	15.007	14.708	14.618	13.098	12.745
Cr_2O_3	0.097	0.081	0.087	0.076	0.073	0.068	0.080	0.121	0.007	0.000	0.009	0.001	0.000	0.000	0.002	0.001	0.000	0.002	0.000	0.000	0.129	0.120	0.016	0.012	0.000
FeO_{TOT}	9.284	9.253	9.265	9.664	9.351	9.382	9.334	8.918	12.204	13.256	12.909	12.811	12.658	12.748	12.854	13.007	12.910	12.864	12.407	12.899	8.558	8.650	9.197	11.280	13.322
MnO	0.097	0.081	0.136	0.101	0.096	0.084	0.096	0.125	0.196	0.159	0.169	0.136	0.126	0.137	0.154	0.109	0.178	0.164	0.156	0.159	0.096	0.091	0.116	0.148	0.241
MgO	13.584	13.675	13.509	13.571	13.512	13.570	13.542	13.502	11.614	11.909	12.036	12.258	12.291	12.007	12.016	12.078	11.991	12.153	12.317	12.191	13.842	13.973	13.753	12.134	11.133
CaO	11.901	11.897	11.745	11.572	11.933	11.770	11.927	11.963	11.900	11.360	11.429	11.461	11.459	11.448	11.441	11.544	11.481	11.347	11.473	11.542	12.205	12.128	12.027	12.359	11.833
Na_2O	2.456	2.482	2.452	2.437	2.502	2.516	2.514	2.448	2.577	2.549	2.612	2.591	2.548	2.637	2.605	2.551	2.583	2.607	2.609	2.544	2.430	2.434	2.529	2.433	2.570
K_2O	1.164	1.142	1.162	1.115	1.147	1.119	1.135	1.182	1.053	1.180	1.192	1.206	1.165	1.189	1.185	1.246	1.208	1.249	1.231	1.199	1.148	1.157	1.026	1.045	1.105
NiO	0.003	0.011	0.004	0.000	0.015	0.000	0.046	0.034	0.000	0.004	0.000	0.037	0.015	0.004	0.000	0.004	0.000	0.008	0.031	0.000	0.014	0.020	0.057	0.000	0.000
F	0.339	0.265	0.178	0.360	0.290	0.270	0.379	0.327	0.585	0.110	0.281	0.263	0.221	0.275	0.238	0.237	0.083	0.209	0.185	0.226	0.263	0.337	0.295	0.476	0.579
Cl	0.000	0.028	0.000	0.041	0.000	0.030	0.066	0.020	0.036	0.047	0.000	0.000	0.074	0.031	0.000	0.013	0.026	0.000	0.053	0.000	0.000	0.036	0.000	0.049	0.000
Tot.	97.993	98.054	97.529	97.694	97.826	97.919	98.194	97.508	97.837	97.970	98.097	98.155	98.137	97.846	97.885	98.274	97.923	98.098	98.149	98.039	97.905	98.042	98.225	98.528	98.310
Mg#	**72.3**	**72.5**	**72.2**	**71.4**	**72.0**	**72.0**	**72.1**	**73.0**	**62.9**	**61.6**	**62.4**	**63.0**	**63.4**	**62.7**	**62.5**	**62.3**	**62.3**	**62.7**	**63.9**	**62.7**	**74.2**	**74.2**	**72.7**	**65.7**	**59.8**
$Fe^{3+}/\Sigma Fe$ used	0.904	0.91	0.903	0.904	0.909	0.898	0.912	0.926	0.618	0.574	0.58	0.605	0.605	0.549	0.567	0.562	0.554	0.581	0.584	0.615	0.916	0.913	0.814	0.713	0.478
Group	OH,F,Cl	oxo	oxo	OH,F,Cl	OH,F,Cl	oxo	oxo	OH,F,Cl	oxo	OH,F,Cl	OH,F,Cl	OH,F,Cl	OH,F,Cl	OH,F,Cl	OH,F,Cl	OH,F,Cl	OH,F,Cl	OH,F,Cl	OH,F,Cl	OH,F,Cl	OH,F,Cl	OH,F,Cl	OH,F,Cl	OH,F,Cl	oxo	oxo
Subgroup of (OH,F,Cl)	Ca	B = Ca	B = Ca	Ca	Ca	B = Ca	B = Ca	Ca	B = Ca	Ca	Ca	Ca	Ca	Ca	Ca	Ca	Ca	Ca	Ca	Ca	Ca	Ca	Ca	Ca	B = Ca	B = Ca
Species	magnesio-hastingsite	ferri-kaersutite	ferri-kaersutite	magnesio-hastingsite	magnesio-hastingsite	ferri-kaersutite	ferri-kaersutite	magnesio-hastingsite	ferri-kaersutite	Ti-rich magnesio-hastingsite	Ti-rich magnesio-hastingsite	Ti-rich magnesio-hastingsite	Ti-rich magnesio-hastingsite	Ti-rich magnesio-hastingsite	Ti-rich magnesio-hastingsite	Ti-rich magnesio-hastingsite	Ti-rich magnesio-hastingsite	Ti-rich magnesio-hastingsite	Ti-rich magnesio-hastingsite	Ti-rich magnesio-hastingsite	Ti-rich magnesio-hastingsite	magnesio-hastingsite	magnesio-hastingsite	magnesio-hastingsite	ferri-kaersutite	ferri-kaersutite
Formula Assignments																									
(T) Si	5.794	5.789	5.792	5.778	5.771	5.791	5.782	5.736	5.941	5.89	5.872	5.869	5.894	5.902	5.887	5.897	5.896	5.886	5.898	5.859	5.827	5.856	5.889	5.909	6.04
(T) Al	2.206	2.211	2.208	2.222	2.229	2.209	2.218	2.264	2.059	2.11	2.128	2.131	2.106	2.098	2.113	2.103	2.104	2.114	2.102	2.141	2.173	2.144	2.111	2.091	1.96
(T) Ti	0	0	0	0	0	0	0	0	0	0	0	0	0	0	0	0	0	0	0	0	0	0	0	0	0
(C) Ti	0.494	0.502	0.501	0.491	0.497	0.503	0.519	0.494	0.614	0.358	0.367	0.363	0.372	0.37	0.366	0.362	0.357	0.362	0.375	0.371	0.494	0.488	0.483	0.665	0.529
(C) Al	0.413	0.405	0.423	0.403	0.406	0.414	0.386	0.442	0.237	0.427	0.427	0.402	0.411	0.435	0.431	0.418	0.441	0.424	0.426	0.386	0.42	0.396	0.412	0.213	0.302
(C) Cr	0.011	0.009	0.01	0.009	0.008	0.008	0.009	0.014	0.001	0	0.001	0	0	0	0	0	0	0	0	0	0.015	0.014	0.002	0.001	0
(C) Fe^{3+}	1.03	1.033	1.031	1.076	1.046	1.035	1.047	1.019	0.952	0.944	0.929	0.961	0.949	0.871	0.906	0.906	0.888	0.926	0.897	0.984	0.961	0.968	0.917	1.005	0.802
(C) Ni	0	0.001	0.001	0	0.002	0	0.005	0.004	0	0	0	0.004	0.002	0.001	0	0	0	0.001	0.004	0	0.002	0.002	0.007	0	0
(C) Mn^{2+}	0	0	0	0	0	0	0	0	0	0	0	0	0	0	0	0	0	0	0	0	0	0	0	0.011	0
(C) Fe^{2+}	0.077	0.06	0.068	0.04	0.078	0.068	0.067	0.056	0.583	0.636	0.614	0.563	0.554	0.658	0.634	0.646	0.661	0.601	0.58	0.564	0.082	0.078	0.176	0.404	0.868
(C) Mg	2.974	2.991	2.967	2.981	2.964	2.972	2.967	2.971	2.614	2.635	2.663	2.707	2.713	2.666	2.663	2.668	2.653	2.685	2.719	2.696	3.026	3.053	3.003	2.701	2.499
(B) Mn^{2+}	0.012	0.01	0.017	0.013	0.012	0.01	0.012	0.016	0.025	0.02	0.021	0.017	0.016	0.017	0.019	0.014	0.022	0.021	0.02	0.02	0.012	0.011	0.014	0.007	0.031
(B) Fe^{2+}	0.033	0.043	0.043	0.075	0.027	0.05	0.034	0.026	0.007	0.065	0.059	0.063	0.064	0.059	0.059	0.06	0.054	0.067	0.059	0.052	0.006	0.014	0.033	0	0.008
(B) Ca	1.872	1.87	1.854	1.827	1.881	1.853	1.878	1.892	1.925	1.806	1.817	1.819	1.818	1.827	1.822	1.833	1.826	1.802	1.82	1.834	1.918	1.904	1.887	1.977	1.909
(B) Na	0.083	0.077	0.087	0.086	0.08	0.087	0.076	0.067	0.043	0.108	0.102	0.102	0.102	0.097	0.1	0.094	0.098	0.111	0.101	0.093	0.064	0.071	0.065	0.015	0.053
(A) Ca	0	0	0	0	0	0	0	0	0	0	0	0	0	0	0	0	0	0	0	0	0	0	0	0	0
(A) Na	0.617	0.629	0.614	0.611	0.634	0.63	0.64	0.634	0.711	0.625	0.649	0.643	0.629	0.664	0.651	0.639	0.645	0.639	0.648	0.638	0.627	0.621	0.653	0.689	0.698
(A) K	0.218	0.214	0.218	0.21	0.215	0.21	0.213	0.223	0.203	0.223	0.226	0.228	0.22	0.226	0.225	0.235	0.229	0.236	0.232	0.227	0.215	0.216	0.192	0.199	0.212
O (non-W)	22	22	22	22	22	22	22	22	22	22	22	22	22	22	22	22	22	22	22	22	22	22	22	22	22
(W) OH	0.853	0.865	0.914	0.84	0.871	0.86	0.768	0.853	0.483	1.219	1.134	1.151	1.133	1.123	1.156	1.161	1.24	1.177	1.151	1.152	0.89	0.858	0.897	0.433	0.666
(W) F	0.157	0.123	0.083	0.168	0.135	0.125	0.176	0.153	0.279	0.052	0.132	0.123	0.103	0.13	0.112	0.111	0.039	0.098	0.086	0.106	0.122	0.156	0.137	0.225	0.275
(W) Cl	0	0.007	0	0.01	0	0.008	0.016	0.005	0.009	0.012	0	0	0.019	0.008	0	0.003	0.006	0	0.013	0	0	0.009	0	0.012	0
(W) O	0.99	1.005	1.003	0.982	0.994	1.007	1.039	0.989	1.229	0.717	0.734	0.726	0.745	0.74	0.732	0.725	0.714	0.725	0.75	0.742	0.988	0.978	0.967	1.33	1.059
Sum (T,C,B,A)	15.834	15.844	15.834	15.822	15.85	15.84	15.853	15.858	15.915	15.847	15.875	15.872	15.85	15.891	15.876	15.875	15.874	15.875	15.881	15.865	15.842	15.836	15.844	15.887	15.911

Table 2: (continued)

Sample	MA1 - Camptonite				FC80 - Camptonite			MA1 – Camptonite										
Amphibole type	*Type 3*				*Type 4*			*Type 5*										
Name	Am2_c	Am2_tr1	Am2_tr2	Am2_r	Am3_c	Am3_tr1	Am3_r	Am5_c	Am5_tr1	Am5_tr2	Am5_tr3	Am5_tr4	Am5_tr5	Am5_tr6	Am5_tr7	Am5_tr8	Am5_tr9	Am5_r
Oxyde (wt%)																		
SiO_2	39.088	38.649	39.990	39.134	37.475	37.671	38.310	37.416	37.227	38.800	37.863	36.037	36.968	36.020	40.965	41.475	40.666	40.164
TiO_2	2.405	2.533	3.694	3.908	3.312	3.837	4.336	2.757	2.765	2.787	2.771	2.798	2.782	2.775	3.727	3.681	3.561	3.706
Al_2O_3	13.833	14.093	14.308	13.688	15.537	15.957	15.546	15.375	16.316	16.200	16.158	14.846	15.421	14.974	13.539	13.258	13.611	13.514
Cr_2O_3	0.004	0.000	0.029	0.024	0.000	0.021	0.000	0.009	0.011	0.001	0.000	0.000	0.010	0.003	0.093	0.055	0.059	0.008
FeO_{TOT}	15.794	15.274	10.384	12.324	15.449	12.154	10.548	22.091	22.060	21.710	22.044	22.038	21.979	21.989	9.648	10.186	9.729	10.834
MnO	0.399	0.351	0.134	0.174	0.193	0.139	0.115	0.420	0.426	0.415	0.423	0.442	0.400	0.425	0.168	0.156	0.125	0.153
MgO	10.018	10.383	13.287	11.999	9.137	11.240	12.446	5.341	5.217	5.696	5.397	5.033	5.324	4.949	14.000	13.977	13.894	13.101
CaO	11.721	11.951	11.602	11.791	11.771	12.079	11.779	10.377	10.230	10.279	10.283	10.387	10.395	10.341	11.427	11.238	11.426	11.877
Na_2O	2.660	2.466	2.610	2.735	2.730	2.417	2.513	2.682	3.145	2.994	2.950	2.548	2.732	2.720	2.703	2.647	2.687	2.762
K_2O	1.132	1.073	1.297	0.994	1.182	1.130	1.024	1.396	1.320	1.351	1.364	1.372	1.357	1.316	1.189	1.127	1.153	1.071
NiO	0.000	0.016	0.000	0.026				0.007	0.000	0.017	0.018	0.012	0.000	0.000	0.046	0.038	0.009	0.014
F	0.243	0.304	0.203	0.254	0.111	0.138	0.180	0.199	0.028	0.093	0.064	0.085	0.112	0.112	0.267	0.270	0.178	0.384
Cl	0.034	0.077	0.000	0.010	0.037	0.010	0.014	0.103	0.077	0.084	0.059	0.078	0.099	0.104	0.016	0.029	0.011	0.026
Tot.	97.330	97.167	97.538	97.061	96.933	96.793	96.799	98.172	98.821	100.426	99.391	95.674	97.578	95.727	97.787	98.136	97.107	97.614
Mg#	**53.1**	**54.8**	**69.5**	**63.4**	**51.3**	**62.2**	**67.8**	**30.1**	**29.6**	**31.9**	**30.4**	**28.9**	**30.2**	**28.6**	**72.1**	**71.0**	**71.8**	**68.3**
$Fe^{3+}/\Sigma Fe$ used	0.366	0.449	0.589	0.584	0.41	0.626	0.783	0.314	0.346	0.303	0.325	0.331	0.328	0.328	0.592	0.677	0.58	0.548
Group	OH,F,Cl	OH,F,Cl	OH,F,Cl	OH,F,Cl	OH,F,Cl	OH,F,Cl	OH,F,Cl	OH,F,Cl	OH,F,Cl	OH,F,Cl	OH,F,Cl	OH,F,Cl	OH,F,Cl	OH,F,Cl	OH,F,Cl	OH,F,Cl	OH,F,Cl	OH,F,Cl
Subgroup of (OH,F,Cl)	Ca	Ca	Ca	Ca	Ca	Ca	Ca	Ca	Ca	Ca	Ca	Ca	Ca	Ca	Ca	Ca	Ca	Ca
Species	magnesio-hastingsite	magnesio-hastingsite	Ti-rich magnesio-hastingsite	Ti-rich magnesio-hastingsite	Ti-rich magnesio-hastingsite	Ti-rich magnesio-hastingsite	magnesio-hastingsite	Ti-rich ferro-ferri-sadanagaite	Ti-rich ferro-ferri-sadanagaite	Ti-rich ferro-ferri-sadanagaite	Ti-rich ferro-ferri-sadanagaite	Ti-rich ferro-ferri-sadanagaite	Ti-rich ferro-ferri-sadanagaite	Ti-rich ferro-ferri-sadanagaite	Ti-rich magnesio-hastingsite	Ti-rich magnesio-hastingsite	Ti-rich magnesio-hastingsite	Ti-rich magnesio-hastingsite
Formula Assignments																		
(T) Si	5.946	5.871	5.933	5.894	5.736	5.675	5.722	5.799	5.707	5.838	5.768	5.746	5.76	5.741	6.043	6.078	6.033	5.986
(T) Al	2.054	2.129	2.067	2.106	2.264	2.325	2.278	2.201	2.293	2.162	2.232	2.254	2.24	2.259	1.957	1.922	1.967	2.014
(T) Ti	0	0	0	0	0	0	0	0	0	0	0	0	0	0	0	0	0	0
(C) Ti	0.275	0.289	0.412	0.443	0.381	0.435	0.487	0.321	0.319	0.315	0.318	0.336	0.326	0.333	0.414	0.406	0.397	0.416
(C) Al	0.426	0.393	0.434	0.323	0.539	0.508	0.458	0.607	0.655	0.71	0.67	0.535	0.591	0.554	0.397	0.368	0.412	0.36
(C) Cr	0.001	0	0.003	0.003	0	0.003	0	0.001	0.001	0	0	0	0.001	0	0.011	0.006	0.007	0.001
(C) Fe^{3+}	0.736	0.87	0.759	0.906	0.81	0.958	1.032	0.899	0.979	0.826	0.913	0.972	0.94	0.962	0.705	0.845	0.7	0.74
(C) Ni	0	0.002	0	0.003	0	0	0	0.001	0	0.002	0.002	0.001	0	0	0.005	0.004	0.001	0.002
(C) Mn^{2+}	0.018	0.024	0	0	0.018	0	0	0	0.004	0	0	0	0	0.006	0	0	0	0
(C) Fe^{2+}	1.273	1.07	0.453	0.628	1.168	0.573	0.252	1.936	1.849	1.868	1.872	1.96	1.905	1.969	0.389	0.317	0.41	0.571
(C) Mg	2.272	2.351	2.938	2.694	2.085	2.524	2.771	1.234	1.192	1.278	1.226	1.196	1.237	1.176	3.079	3.053	3.073	2.911
(B) Mn^{2+}	0.034	0.021	0.017	0.022	0.007	0.018	0.015	0.055	0.052	0.053	0.055	0.06	0.053	0.052	0.021	0.019	0.016	0.019
(B) Fe^{2+}	0	0	0.077	0.018	0	0	0.034	0.028	0	0.037	0.024	0.007	0.019	0	0.097	0.086	0.097	0.04
(B) Ca	1.91	1.945	1.844	1.903	1.93	1.95	1.885	1.723	1.68	1.657	1.678	1.774	1.735	1.766	1.806	1.765	1.816	1.897
(B) Na	0.056	0.034	0.062	0.057	0.062	0.032	0.067	0.194	0.268	0.253	0.243	0.159	0.193	0.182	0.076	0.13	0.071	0.044
(A) Ca	0	0	0	0	0	0	0	0	0	0	0	0	0	0	0	0	0	0
(A) Na	0.729	0.692	0.688	0.741	0.748	0.673	0.661	0.612	0.667	0.62	0.628	0.628	0.632	0.658	0.697	0.622	0.702	0.754
(A) K	0.22	0.208	0.246	0.191	0.231	0.217	0.195	0.276	0.258	0.259	0.265	0.279	0.27	0.268	0.224	0.211	0.218	0.204
O (non-W)	22	22	22	22	22	22	22	22	22	22	22	22	22	22	22	22	22	22
(W) OH	1.323	1.255	1.08	0.99	1.173	1.061	0.936	1.232	1.328	1.302	1.318	1.264	1.266	1.25	1.043	1.056	1.119	0.981
(W) F	0.117	0.146	0.095	0.121	0.054	0.066	0.085	0.098	0.014	0.044	0.031	0.043	0.055	0.056	0.124	0.125	0.083	0.181
(W) Cl	0.009	0.02	0	0.002	0.01	0.003	0.004	0.027	0.02	0.021	0.015	0.021	0.026	0.028	0.004	0.007	0.003	0.007
(W) O	0.551	0.579	0.825	0.886	0.764	0.87	0.975	0.644	0.639	0.632	0.636	0.672	0.653	0.666	0.828	0.812	0.795	0.832
Sum (T,C,B,A)	15.95	15.899	15.933	15.932	15.979	15.891	15.857	15.887	15.924	15.878	15.894	15.907	15.902	15.926	15.921	15.832	15.92	15.959

Table 3: LA-ICP-MS trace element composition of representative amphibole (Amp) and clinopyroxene (Cpx) crystals from Predazzo camptonites.

Sample	FC80	FC80	FC80	FC80	FC80	FC80	FC80	FC80
Mineral	Amp	Amp	Amp	Amp	Amp	Amp	Cpx	Cpx
Type	*Type 1_core*	*Type 1_rim*	*Type 1_groundmass*	*Type 2_rim*	*Type 4_core*	*Type 4_rim*	Large phenoXX	Small phenoXX
Trace element (ppm)								
Sc	53.670	89.030	54.330	65.190	32.225	77.530	124.850	148.210
V	398.665	519.700	379.830	343.440	333.475	519.990	409.270	453.925
Cr	9.830	131.000	22.485	195.080	21.245	62.270	542.315	941.050
Co	58.415	55.180	57.550	55.115	52.450	54.550	30.240	31.635
Ni	55.205	95.635	55.720	80.480	23.930	94.380	65.720	71.360
Zn	n.d.	n.d.	n.d.	n.d.	n.d.	n.d.	n.d.	n.d.
Pb	0.441	0.550	0.372	0.569	0.744	0.474	0.234	0.196
Cs	0.050	0.260	n.d.	0.179	n.d.	0.169	n.d.	n.d.
Rb	5.340	6.195	6.055	6.705	6.990	6.510	0.049	n.d.
Ba	291.855	365.970	349.270	303.505	429.855	356.940	0.521	0.328
Th	0.095	0.078	0.101	0.040	0.151	0.131	0.080	0.106
U	0.043	0.022	0.018	0.050	0.029	<0.0118	0.011	0.016
Nb	16.310	22.335	20.005	17.685	27.125	16.080	0.511	0.854
Ta	0.681	1.054	0.973	0.826	0.981	0.862	0.095	0.096
La	7.960	7.080	10.195	7.095	12.860	7.590	5.390	4.985
Ce	25.540	23.345	33.460	23.420	38.760	22.910	18.490	18.585
Pr	4.355	4.130	5.590	4.170	6.320	4.130	3.510	3.410
Sr	767.490	763.915	786.870	728.255	796.760	735.690	100.915	103.345
Nd	24.160	22.885	30.780	23.530	33.730	22.780	20.475	20.580
Zr	83.480	120.945	112.995	96.095	134.655	97.380	98.605	113.245
Hf	2.760	4.085	3.500	3.475	4.425	3.710	3.915	5.030
Sm	6.815	5.905	8.160	6.520	8.315	6.540	6.865	6.465
Eu	2.290	2.295	2.530	2.550	2.925	2.033	2.205	2.310
Gd	6.470	6.760	7.150	6.450	7.750	6.290	6.200	6.065
Tb	1.047	1.069	1.274	1.130	1.214	1.042	1.155	1.095
Dy	6.090	5.895	6.755	6.130	7.600	5.690	6.820	6.835
Y	30.115	30.060	34.325	32.300	38.270	29.120	31.030	33.470
Ho	1.185	1.163	1.319	1.341	1.408	1.180	1.325	1.414
Er	2.955	3.105	3.200	3.220	3.910	3.040	3.030	3.185
Tm	0.375	0.433	0.454	0.403	0.531	0.390	0.501	0.529
Yb	2.525	2.430	3.105	2.730	3.370	2.520	2.720	3.170
Lu	0.373	0.298	0.440	0.358	0.507	0.405	0.391	0.455

Table 4: Major element composition and a.p.f.u. calculation of representative clinopyroxene (Cpx) crystals from Predazzo lamprophyres. Mg# = Mg/[Mg+Fe] mol%, assuming all Fe as Fe^{2+}

Sample	FC80 - Camptonite												MA5 - Camptonite						FF14 - Camptonite				
Name	Cpx1 c	Cpx1 r	Cpx3 c	Cpx4 c	Cpx6 c	Cpx6 tr1	Cpx8 c	Cpx11 c	Cpx11 r	Cpx14 c	Cpx14 r	Cpx19 c	Cpx1 c	Cpx1 tr1	Cpx1 r	Cpx2 c	Cpx3 c	Cpx4 c	Cpx1 c	Cpx2 c	Cpx5 c	Cpx8 c	Cpx12 c
Oxide (wt%)																							
SiO_2	49.604	42.278	48.742	47.089	44.324	45.773	43.078	45.583	48.050	45.548	45.762	46.792	47.658	47.176	43.272	43.518	47.591	42.472	44.043	44.549	42.305	47.141	48.427
TiO_2	1.108	4.031	1.206	2.126	2.065	2.136	3.164	2.266	2.012	2.151	1.974	1.744	1.461	1.491	3.773	3.844	2.089	4.049	3.343	2.614	3.633	1.947	1.536
Al_2O_3	5.005	9.933	5.847	5.462	10.878	9.710	10.085	9.836	5.581	9.582	9.247	9.208	8.612	9.028	10.068	9.320	5.270	9.178	9.003	8.648	10.510	5.790	4.823
FeO_{TOT}	5.751	8.483	6.028	8.099	8.532	6.142	7.942	6.680	7.971	6.469	6.756	6.383	5.394	5.476	7.874	8.073	8.106	9.655	6.928	6.474	7.052	8.213	6.620
MnO	0.138	0.139	0.130	0.180	0.176	0.118	0.143	0.125	0.200	0.126	0.126	0.116	0.110	0.119	0.110	0.133	0.146	0.139	0.112	0.130	0.096	0.168	0.170
MgO	14.534	10.291	14.344	12.714	10.378	12.376	11.069	12.295	12.714	12.290	12.161	12.765	13.600	13.384	11.329	11.037	13.487	10.405	11.393	12.179	11.164	12.814	14.086
CaO	22.176	22.555	21.673	22.676	21.990	22.073	22.669	22.133	22.611	22.259	22.334	21.958	22.045	21.903	22.618	22.829	21.650	22.464	22.758	22.967	22.873	22.475	22.767
Na_2O	0.502	0.594	0.505	0.410	0.754	0.641	0.471	0.621	0.448	0.624	0.597	0.650	0.555	0.558	0.414	0.533	0.322	0.524	0.408	0.406	0.416	0.332	0.283
K_2O	0.000	0.017	0.000	0.022	0.004	0.005	0.005	0.008	0.008	0.000	0.002	0.014	0.000	0.015	0.004	0.005	0.000	0.006	0.059	0.012	0.023	0.014	0.007
Cr_2O_3	0.133	0.000	0.155	0.010	0.041	0.142	0.025	0.194	0.000	0.258	0.047	0.205	0.462	0.510	0.249	0.202	0.121	0.002	0.442	0.830	0.463	0.025	0.159
NiO	0.000	0.019	0.020	0.013	0.009	0.022		0.012	0.007	0.000	0.010	0.015	0.036	0.034	0.017	0.000	0.006	0.000	0.020	0.000	0.000	0.000	0.000
Tot.	98.933	98.336	98.643	98.799	99.150	99.138	98.782	99.754	99.601	99.306	99.015	99.849	99.932	99.695	99.727	99.494	98.788	98.893	98.510	98.804	98.557	98.983	98.933
Mg#	**81.8**	**68.4**	**80.9**	**73.7**	**68.4**	**78.2**	**71.3**	**76.6**	**74.0**	**77.2**	**76.2**	**78.1**	**81.8**	**81.3**	**71.9**	**70.9**	**74.8**	**65.8**	**74.6**	**77.0**	**73.8**	**73.5**	**79.1**
A.p.f.u.																							
(T) Si^{4+}	1.841	1.612	1.815	1.775	1.664	1.703	1.628	1.688	1.796	1.694	1.708	1.727	1.751	1.738	1.621	1.636	1.791	1.616	1.667	1.674	1.600	1.774	1.810
(T) Al^{3+}	0.159	0.388	0.185	0.225	0.336	0.297	0.372	0.312	0.204	0.306	0.292	0.273	0.249	0.262	0.379	0.364	0.209	0.384	0.333	0.326	0.400	0.226	0.190
(T) Fe^{3+}	0.000	0.000	0.000	0.000	0.000	0.000	0.000	0.000	0.000	0.000	0.000	0.000	0.000	0.000	0.000	0.000	0.000	0.000	0.000	0.000	0.000	0.000	0.000
(M1) Al^{3+}	0.060	0.058	0.072	0.017	0.146	0.128	0.077	0.118	0.041	0.114	0.115	0.127	0.124	0.130	0.065	0.050	0.025	0.028	0.069	0.057	0.069	0.031	0.022
(M1) Fe^{3+}	0.069	0.144	0.078	0.119	0.127	0.092	0.149	0.107	0.083	0.109	0.108	0.091	0.071	0.075	0.124	0.130	0.086	0.164	0.093	0.127	0.142	0.110	0.097
(M1) Ti^{4+}	0.031	0.116	0.034	0.060	0.058	0.060	0.090	0.063	0.057	0.060	0.055	0.048	0.040	0.041	0.106	0.109	0.059	0.116	0.095	0.074	0.103	0.055	0.043
(M1) Cr^{3+}	0.004	0.000	0.005	0.000	0.001	0.004	0.001	0.006	0.000	0.008	0.001	0.006	0.013	0.015	0.007	0.006	0.004	0.000	0.013	0.025	0.014	0.001	0.005
(M1) Ni^{2+}	0.000	0.001	0.001	0.000	0.000	0.001	0.000	0.000	0.000	0.000	0.000	0.000	0.001	0.001	0.001	0.000	0.000	0.000	0.001	0.000	0.000	0.000	0.000
(M1) Mg^{2+}	0.804	0.585	0.796	0.714	0.581	0.686	0.624	0.679	0.708	0.681	0.677	0.702	0.745	0.735	0.633	0.619	0.757	0.590	0.643	0.682	0.630	0.719	0.785
(M1) Fe^{2+}	0.032	0.097	0.015	0.089	0.086	0.029	0.060	0.027	0.111	0.028	0.043	0.025	0.006	0.003	0.064	0.087	0.070	0.103	0.086	0.035	0.042	0.085	0.047
(M2) Fe^{2+}	0.078	0.030	0.095	0.048	0.055	0.070	0.043	0.073	0.056	0.064	0.060	0.081	0.089	0.091	0.059	0.037	0.099	0.041	0.041	0.041	0.038	0.064	0.062
(M2) Mn^{2+}	0.004	0.004	0.004	0.006	0.006	0.004	0.005	0.004	0.006	0.004	0.004	0.004	0.003	0.004	0.003	0.004	0.005	0.004	0.004	0.004	0.003	0.005	0.005
(M2) Ca^{2+}	0.882	0.921	0.865	0.916	0.885	0.880	0.918	0.878	0.905	0.887	0.893	0.868	0.868	0.865	0.908	0.920	0.873	0.916	0.923	0.925	0.927	0.906	0.912
(M2) Na^{+}	0.036	0.044	0.036	0.030	0.055	0.046	0.035	0.045	0.032	0.045	0.043	0.046	0.040	0.040	0.030	0.039	0.023	0.039	0.030	0.030	0.031	0.024	0.021
(M2) K^{+}	0.000	0.001	0.000	0.001	0.000	0.000	0.000	0.000	0.000	0.000	0.000	0.001	0.000	0.001	0.000	0.000	0.000	0.000	0.003	0.001	0.001	0.001	0.000
Wo	47.18	51.72	46.67	48.42	50.87	49.96	51.07	49.68	48.44	50.01	50.04	49.02	48.70	48.79	50.70	51.19	46.20	50.38	51.60	50.96	52.00	47.97	47.76
En	43.03	32.84	42.98	37.78	33.41	38.98	34.70	38.40	37.90	38.42	37.92	39.65	41.81	41.48	35.33	34.44	40.05	32.47	35.94	37.60	35.32	38.06	41.12
Fs	9.78	15.44	10.35	13.80	15.73	11.06	14.22	11.92	13.67	11.57	12.04	11.33	9.49	9.73	13.97	14.37	13.75	17.15	12.46	11.44	12.69	13.97	11.12
Tot.	100.00	100.00	100.00	100.00	100.00	100.00	100.00	100.00	100.00	100.00	100.00	100.00	100.00	100.00	100.00	100.00	100.00	100.00	100.00	100.00	100.00	100.00	100.00

Table 5: Major element composition and a.p.f.u. calculation of representative plagioclase (Pl) and K-feldspar (Kfs) crystals from Predazzo lamprophyres

Sample	FC80 - Camptonite										FF14 - Camptonite						MA5 - Camptonite		MA1 - Camptonite				
Mineral	Pl	Pl	Pl	Pl	Pl	Pl	Pl	Pl	Pl	Pl	Pl	Pl	Pl	Pl	Pl	Pl	Pl	Pl	Pl	Pl	Kfs	Kfs	Kfs
Name	Plag1_c	Plag1_tr1	Plag1_tr2	Plag1_tr3	Plag1_r	Plag4_c	Plag5_c	Plag5_r	PLag7_c	Plag7_r	Plag3_c	Plag4_c	Plag8_c	Plag10_c	Plag11_c	Plag14_c	Plag3_c	Plag5_c	Plag1_c	Plag3_c	Kf1_c	Kf2_c	Kf4_c
Oxide (wt%)																							
SiO_2	56.994	55.766	56.303	56.115	49.614	51.747	55.204	49.116	52.291	50.105	53.309	51.735	49.748	55.984	49.369	50.193	49.209	49.275	61.624	56.077	64.624	65.065	65.340
TiO_2	0.013	0.000	0.002	0.012	0.107	0.087	0.013	0.086	0.015	0.102	0.148	0.127	0.091	0.126	0.067	0.121	0.081	0.071	0.024	0.041	0.012	0.000	0.014
Al_2O_3	26.996	27.050	27.099	27.365	30.781	30.266	28.417	31.571	30.506	31.151	29.209	29.855	30.713	27.734	31.030	30.352	31.688	32.093	23.858	26.491	19.408	19.523	19.125
FeO_{TOT}	0.147	0.450	0.151	0.143	0.587	0.639	0.203	0.596	0.043	0.520	0.595	0.614	0.631	0.560	0.770	0.676	0.619	0.554	0.309	0.418	0.271	0.195	0.207
MnO	0.000	0.006	0.000	0.000	0.000	0.020	0.004	0.003	0.002	0.008	0.013	0.000	0.007	0.006	0.014	0.000	0.009	0.000	0.009	0.009	0.010	0.000	0.005
MgO	0.002	0.379	0.000	0.000	0.082	0.071	0.006	0.101	0.000	0.079	0.050	0.067	0.112	0.029	0.131	0.125	0.111	0.104	0.008	0.032	0.012	0.000	0.010
CaO	8.566	9.274	8.988	9.313	13.734	12.879	10.469	14.586	12.605	13.943	11.550	12.615	13.904	9.586	14.186	13.688	15.000	15.240	4.748	8.586	0.294	0.350	0.244
BaO	0.000	0.013	0.000	0.027	0.066	0.036	0.007	0.037	0.000	0.009	0.049	0.071	0.000	0.143	0.000	0.029	0.000	0.000	0.000	0.000	0.000	0.000	0.000
Na_2O	6.687	5.987	6.230	6.216	3.380	3.857	5.559	3.047	4.439	3.471	4.736	4.084	3.131	5.529	3.186	3.453	3.025	2.841	7.941	6.184	4.700	5.019	5.021
K_2O	0.240	0.189	0.220	0.174	0.265	0.289	0.247	0.211	0.190	0.246	0.453	0.378	0.496	0.643	0.240	0.301	0.135	0.146	1.177	0.579	9.925	9.465	9.555
Tot.	99.610	99.113	98.986	99.347	98.609	99.890	100.130	99.353	100.064	99.632	100.110	99.537	98.825	100.341	98.980	98.938	99.875	100.323	99.696	98.417	99.255	99.618	99.561
A.p.f.u.																							
Si	2.558	2.526	2.551	2.533	2.292	2.356	2.482	2.256	2.363	2.289	2.410	2.361	2.296	2.518	2.275	2.312	2.249	2.244	2.751	2.557	2.942	2.946	2.963
Ti	0.000	0.000	0.000	0.000	0.004	0.003	0.000	0.003	0.001	0.004	0.005	0.004	0.003	0.004	0.002	0.004	0.003	0.002	0.001	0.001	0.000	0.000	0.000
Al	1.428	1.444	1.447	1.456	1.676	1.624	1.506	1.709	1.625	1.677	1.557	1.606	1.671	1.470	1.685	1.648	1.707	1.722	1.255	1.424	1.041	1.042	1.022
Cr	0.000	0.000	0.000	0.000	0.000	0.000	0.000	0.000	0.000	0.000	0.000	0.000	0.000	0.000	0.000	0.000	0.000	0.000	0.000	0.000	0.000	0.000	0.000
Fe^{3+}	0.000	0.000	0.000	0.000	0.000	0.000	0.000	0.000	0.000	0.000	0.000	0.000	0.000	0.000	0.000	0.000	0.000	0.000	0.000	0.000	0.000	0.000	0.000
Fe^{2+}	0.006	0.017	0.006	0.005	0.023	0.024	0.008	0.023	0.002	0.020	0.022	0.023	0.024	0.021	0.030	0.026	0.024	0.021	0.012	0.016	0.010	0.007	0.008
Mn	0.000	0.000	0.000	0.000	0.000	0.001	0.000	0.000	0.000	0.000	0.000	0.000	0.000	0.000	0.001	0.000	0.000	0.000	0.000	0.000	0.000	0.000	0.000
Mg	0.000	0.026	0.000	0.000	0.006	0.005	0.000	0.007	0.000	0.005	0.003	0.005	0.008	0.002	0.009	0.009	0.008	0.007	0.001	0.002	0.001	0.000	0.001
Ca	0.412	0.450	0.436	0.450	0.680	0.628	0.504	0.718	0.610	0.683	0.560	0.617	0.688	0.462	0.700	0.675	0.734	0.744	0.227	0.419	0.014	0.017	0.012
Ba	0.000	0.000	0.000	0.000	0.001	0.001	0.000	0.001	0.000	0.000	0.001	0.001	0.000	0.003	0.000	0.001	0.000	0.000	0.000	0.000	0.000	0.000	0.000
Na	0.582	0.526	0.547	0.544	0.303	0.341	0.485	0.271	0.389	0.307	0.415	0.361	0.280	0.482	0.285	0.308	0.268	0.251	0.687	0.547	0.415	0.441	0.441
K	0.014	0.011	0.013	0.010	0.016	0.017	0.014	0.012	0.011	0.014	0.026	0.022	0.029	0.037	0.014	0.018	0.008	0.008	0.067	0.034	0.576	0.547	0.553
Tot. cat.	5.000	5.000	5.000	5.000	5.000	5.000	5.000	5.000	5.000	5.000	5.000	5.000	5.000	5.000	5.000	5.000	5.000	5.000	5.000	5.000	5.000	5.000	5.000
Tot. oxy.	7.975	7.980	7.994	7.985	7.975	7.993	7.986	7.972	7.976	7.970	7.973	7.976	7.980	7.998	7.970	7.977	7.967	7.978	8.002	7.980	7.967	7.974	7.977
An	40.88	45.61	43.79	44.84	68.10	63.75	50.28	71.67	60.41	67.96	55.91	61.67	68.97	47.09	70.10	67.45	72.69	74.14	23.14	41.95	1.43	1.69	1.18
Ab	57.75	53.28	54.93	54.16	30.33	34.55	48.31	27.09	38.50	30.61	41.48	36.13	28.10	49.15	28.49	30.79	26.53	25.01	70.03	54.68	41.25	43.87	43.88
Or	1.36	1.11	1.28	1.00	1.56	1.70	1.41	1.23	1.08	1.43	2.61	2.20	2.93	3.76	1.41	1.77	0.78	0.84	6.83	3.37	57.32	54.44	54.94
Tot.	100.00	100.00	100.00	100.00	100.00	100.00	100.00	100.00	100.00	100.00	100.00	100.00	100.00	100.00	100.00	100.00	100.00	100.00	100.00	100.00	100.00	100.00	100.00

Table 6: Major element composition and a.p.f.u. calculation of representative Fe-Ti oxides from Predazzo lamprophyres

Sample	FC80 - Camptonite				MA1 - Camptonite
Name	Ox1	Ox2	Ox5	Ox7	Ox3
Oxides (wt%)					
SiO_2	0.524	0.097	0.788	0.514	2.106
TiO_2	17.615	12.139	18.982	18.339	12.260
Al_2O_3	7.851	2.330	5.533	7.381	4.283
FeO	61.332	77.084	63.173	62.735	69.367
MnO	0.783	0.976	0.907	0.756	1.451
MgO	2.331	0.219	0.950	2.418	0.196
CaO	0.166	0.119	0.562	0.198	0.219
Cr_2O_3	0.146	0.000	0.044	0.036	0.043
V_2O_3	0.455	0.086	0.363	0.469	0.097
NiO	0.000	0.000	0.000	0.000	0.030
ZnO	0.166	0.238	0.322	0.110	0.237
Tot.	91.364	93.269	91.615	92.956	90.288
A.p.f.u.					
Si	0.020	0.004	0.031	0.019	0.083
Ti	0.503	0.352	0.553	0.515	0.363
Al	0.351	0.106	0.253	0.325	0.199
Fe^{3+}	0.000	0.000	0.000	0.000	0.000
Fe^{2+}	1.947	2.487	2.046	1.961	2.283
Mn	0.025	0.032	0.030	0.024	0.048
Mg	0.132	0.013	0.055	0.135	0.011
Ca	0.007	0.005	0.023	0.008	0.009
Cr	0.004	0.000	0.001	0.001	0.001
V	0.011	0.002	0.009	0.012	0.003
Tot. Cat.	3.000	3.000	3.000	3.000	3.000
FeO (mol%)	**63.04**	**58.10**	**63.78**	**62.76**	**62.79**
Fe_2O_3 (mol%)	**13.63**	**26.24**	**12.33**	**13.60**	**20.67**
TiO_2 (mol%)	**23.32**	**15.66**	**23.90**	**23.65**	**16.55**

Table 7: Major element composition of representative carbonates in Predazzo lamprophyres

Sample	FC80 - Camptonite														
Name	C1	C3	C4	C5	C6	C7	C9	C10	C11	C13	C14	C15	C16	C18	C19
Oxides (wt%)															
SiO_2	0.023	0.017	0.011	0.006	0.012	0.007	0.016	0.025	0.000	0.043	0.000	0.021	0.000	0.000	0.030
FeO	35.147	34.065	32.973	5.434	10.377	5.523	6.483	10.561	38.746	38.623	38.958	14.368	7.794	5.001	6.548
MnO	0.406	0.447	0.483	0.544	0.249	0.467	0.391	0.328	0.647	0.550	0.581	0.423	0.477	0.421	0.450
MgO	18.482	18.521	17.697	18.416	16.137	18.578	18.025	13.629	14.356	15.035	15.342	12.706	16.453	18.538	17.990
CaO	2.209	3.343	5.232	28.475	27.579	29.062	28.604	29.870	3.645	3.137	2.250	27.823	28.638	28.816	27.907
SrO	0.000	0.000	0.000	0.212	0.080	0.166	0.033	0.054	0.000	0.000	0.000	0.066	0.161	0.304	0.098
Tot.	56.266	56.393	56.397	53.087	54.435	53.803	53.552	54.465	57.394	57.388	57.131	55.405	53.522	53.080	53.023
$CaCO_3$ (%)	**3.966**	**5.962**	**9.343**	**48.352**	**47.239**	**48.690**	**48.411**	**52.050**	**6.703**	**5.737**	**4.131**	**48.722**	**49.310**	**48.831**	**47.715**
$MgCO_3$ (%)	**46.167**	**45.958**	**43.971**	**43.510**	**38.457**	**43.306**	**42.446**	**33.043**	**36.728**	**38.254**	**39.194**	**30.957**	**39.416**	**43.708**	**42.798**
$FeCO_3$ (%)	**49.253**	**47.421**	**45.961**	**7.202**	**13.873**	**7.222**	**8.565**	**14.364**	**55.610**	**55.129**	**55.833**	**19.639**	**10.474**	**6.615**	**8.739**
$SrCO_3$ (%)	**0.000**	**0.000**	**0.024**	**0.197**	**0.075**	**0.152**	**0.031**	**0.051**	**0.018**	**0.012**	**0.000**	**0.063**	**0.152**	**0.281**	**0.091**
$MnCO_3$ (%)	**0.577**	**0.630**	**0.682**	**0.730**	**0.337**	**0.619**	**0.523**	**0.451**	**0.941**	**0.796**	**0.843**	**0.585**	**0.649**	**0.564**	**0.608**

Table 8: *P*, *T*, fO_2 and H_2O parameters obtained by mineral-melt and single mineral calculations on Predazzo lamprophyres. For each applied method, the corresponding reference and error on the single parameters are reported. *T* and *P* of clinopyroxene crystallization were obtained by means of the single mineral equations of Putirka (2008). Oxygen fugacity was calculated by means of the Ishibashi (2013) oxy-barometer. The water content of the melt during amphibole crystallization was calculated using the Ridolfi *et al.* (2010) single-mineral hygrometer. *T* and *P* of amphibole crystallization were obtained by means of the Putirka (2016) mineral-melt thermometer and H_2O-dependent barometer. This latter equation was applied by considering as input the H_2O content of the coexisting melt resulted from the hygrometer of Ridolfi *et al.* (2010). Cpx: clinopyroxene; Amp: amphibole

Sample	Type (Amp)	Method	Reference	T (°C)	Error (°C)	P (MPa)	Error (MPa)	H_2O (wt%)	Error (wt%)	logfO_2
MA5 - Camptonite	-	Cpx-only	Putirka (2008), Eq. 32a/32d	1060-1124	±58	230-640	±310	-	-	-
FC80 - Camptonite	*Type 1_core*	Amp-only; Amp-melt	Ridolfi et al. (2010); Putirka (2016), Eq. 5/7b	1023-1069	±30	920-1160	±170	7.2-8.5	±0.8-1.2	-
FC80 - Camptonite	*Type 1_rim*	Amp-only; Amp-melt	Ridolfi et al. (2010); Putirka (2016), Eq. 5/7b	1038-1067	±30	740-900	±170	6.8-7.5	±0.8-1.2	-
FC80 - Camptonite	*Type 1_intermediate*	Amp-only; Amp-melt	Ridolfi et al. (2010); Putirka (2016), Eq. 5/7b	1071	±30	1050	±170	7.7	±0.8-1.2	-
FC80 - Camptonite	*Type 1_groundmass*	Amp-only; Amp-melt	Ridolfi et al. (2010); Putirka (2016), Eq. 5/7b	1025-1074	±30	850-1110	±170	6.7-8.1	±0.8-1.2	-
MA1 - Camptonite	*Type 1_core*	Amp-only; Amp-melt	Ridolfi et al. (2010); Putirka (2016), Eq. 5/7b	948-1042	±30	620-980	±170	6.5-7.7	±0.8-1.2	-
MA1 - Camptonite	*Type 1_rim*	Amp-only; Amp-melt	Ridolfi et al. (2010); Putirka (2016), Eq. 5/7b	1031-1032	±30	600-640	±170	6.2-6.6	±0.8-1.2	-
MA1 - Camptonite	*Type 1_groundmass*	Amp-only; Amp-melt	Ridolfi et al. (2010); Putirka (2016), Eq. 5/7b	1001-1029	±30	470-800	±170	6.5-7.6	±0.8-1.2	-
FC80 - Camptonite	*Type 2_core*	Amp-only; Amp-melt	Ridolfi et al. (2010); Putirka (2016), Eq. 5/7b	997-1009	±30	890-920	±170	6.8-7.1	±0.8-1.2	-
FC80 - Camptonite	*Type 2_rim*	Amp-only; Amp-melt	Ridolfi et al. (2010); Putirka (2016), Eq. 5/7b	1005-1053	±30	730-770	±170	6.8-7.0	±0.8-1.2	-
FC80 - Camptonite	*Type 2_intermediate*	Amp-only; Amp-melt	Ridolfi et al. (2010); Putirka (2016), Eq. 5/7b	1051-1063	±30	920-970	±170	7.2-7.4	±0.8-1.2	-
FC80 - Camptonite	*Type 3_rim*	Amp-only; Amp-melt	Ridolfi et al. (2010); Putirka (2016), Eq. 5/7b	1057-1063	±30	870-980	±170	7.2-7.3	±0.8-1.2	-
MA1 - Camptonite	*Type 3_rim*	Amp-only; Amp-melt	Ridolfi et al. (2010); Putirka (2016), Eq. 5/7b	961-1030	±30	630-750	±170	6.4-7.8	±0.8-1.2	-
FC80 - Camptonite	*Type 4_core*	Amp-only; Amp-melt	Ridolfi et al. (2010); Putirka (2016), Eq. 5/7b	1008	±30	1220	±170	8.9	±0.8-1.2	-
FC80 - Camptonite	*Type 4_rim*	Amp-only; Amp-melt	Ridolfi et al. (2010); Putirka (2016), Eq. 5/7b	1042-1060	±30	1120-1230	±170	8.3	±0.8-1.2	-
MA1 - Camptonite	*Type 5_core*	Amp-only; Amp-melt	Ridolfi et al. (2010); Putirka (2016), Eq. 5/7b	927-983	±30	960-1130	±170	8.8-9.8	±0.8-1.2	-
MA1 - Camptonite	*Type 5_rim*	Amp-only; Amp-melt	Ridolfi et al. (2010); Putirka (2016), Eq. 5/7b	977-1048	±30	490-690	±170	5.8-6.9	±0.8-1.2	-
FC80 - Camptonite	-	Ti-magnetite-melt	Ishibashi (2013)	1100 (input)	-	500 (input)	-	-	-	-8.4/-10.0
MA1 - Camptonite	-	Ti-magnetite-melt	Ishibashi (2013)	1050 (input)	-	500 (input)	-	-	-	-9.4/-11.0

Table 9: Modal composition, melting proportions and REE composition of the mantle sources used in the partial melting models. Ol: olivine; Opx: orthopyroxene; Cpx: clinopyroxene; Spl: spinel; Grt: garnet: Amp: amphibole; Phl: phlogopite. I = Spl-lherzolite with DMM composition (Workman & Hart 2005); II = Spl-lherzolite; III = Grt-lherzolite; IV = Spl-Grt-Amp-lherzolite; V = Grt-Amp-lherzolite; VI = Grt-Phl-lherzolite. Starting REE composition of II, III, IV, V and VI sources is fertile PM of Sun & McDonough (1989). REE partition coefficients used in the models are also reported. Olivine, Opx, Cpx, Spl, Grt and Amp partition coefficients are from McKenzie & O'Nions (1991) and Schmidt *et al.* (1999), except for Tm in Cpx (Zack & Brumm, 1998). Phlogopite partition coefficients: La, Ce, Nd and Sm from Schmidt *et al.* (1999); Eu, Gd, Dy, Er, Yb and Lu from Fujimaki *et al.* (1984); Pr, Tb, Ho and Tm were extrapolated from the partition coefficients of the adjacent elements according to Barry *et al.* (2003)

Source modal composition	I	II	III	IV	V	VI
Ol	0.57	0.55	0.55	0.55	0.55	0.56
Opx	0.28	0.25	0.25	0.19	0.2	0.19
Cpx	0.13	0.15	0.15	0.15	0.15	0.15
Spl	0.02	0.05	-	0.02	-	-
Grt	-	-	0.05	0.04	0.04	0.02
Amp	-	-	-	0.05	0.06	0.02
Phl	-	-	-	-	-	0.06

Source melting proportions	I	II	III	IV	V	VI
Ol	0.01	0.01	0.01	0.05	0.03	0.03
Opx	0.09	0.09	0.07	0.05	0.05	0.05
Cpx	0.6	0.6	0.6	0.1	0.22	0.1
Spl	0.3	0.3	-	0.1	0	-
Grt	-	-	0.32	0.2	0.2	0.15
Amp	-	-	-	0.5	0.5	0.37
Phl	-	-	-	-	-	0.3

Source REE composition	I	II	III	IV	V	VI
La	0.192	0.687	0.687	0.687	0.687	0.687
Ce	0.55	1.775	1.775	1.775	1.775	1.775
Pr	0.107	0.276	0.276	0.276	0.276	0.276
Nd	0.581	1.354	1.354	1.354	1.354	1.354
Sm	0.239	0.444	0.444	0.444	0.444	0.444
Eu	0.0096	0.168	0.168	0.168	0.168	0.168
Gd	0.358	0.596	0.596	0.596	0.596	0.596
Tb	0.07	0.108	0.108	0.108	0.108	0.108
Dy	0.505	0.737	0.737	0.737	0.737	0.737
Ho	0.115	0.164	0.164	0.164	0.164	0.164
Er	0.348	0.48	0.48	0.48	0.48	0.48
Tm	-	0.074	0.074	0.074	0.074	0.074
Yb	0.365	0.493	0.493	0.493	0.493	0.493
Lu	0.058	0.074	0.074	0.074	0.074	0.074

Partition coefficients	Ol	Opx	Cpx	Spl	Grt	Amp	Phl
La	0.0004	0.002	0.054	0.01	0.01	0.17	0.00002
Ce	0.0005	0.003	0.098	0.01	0.021	0.26	0.0002
Pr	0.0008	0.0048	0.15	0.01	0.054	0.35	0.0002
Nd	0.001	0.0068	0.21	0.01	0.087	0.44	0.0002
Sm	0.0013	0.01	0.26	0.01	0.217	0.76	0.0002
Eu	0.0016	0.013	0.31	0.01	0.32	0.88	0.0218
Gd	0.0015	0.016	0.3	0.01	0.498	0.86	0.0205
Tb	0.0015	0.019	0.31	0.01	0.75	0.83	0.025
Dy	0.0017	0.022	0.33	0.01	1.06	0.78	0.0281
Ho	0.0016	0.026	0.31	0.01	1.53	0.73	0.028
Er	0.0015	0.03	0.29	0.01	2	0.68	0.0303
Tm	0.0015	0.04	0.449	0.01	3	0.64	0.035
Yb	0.0015	0.049	0.28	0.01	4.03	0.59	0.0484
Lu	0.0015	0.06	0.28	0.01	5.5	0.51	0.0471